TÉCNICO LISBOA

Optimization of Ni nanofoams for assembling a Ni-Cap device

Olesia Meroniuk

Thesis to obtain the Master of Science Degree in

Energy Engineering and Management

Supervisor: Prof. Maria de Fátima Grilo da Costa Montemor

Examination Committee

Chairperson: Prof. Duarte de Mesquita e Sousa

Supervisor: Prof. Maria de Fátima Grilo da Costa Montemor

Member of the Committee: Prof. Maria Teresa Oliveira de Moura e Silva

November 2018

Acknowledgments

This thesis is based on the work conducted within the KIC InnoEnergy Master School, in the MSc programme in Renewable Energy. This programme is supported financially by the KIC InnoEnergy. The author also received financial support from KIC InnoEnergy, which is gratefully acknowledged.

KIC InnoEnergy is a company supported by the European Institute of Innovation and Technology (EIT) and has the mission of delivering commercial products and services, new businesses, innovators and entrepreneurs in the field of sustainable energy through the integration of higher education, research, entrepreneurs and business companies. Shareholders in KIC InnoEnergy are leading industries, research centers, universities and business schools from across Europe.

The MSc programme in Renewable Energy is a collaboration of:

IST Instituto Superior Técnico, Portugal,
KTH Royal Institute of Technology, Sweden,
École Polytechnique, Université Paris-Saclay, France,
UPC Universitat Politècnica de Catalunya · BarcelonaTech, Spain.

Acknowledgments

The work presented in this thesis was accomplished with the help of many colleagues and friends. It is a pleasant opportunity to express my thankfulness to all the people who have helped me directly or indirectly in their various capacities during my Master study.

Firstly, I would like to express my sincere gratitude and respect to my supervisor Prof. Maria de Fátima Grilo da Costa Montemor who started by proposing this Master project and believing in my capacity to accomplish it. Thank you for the continuous support of my Master study and related research, for guiding me, often with big doses of patience. I could not have imagined having a better supervisor for my Master study.

My sincere thanks also goes to Rui Silva, André Mão de Ferro and Cátia Piedade, who provided me an opportunity to join their team at C2C-NewCap, and who gave access to their laboratory and research materials. Thank for their co-operative support, and also presenting with an opportunity for me to have a practical experience in this organization. It was a great chance for learning and professional development.

My very profound gratitude to my dear friend and collegue Katarzyna Irena Siwek (PhD student) for enlightening me the first glance of research. You supported me greatly and were always willing to help me. Your positive outlook and confidence in my work inspired me and gave me confidence. Without your precious support and motivation it would not be possible to conduct this thesis.

I thank my collegues and friends of the Electrochemical laboratory at the Department of Chemical Engineering (DEQ) for the stimulating discussions and for all the fun we have had in the last year. In particulat to Kush Kumar Upadhyay and Alberto Adán Más for their insightful comments and encouragement, but also for the hard question which incented me to widen my research from various perspectives.

A special thank to Sónia Eugénio for her help with Scanning Electron Microscopy. I choose this moment to acknowledge her contribution gratefully.

Most importantly, I wish to express my love and my gratitude my parents for supporting me throughout my years of study and my life in general. Finally, I wish to thank my loving and supportive boyfriend, Chris Lyons, for providing me with unfailing support and continuous encouragement through the process of researching and writing this thesis. Also to all my friends who never give up in giving their support to me in all aspects of life. This accomplishment would not have been possible without them.

Abstract

The work in this thesis includes development and testing of novel electrodes based on nanostructured metallic foams of Ni and Ni hydroxide for application as electrode for hybrid supercapacitor. The first part of this thesis is dedicated to modification of morphology of the electrode current collector by Ni nano-foams using electrodeposition techniques. Next, the as prepared electrode supports were functionalized with active material Ni hydroxide.

The experimental results are presented to illustrate the influence of fabrication technique and electrode architecture on the overall electrode performance. Analysis of the produced composites was carried out using scanning electron microscopy and Raman spectroscopy. The electrochemical response was assessed by cyclic voltammetry and chronopotentiometry experiments. Obtained results showed that electrodes based on nickel hydroxide are very promising for hybrid supercapacitor applications. Introducing nanostructured composite as electrode support significantly improves overall performance of the electrode.

Key words: electrodeposition, supercapacitor, hybrid, energy storage.

Resumo

Esta dissertação incluiu o desenvolvimento e teste de novos eletrodos baseados em espumas metálicas nanoestruturadas de níquel e de hidróxido de níquel para aplicação como eletrodo em supercondensadores híbridos. A primeira parte deste trabalho é dedicada à eletrodeposição de espumas 3D nanoestruturadas porosas de níquel sobre uma espuma comercial de níquel, de forma a preparar compósitos que possam ser usados como suportes de eletrodos. Seguidamente, um material activo de hidróxido de níquel foi introduzido na estrutura porosa dos suportes preparados para produzir um eléctrodo.

Os resultados experimentais são apresentados para ilustrar a influência da técnica de fabrico e da arquitetura do eletrodo no desempenho geral do eletrodo. A análise dos compostos produzidos foi realizada por microscopia eletrónica de varrimento e espectroscopia Raman. A resposta eletroquímica foi avaliada por ensaios de voltametria cíclica e cronopotenciometria. Os resultados obtidos mostraram que eletrodos baseados em hidróxido de níquel são muito promissores para aplicações de supercondensadores híbridos. A introdução do composto nanoestruturado como suporte do eletrodo melhora significativamente o desempenho geral do mesmo.

Palavras-chave: armazenamento de energia, supercondensador, híbrido, eletrodeposição.

Table of Contents

List of Tables

List of Figures

Nomenclature

OECD	–	Economic Cooperation and Development
EES	–	Electric Energy Storage
RES	–	Renewable energy sources
HEV	–	Hybrid electric vehicles
SC	–	Supercapacitor
NMF	–	Nanostructured metallic foam
CNF	–	Commercial Nickel Foam
NF	–	Nanostructured Nickel Foam
StE	–	Sintered electrode provided by C2C-Newcap
S/CNF	–	Sintered Nickel over Commercial Nickel Foam
Ox	–	Oxidized species
Red	–	Reduced species
$\bar{e}$	–	electron
PHS	–	Pumped Hydroelectric Storage
CAES	–	Compressed Air Energy Storage
SNG	–	Synthetic Natural Gas
CV	–	Cyclic Voltammetry
EDLC	–	Electrical Double Layer Capacitor
DHBT	–	Dynamic Hydrogen Bubble Template
GCD	–	Galvanostatic charge-discharge
SCE	–	Saturated Calomel Electrode
AC	–	Activated carbon
I	–	Constant current [mA]
$t_{discharge}$	–	Discharge time [sec]
m	–	mass [g]
C_s	–	Specific capacitance [F g^{-1}]
E_{real}	–	Real energy density [Wh kg^{-1}]
P_{real}	–	Real power density [W kg^{-1}]
E_{real}	–	Real energy [Wh kg^{-1}]
ΔV_{disch}	–	Potential difference between the end of the charge and the end of the discharge [V]
IR	–	Internal resistance

I. Introduction

Building a sustainable and secure future is a major scientific and social challenge facing modern society. In a worldwide development the energy sector plays a crucial role. It has been reported that with expected growth of global population, industrialization and urbanization, the world energy consumption will rise by 28% by 2040 [1]. Most of the growth is predicted to be driven by increasing prosperity in emerging economies of the countries that are not members the Organization for Economic Cooperation and Development (OECD), specifically China, India and Southeast Asia [2].

In 2017 the global economic output is estimated to have risen by 3.7% [3], leading to the growth of global energy demand by 2.1%. The same time fossil fuels continue to dominate accounting for the largest share of 81% in global energy demand. According to the International Energy Agency, energy generation from fossil fuels is the main source of greenhouse gases such as nitrous oxide, methane and carbon dioxide, which tend to contribute to air pollution and cause climate disruption. Each year millions of tons of these pollutants are released into the atmosphere. In 2017 CO_2 emissions associated with energy production increased by 1.4% worldwide (Fig. 1), reaching the highest in history value of 32.5Gt [4].

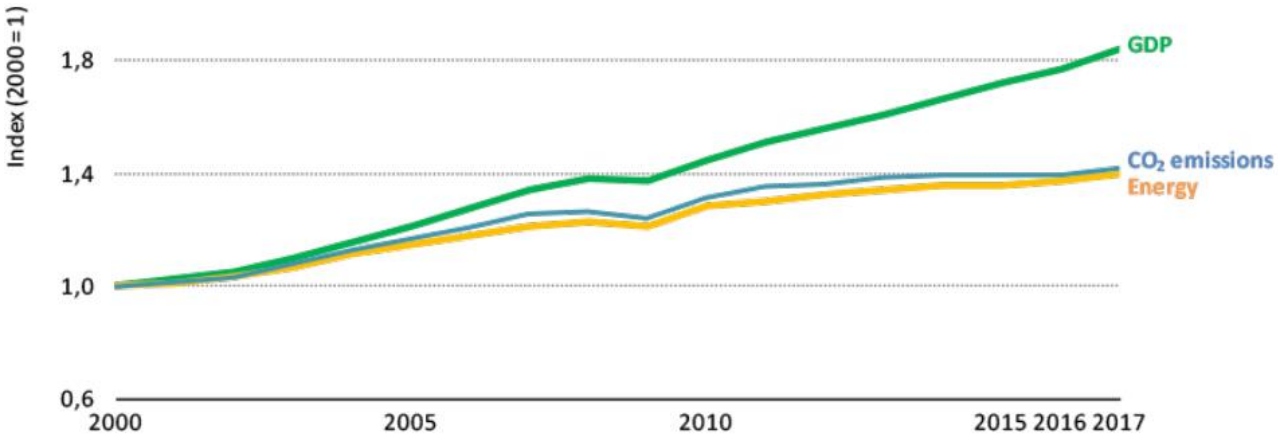

Figure 1. Global GDP, energy demand and energy-related carbon dioxide emissions, 2000-2017 (Adaption of [4])

In light of this evidence it is critical to deploy the actions to guarantee future energy security and GHG emissions reduction to meet the objectives of the Paris Agreement to combat catastrophic climate change. To do so it is necessary to increase the share of energy generation that comes from renewable and clean energy sources and ensure efficient energy use. European energy policies have clearly identified the potential of electric energy storage (EES) to help reaching these targets. The reason of focusing on electrical energy storage is linked to the nature of most forms of low or zero carbon energy generation that differ from the fossil fuel dominated in traditional electricity system [5], [6].

Renewable energy sources (RES) are projected to be the fastest growing source of energy, with consumption rising at a rate of 2.3% per year between 2015 and 2040 worldwide [7]. Furthermore, the existing European policy mandates achieving a 20% share for renewable energy by 2020 and at least 27% by 2030 [8]. European Union is committed to advancing renewable energy and lays out a plan to decarbonize energy system in the E.U. by the middle of the century in an effort to limit the effects of climate change [9].

As the renewable energy market grows, the market for EES systems, especially for small and dispersed ones, also expands. The numerous studies indicate that the introduction of renewable energy, hybrid electric vehicles (HEV), smart grids and expanding of consumer portable electronic sector (laptop computers, portable media players, GPS etc.) are the key driven forces for the growth of electric energy storage system [10], [11]. Currently, electrochemical storage is one of the most rapidly growing market segments for stationary applications, with batteries and supercapacitors as dominant technologies [12]. These technologies due to their dissimilar charge storage mechanisms, demonstrate different properties. Batteries, with faradaic reaction represent a high energy density device with slow and steady discharge rate, while supercapacitors (SCs) with a non-faradaic process charge and discharge quickly for low energy demands. The hybridization of batteries and SCs in a single device is a promising combination which allows achievement of both higher energy and power densities [13], [14], [15], [16]. Therefore, the commercialization of hybrid supercapacitors requires development of novel electrodes and suitable supercapacitor configurations.

The aim of this research was to develop and to test new electrodes based on nanostructured metallic foams (NMFs) of Ni and Ni hydroxide for application as electrode for hybrid supercapacitor. Nickel became an attractive candidate as an electrode material in supercapacitors of hybrid configuration because of demonstrated excellent performance in alkaline electrolyte coupled with low fabrication cost and natural abundance.

Aim and goals of the thesis

The main objective of this thesis is to develop novel methods for manufacturing Nickel based electrode aiming to achieve higher performance output. The work included the following tasks:

- Understanding electrochemical behavior of metallic foams in selected electrolyte environment.
- Characterization of the porous morphology of selected foams and its further re-designing/improvement for energy storage applications through the advanced electrodeposition techniques.
- Filling the porous structure with an active material by means of chemical/electrochemical techniques in order to produce a composite electrode material.
- Integration a composite electrode into electrochemical cell and its electrochemical response characterization in selected electrolyte environment.

1. Emerging needs for Electrical Energy Storage (EES)

This section presents a brief introduction on the role of electric energy storage, in particular batteries and supercapacitors systems, in modern energy system.

1.1 In grid

As stated in a study recently issued by the European Parliament Research Service, electric energy storage can facilitate the increased penetration of renewables. In the past two decades Renewable energy production in Europe has increased significantly as new technologies became commercial and the importance of sustainable energy became understood. Importantly, the majority of the growth in renewable energy over the past 15 years has come from wind and solar [17]. Wind and solar energy is plentiful and highly sustainable. There is, however, a challenge impeding greater adoption of wind and solar energy sources to the electric network. It is well known, that modern alternative current grid requires instant match of electricity demand to supply for the reason of stability. The grid imbalance has a negative impact with consequences including blackouts, loss of industry production. Traditional electricity system (based on fossil fuels) stores fuels stock on site to immediately generate electricity when it is needed to match supply with demand. For the same purpose commonly, the water in a reservoir behind a hydropower dam can be used [18]. Unlike traditional fossil fuel power plants or certain renewable sources such as hydroelectric and geothermal that can be controlled to meet demand, solar and wind power is produced intermittently when the sun shines and the wind blows. Therefore, there is often a problem of matching the supply to demand. To balance the system, EES offers the potential to reserve excess generation for later use. In so doing, stored electrical energy transforms into a commodity comparable to coal, oil and gas [10]. Among different types of storage solutions, electrochemical storage is now the fastest growing storage technology and it is expected that the stationary battery storage will grow from 1.9 GW worldwide now to around 175 GW by 2030 [12].

1.2 In transport

Electrical energy storage is not only significant at the grid level. EES is playing a major role in reducing fossil fuel consumption in the transportation sector through the development of hybrid-electric and fully electric vehicles [6]. These vehicles use EES systems comprised of batteries and supercapacitors, from which the stored electrical energy can instantly be extracted to power a vehicle. Using regenerative braking system, the electric motor also works as a generator. When braking, some of the wheels' kinetic energy is transformed into electrical energy and gets stored in supercapacitors and batteries. From the SCs the stored energy can

be used to accelerate a vehicle, while the energy stored in the batteries can then be utilized by other applications such as air-conditioning or lights. Such kind of system significantly prolongs battery lifetime and improves the overall efficiency of the EES of the car, and therefore improve the overall performance of the vehicle [19] [20]. To fully charge HEV is plugged into the grid. As additional advantage, battery from the electric vehicles may help to balance out the grid by charging up when electricity is abundant and injecting electricity back during peak hours [11].

1.3 Portable devices

Next, EES plays a vital role powering the portable electronic devices that have become ubiquitous and indispensable in modern life. Battery and supercapacitor based EES have developed significantly in recent years to match consumer demand for more powerful and portable personal communication devices [11]. Furthermore, progress in modern electronics with different wireless technologies and sensor networks, require development of smaller though powerful EES systems. To reduce the dimensions of the storage system, the battery can be combined with high power component like supercapacitor [21], [22].

1.4 Electrification off-grid locations

Finally, EES can contribute to escalating energy excess in many developing countries as well as to the remote locations that cannot accessed by electricity grids. It was reported, that nearly 13% of the world's population, or 1.1 billion people, mainly in Asia and sub-Saharan Africa are still living their daily lives without electricity. Battery systems in combination with solar photovoltaics or mini-wind turbines can provide a reliable off-grid electricity supply. Accelerating energy access is vital for achieving sustainable development goals [7].

Clearly, EES systems are relevant today and will only grow in importance in the coming decades. Therefore, it is necessary to develop advanced, environmentally friendly, efficient and low-cost energy storage solutions. In the following section, we will contextualize EES devices within the wider category of energy storage systems and then discuss the current state of the art of commercial EES devices.

2. Classification of Electrical Energy Storage Systems

Electrical energy storage is a process of converting energy into a different form that is possible to store and reserving it for later use as electrical energy; then the stored energy can be converted into electricity when needed. Energy storage provides a broad range of technologies, which possesses its own characteristics and suitable for various applications. Generally, these technologies can be classified according to the form of energy used to store energy. The range includes mechanical (pumped hydroelectric storage, compressed air energy storage and flywheels), chemical (hydrogen storage with fuel cells) and electrochemical (rechargeable

batteries and supercapacitors) [11] as shown schematically on the Fig. 2. Further this section provides selection of the main existing electrical storage systems with a brief description of functioning, following the above order.

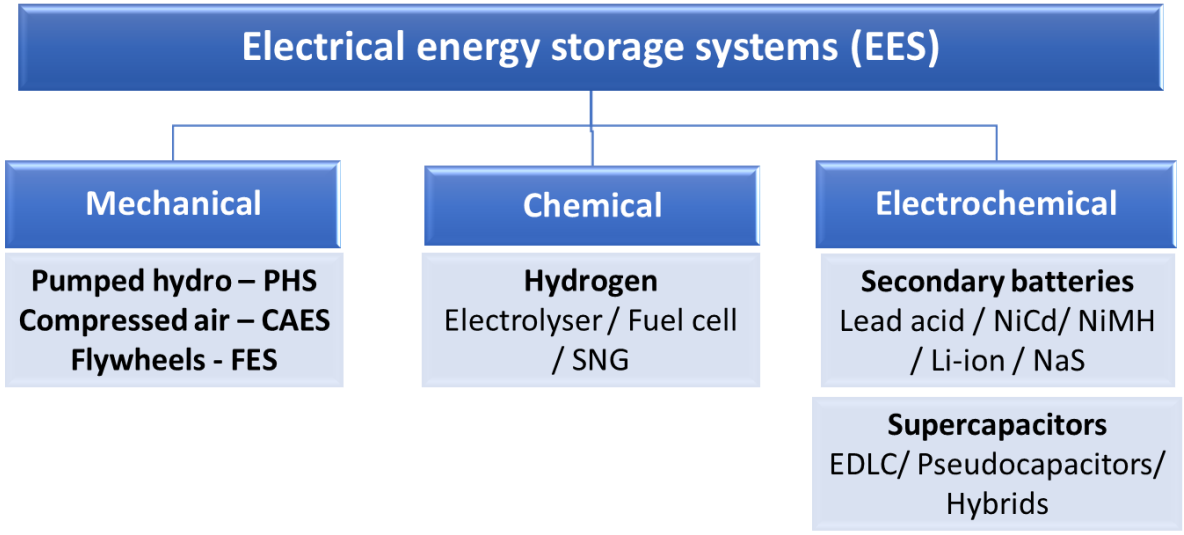

Figure 2. Classification of EES

2.1 Mechanical Energy Storage

Mechanical energy storage devices work on the principle of storing energy in a kinetic or potential form until it is needed and subsequently convert it into electric power.

2.1.1 Pumped hydroelectric storage

Pumped hydroelectric storage (PHS) is the most mature and widely adopted method of energy storage for grid applications, which are capable to provide energy balancing, reserve power, and stability functions. PHS total installed storage power capacity is 96% of the total of 176 GW installed globally. Conventional PHS system principally consists of two water reservoirs at different elevations, turbine with generator and electrically powered pumps. During hours when electricity demand is lower, the pumps deliver water to a higher-potential reservoir (charging), where the water stored until power is needed. During peak-hours, when the demand is high, the water flows down to the lower reservoir through hydroelectric turbines, which generates electricity. The capacity of PHS system is proportional to differential in height between two reservoirs and the amount of water can be stored [23] [24]. A simplified schematic of a PHS system is depicted in Fig. 3.

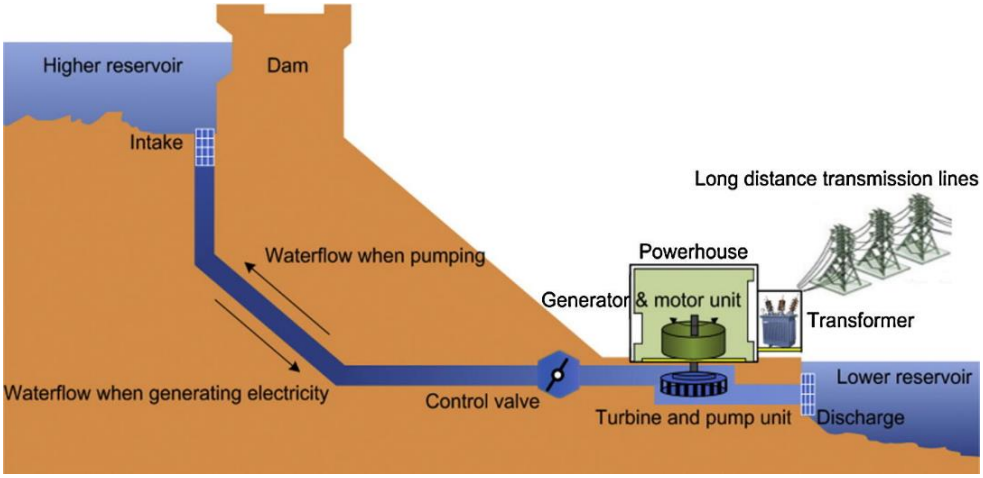

Figure 3. Schematic illustration of PHS (modified from [24])

2.1.2 Compressed air energy storage (CAES)

In CAES systems air serves as a storage medium. To charge the system the plant's generator, powered by off-peak/ low-cost electricity, produces energy required to compress air within a pressurized holding reservoir. The reservoir could be either an underground structure (abandoned mines, aquifers, salt caverns) or an above-ground system of vessels or pipes. To discharge the system, the compressed air is released through a gas turbine-generator, producing electricity. Heat generated in the compression process may be stored and transferred back to the air during expansion to improve efficiency and reduce the quantity of natural gas required by the gas turbine [11]. Fig. 4 shows the schematic illustration of a CAES system.

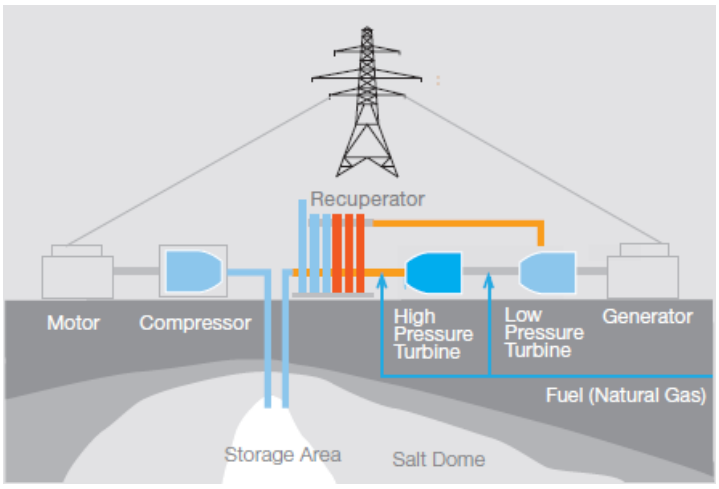

Figure 4. Schematic illustration of CAES System (Modified from [25])

2.1.3 Flywheel

Flywheels energy storage systems is a kinetic-energy based technique that can achieve relatively high power-density up to MWs without possessing great energy density or the ability to store energy over long periods. Flywheels store kinetic energy in the form of a rotating mass and release out upon demand. A mass spins fast without resistance using magnetic bearings. In order to reduce the friction losses usually a flywheel is placed inside a vacuum chamber. To charge, a flywheel operates as a motor, using electrical energy to spin the wheel. By speeding up the flywheel an electro-mechanical transmission devise is capable of converting electrical power into kinetic energy (charging). To discharge, flywheel operates as a brake slowing down the system, converting kinetic energy into electricity. [11] [6].

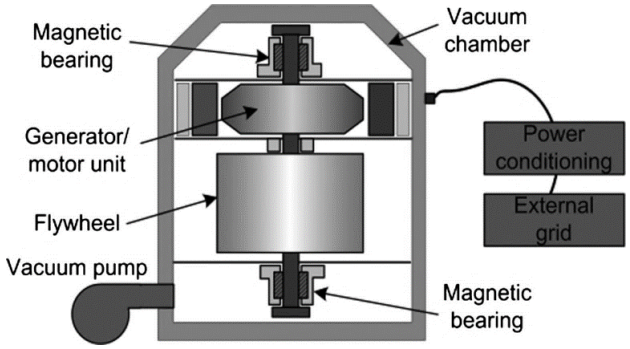

Figure 4. Schematic illustration of a flywheel energy storage facility (modified from [24])

2.2 Chemical Energy Storage

This section is limited to describing systems that produce and store hydrogen or derivative gas compounds such as synthetic natural gas (SNG). The most basic system consists of an electrolyser, a hydrogen receiver and a fuel cell. The electrolyser using electrical power divides water molecules into hydrogen and oxygen. The hydrogen is then stored in a receiver, as a pressurized gas. To keep the process sustainable, the water from domestic use and the low carbon electricity as an input are desired. When needed, electricity is produced from the fuel cell via reverse process when hydrogen gas is combined with oxygen to form water. In a SNG application, hydrogen gas from the electrolyser is combined with carbon dioxide to produce methane gas [26].

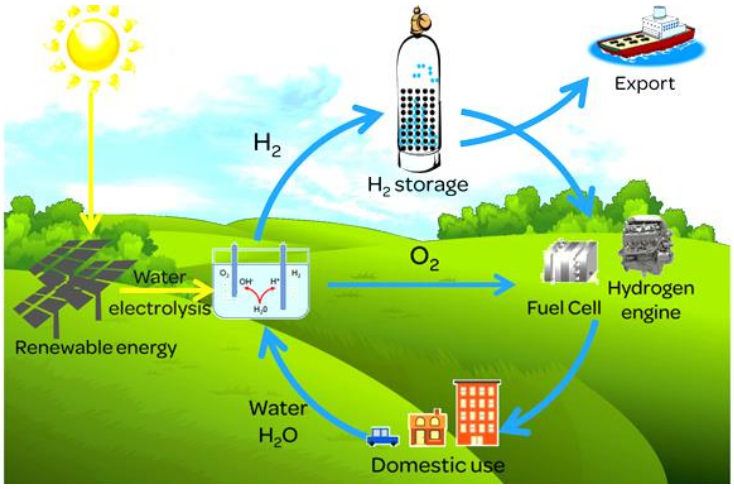

Figure 5. Schematic illustration of hydrogen energy storage cycle (modified from [27])

2.3 Electrochemical Energy Storage

2.3.1 Battery

Batteries are one of the most widely used electrochemical energy storage technology. The working principle of battery is based on conversion between chemical and electrical energy. A basic battery configuration consists of one or several electrochemical cells, connected in series or in parallel, or both depending on the desired output voltage from electrochemical reactions. Each cell includes one positive (cathode) and one negative (anode) electrode separated by porous membrane and an electrolyte. The electrolyte can be at solid, liquid or viscous states. The electrochemical reactions occur at both electrodes simultaneously and can be formulated with Eq. 1, where electron $\bar{e}$ is transferred between oxidized species Ox and reduced species Red [28].

$$Ox + e^- \rightleftarrows Red \quad (1)$$

During discharge, anode is oxidized (loosing electrons), and the cathode is reduced (consuming electrons). Concurrently the ionic species generated at the electrodes (cations and anions) flow through the electrolyte under the influence of electric field. This oxidation-reduction cycle creates a flow of electrons that can form a useful electric current to power an electric load connected through an external circuit. To charge the cell, the external load is replaced with an applied voltage causing the electrochemical reactions at the electrodes to reverse and electrons to flow in the opposing direction.

The main difference between different battery is the materials used as electrodes and electrolyte, which determine the properties of the batteries. Generally, batteries can be divided into two main groups: primary

and secondary. In a primary cell theoretically, chemical reactions are irreversible and therefore the recharging process has very low outcome and can be repeated only a few times with occurring damage of the electrodes and high risk of short circuit. Therefore, primary batteries are considered as non-rechargeable and can be used just once. In secondary cell chemical reactions are reversible and therefore the cell can be recharged. Note, that during charging and discharging processes in rechargeable battery, simultaneous chemical interconversions of the cathode and anode are often accompanied by phase changes of the reagent. In practice phase transformation often introduces material with a different conductivity into the system. This change in electrode material resistance leads to kinetic irreversibility, which in practice results in limiting the cycle life of a battery [29].

This section is presenting an overview on the most common battery technologies that are either in use and/or potentially suitable in industry, transport or daily life. The selection includes lead acid battery, nickel-based battery, sodium sulphur battery and lithium-ion battery. The chemical reactions which occur in these battery types simultaneously on anode and cathode are presented in the Tab. 1 [30], [24].

Table 1. Chemical reaction and unit voltage

Battery type	Chemical reactions at anodes and cathodes	Voltage
Lead-acid	$Pb + SO_4^{-2} \leftrightarrow PbSO_4 + 2e^-$ $PbO_2 + SO_4^{-2} + 4H^+ + 2e^- \leftrightarrow PbSO_4 + 2H_2O$	2.0 V
Li-ion	$C + nLi^+ + ne^- \leftrightarrow Li_nC$ $LiXXO_2 \leftrightarrow Li_{1-n}XXO_2 + nLi^+ + ne^-$	3.7 V
NaS	$2Na \leftrightarrow 2Na + 2e^-$ $xS + 2e^- \leftrightarrow xS^{-2}$	~2.08 V
NiCd	$Cd + 2OH^- \leftrightarrow Cd(OH)_2 + 2e^-$ $2NiOOH + 2H_2O + 2e^- \leftrightarrow 2Ni(OH)_2 + 2OH^-$	1.0-1.3 V
NiMH	$H_2O + e^- \leftrightarrow 0.5H_2 + OH^-$ $Ni(OH)_2 + OH^- \leftrightarrow NiOOH + H_2O + e^-$	1.0-1.3 V

Lead-acid

Lead-acid battery is a well-established technology and attractive because of their low cost and high reliability. The typical applications are automobile starter batteries, grid storage systems, emergency power supply systems and uninterrupted power supplies. The cathode is made of lead dioxide PbO_2, the anode is made of lead Pb, immersed into the sulfuric acid electrolyte H_2SO_4. These materials are considered as potentially hazardous; however, the technology of the recycling is fully in place. Lead-acid batteries have several drawbacks including low specific energy and power, toxicity, reduced capacity at high discharge rates, low depth of discharge and limited life cycle (fewer than 500) [11], [6] .

Lithium-ion

Lithium-ion batteries are widely used to powering portable electronics. The cathode in this type of battery is made of a lithium metal oxide, such as $LiCoO_2$ and $LiMO_2$, and the anode is made of graphite. The electrolyte is usually based on Li salt in organic solution. Lithium-ion batteries have a high energy density compared to other technologies because due to the higher operating voltage of around 3-4 V per cell [31]. Coupled with the ability to meet a wide range power needs, lithium-ion batteries are finding a growing number of applications including electric vehicles and grid storage. Several disadvantages of lithium-ion batteries limit their adoption including high material costs and safety issues caused by thermal instability of the electrode [11] .

Sodium sulfur

A NaS battery cell consists of molten sodium as the anode and molten sulphur as the cathode, separated by the solid electrolyte beta alumina. The operating temperature of the cell is between 300°C and 350°C to keep the electrodes in liquid states, ensuring a high reactivity. Practically, the batteries are kept under charge so that they will remain molten be ready for use when required. The electrode materials are non-toxic making recycle possible. These batteries attracted lots of attention due to high energy density compared to many other batteries, quick response capability and high cycle life, which make them a potential asset for grid stabilization and hybrid electric vehicles. However, the limitations are high annual operating cost (2000 $/kW) and high operation temperatures [32].

Nickel-based battery

Various nickel batteries have had significant commercial success. Historically, nickel-cadmium batteries exhibited improved performance compared with lead-acid batteries and were used in many applications despite being more expensive. In NiCd one of the electrodes if made of nickel hydroxide, and the second one of Cd hydroxide. Aqueous alkaline solution serves as an electrolyte. The main drawback is that NiCd battery suffers from the memory effect, meaning that capacity can significantly drop if the battery was charge after being only partially discharged. Recently, NiCd batteries have seen reduced usage due to the toxicity of Cadmium [31], [32].

Nickel-hydrite (NiMH) is similar to NiCd, with a difference that here hydrogen-absorbing alloy is used as a negative electrode instead of Cd. NiMH batteries have become commercialized in the last 20 years and are now the leading battery type for electric vehicles due their relatively high energy density and safety compared to lithium-ion batteries. NiMH batteries are also suitable for use in personal electronics; however, they have largely been replaced in that application with lithium-ion batteries. NiMH batteries are most relevant today because of the promise they hold in electric vehicle applications [10].

2.3.2 Supercapacitors

Electrochemical capacitor, also known under commercial names as “supercapacitor” or “ultracapacitor”, is a type of capacitor that is able to store and deliver energy at relatively higher rates as compared to batteries and are able to go through many cycles without degradation.

Generally supercapacitor configuration consists of two electrodes (positive and negative) separated by a conductive electrolyte which is in direct contact with the surface of electrode, two current collectros (positive and negative) and porous membrane. The function of the membrane is to prevent short circuit between the electrodes of opposite polarization, while allowing ionic diffusion through its porosity to insure the ionic conduction.

Variations in the storage mechanism and choice of electrode material lead to various classifications for supercapacitors. Depending on the type of charge storage mechanism, SCs can be divided into electrical double layer capacitors (EDLC) and pseudocapacitors. The former is based on electrostatic accumulation of charges at the electrode–electrolyte interface, while the later utilizes fast surface and subsurface faradaic reaction.

Depending on the type of cell configuration, supercapacitors can be divided into symmetric, asymmetric and hybrid. A symmetric device consists of two identical supercapacitor-type electrodes (EDLC or pseudocapacitive). It is noted that, the dimensions, the mass and the composition of both electrodes must be equal in order to exhibit equivalent performance on both electrodes. SC with two activated carbon electrodes (EDLCs) is the simplest and most commercially available symmetric type. Asymmetric SCs include every combination of positive and negative electrodes whenever there is any difference between their properties (storage mechanism, mass, dimensions, composition etc.). The purpose of asymmetric configuration is to enhance the energy density of supercapacitor by increasing the cell working voltage. Finally, hybrid capacitors are composed of an EDLC electrode and a battery type electrode, potentially improving the overall performance of the device by combining the benefits of both systems [13], [33], [34].

EDLC

EDL capacitors store charges by the means of an electrical double layer, a so-called Helmholtz plane, at the interface between the electrically conductive electrode and an electrolyte. This layer results from electrostatic attraction between electrolyte ions and charges accumulated on the electrode surface [35].

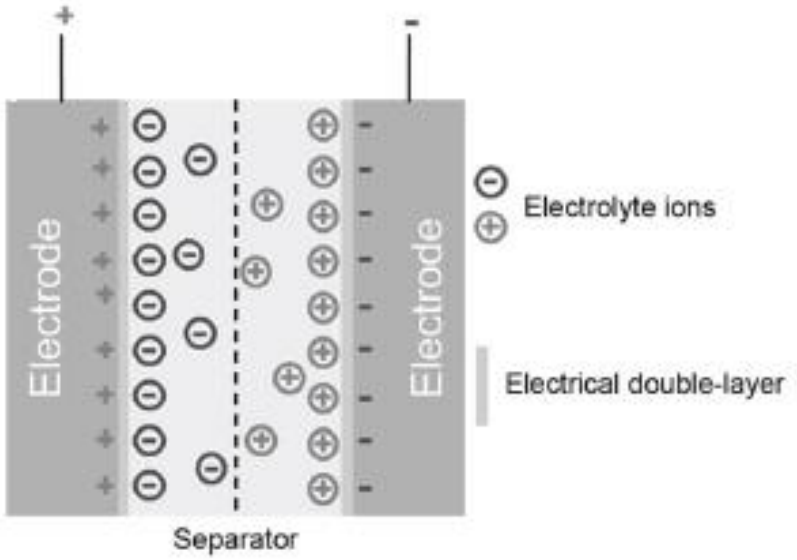

Figure 6. Schematic illustration of an EDLC in its charged (modified from [35])

When an external electric field is appplied to the system, the process of reversible adsorption of electrolyte ions onto the electrical double layer proceeds simultaniously on both electrodes and corresponds to the charge and discharge of EDLC (Fig. 6).

Compared with a battery, EDL material due to the physical reaction in nature can respond faster to the change in charge potential and therefore has a faster charge-discharge rate, and much higher power density performance. The absence of faradic reactions also eliminates kinetics irreversibility which usually leads to the deterioration of the reagent material during cycling. This means that EDLCs can sustain a greater number of cycles than a typical battery [36].

Since no charge transfer between electrode-electrolyte interface occurs and no chemical changes of electrode reagents are involved, the EDLC electric storage mechanism represents a true capacitance effect. Following a general mathematical expression for conventional parallel-plated capacitor, a double layer capacitance can be calculated with the equation presented below [35]:

$$C = \varepsilon_r \varepsilon_0 A/d \quad (2)$$

where ε_r (a dimensionless constant) is the relative dielectric constant of electrolyte; ε_0 (= 8.854×10^{-12} F m^{-1}) is the dielectric constant of the vacuum; d (in m) is the charge separation distance (double layer thickness); and A (in m^2) is the surface area of the electrode accessible to the electrolyte ions.

From Eq. 2, it is evident that the value of the double layer capacitance is greatly dependent on the specific surface area of the electrode. In other words, the electrode the materials with a very large specific surface

can store more charges providing higher energy density to the system. With respect to morphology as well as high electric conductivity, carbon materials and their derivatives, including activated carbon (AC), porous carbon, carbon nanotubes, and graphene, are the most commonly used materials for designing EDLCs.

Materials for EDLC

The most widely used electrode material is AC and that is due to its large surface area, natural abundancy and low-cost. AC can be synthesized from various types of from carbon-rich organic precursors such as wood, coconut shells etc. Depending on the production methods, AC demonstrate various pore sizes that can be classified as micropores (< 2 nm), mesopores (2 - 50 nm) and macropores (> 50 nm). The reported specific surface area of AC is up to 3000 $m^2 g^{-1}$. However, experiments obtained relatively low specific capacitance of up to 300 F g^{-1} in aqueous electrolytes and around 150 F g^{-1} in organic electrolytes. Since the amount of stored charge depends on number of active sites in contact with electrolyte, the lack of pores uniformity may lead to poor material utilization. Therefore, estimated useful specific surface area is usually in the range of 1000 – 2000 $m^2 g^{-1}$. For carbon nanotubes, on another hand, it is possible to obtain different nanostructured formations controlling fabrication condition. CNTs have fully accessible by electrolyte ions external surface area, formed by interconnected mesopores, and high electric conductivity and mechanical stability. However, CNT possess small specific surface area of < 500 $m^2 g^{-1}$ which leads to a low energy density compared to AC. Finally, graphene has attracted lots of attention for energy storage device applications due to due rate and cycle capability and improved capacity coupled with electrical conductivity, chemical stability. Graphene is a one atom thick layer made of bonded carbon atoms. Recently developed graphene demonstrated high specific surface area of 2630 $m^2 g^{-1}$. If the entire specific surface area is efficiently utilized a capacitance of graphene may reach up to 550 F g^{-1} [33].

Pseudocapacitors

The link between battery and EDL energy storage was found through a phenomenon called pseudocapacitance. In this type of material, electron transfer across the double layer originates from the fast-reversible surface Faraday redox reaction occurring at the interface between the electrode material and electrolyte, as well as in the bulk near the surface of the electrode (Fig. 7). Despite the faradic nature of the charge storage process, the electrochemical signature of pseudocapacitive material is similar to that of EDLC electrode [15]. Being pseudocapacitive in nature, metal oxides (MnO_2, Fe_3O_4, RuO_2, MoO_3, PbO_2 and Fe_2O_3 etc.), as well as electronically conducting polymers, are considered to be promising electrode materials, as their capacitance usually significantly surpasses the double-layer capacitance reachable with carbon materials. On another hand, in comparison to EDLCs, the power capability is usually significantly reduced due to the low conductivity of metal oxides. Moreover, some irreversible transformation of material during the charge-discharge process can occur shortening the lifecycle of the electrode [14].

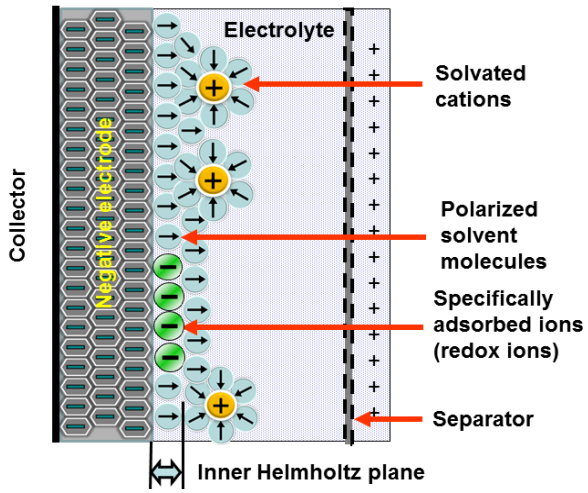

Figure 7. Schematic illustration of the charge storage phenomenon in a pseudocapacitor (Adaption of [37])

Hybrid supercapacitors

Hybrid electrochemical system constitutes of a battery-type electrode (for higher energy density) and capacitive electrode (for higher power density and lifecycle). It has been suggested, that the concept of hybridization can bring important outcomes for the overall performance of the cell in terms of voltage window and capacity/capacitance if compared with standard symmetric and asymmetric configurations. In general, hybrid devices represent an important future direction for energy storage technologies, therefore their different designs shall be more explored [13], [14], [15], [16].

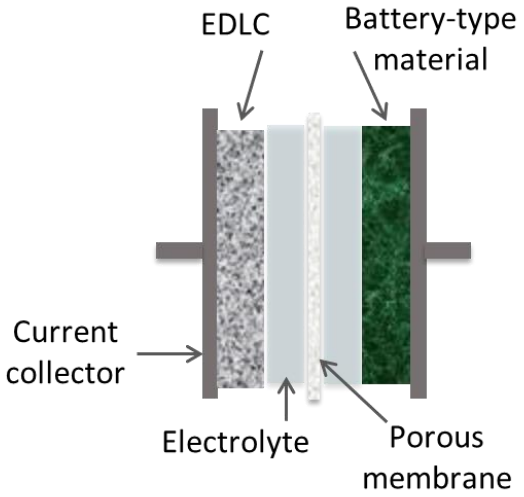

Figure 8. Schematic illustration of supercapacitor of hybrid configuration (modified from [38])

Materials and Electrolytes for Hybrid Supercapacitors

Electrolytes widely used in hybrid supercapacitors can be classified as aqueous and organic. Organic electrolytes usually include Li-ion battery electrolytes ($LiPF_6$, $LiBF_4$) or Na-ion battery electrolytes ($NaClO_4$, $NaPF_6$), whereas aqueous electrolytes can be acidic (H_2SO_4, CH_3SO_3H), alkaline (KOH, NaOH) or neutral (Li_2SO_4, Na_2SO_4).

Aqueous electrolytes are considered environmentally friendly and low-cost; however, the voltage limit of aqueous electrolytes is relatively low due to the water decomposition at 1.23 V. In contrast cells based on organic electrolytes can reach voltages of 2.7 V and higher. The main drawback of organic electrolytes are toxicity and high production costs due to the process of purification from water, which is required to achieve the higher cell voltage avoiding degrading the electrolyte [33]. Therefore, for certain applications a feasible solution to achieve higher working voltage in aqueous electrolytes is to use two different electrodes. Among aqueous electrolytes, acidic are normally used in the hybrids of lead–acid battery and SC; alkaline electrolytes are typical for devices where alkaline battery electrode (such as Ni-/Fe- oxides/hydroxides) is paired with carbon electrode; and neutral electrolytes are mainly utilized in aqueous Li-ion and Na-ion [13].

The concept of hybridization of SCs and battery was firstly introduced by combining in aqueous electrolyte KOH activated carbon electrode C with Ni(OOH). The device demonstrated improved energy density compared to symmetric carbon EDLC operating in aqueous electrolytes with a maximum operating potential of 1.4 V [39]. To date, Ni-based compounds and their composites with carbon or conductive polymers are the most popular cathode materials for aqueous alkaline hybrid supercapacitor. Among those Ni hydroxide takes special place due to high theoretical specific capacitance (2082 F g^{-1}) and stability in strong alkaline electrolyte. The benefits which include reliability, simplicity, easy synthesis, natural abundancy and low cost, make nickel hydroxide among the most promising electrode material for hybrid supercapacitor [40], [41].

3. Characteristics of different energy storage technologies

The previous sections presented an overview of the most frequently used technologies to store energy. The relevant parameters which define EES devices are: storage capacity; high efficiency; time of response; long lifetime under cyclic conditions, power density; energy density; low maintenance and be able to meet environmental concerns. It is also important to consider the level of technical maturity of EES technologies which are linked to the level of commercialization, the technical risk and the related economic benefits. These are considered the most relevant characteristics for the purposes of this thesis, though other characteristics may be additionally needed, depending on the application.

From this overview, it can be seen each EES technology possess different characteristics that are best suited to certain applications. Therefore, it can be concluded that none of the existing storage technologies can be considered as a superior over the other storage systems [11].

With a suitable combination of different technologies, EES can potentially meet most of the technical requirements for various power system and network operations. Recent research study shows, that stationary energy storage industry is now exploring grid-scale hybrid solutions, which combine several energy storage technologies with complementary operating characteristics. These systems deliver power capacity, energy duration, and cycle life in a single system that is not achievable by any one energy storage technology operating individually. Global installed power capacity of such kind of system is expected to reach up to 2.1 GW in 2026 [42].

Among presented EES, it can be seen on the Fig. 9, batteries and supercapacitors are dominating in small (100kW) and medium (from 100 kW to 100 MW) scale applications. It's been reported that with recent changes related to the energy sector transformation (see Chap. 1) the global share of electrochemical energy storage systems has increased by 15% from 2017.

Although the battery technology significantly advanced, the relatively low cycling times and high costs have been still limiting implementation of batteries for larger scale applications [12]. The full life cycle, from raw materials to disposal or recycling of batteries must also be taken into account if toxic chemical materials are used. The advantages of supercapacitors are high power density, efficiency and long operation lifetime. SCs can charge and discharge for more than one million cycles. However, the main drawback of this devices is having low energy density [24].

The combination of supercapacitor and battery technologies can bring beneficial characteristics including relatively large storage capacity and very fast charge/discharge rates. To achieve both characteristics in one device is a challenging task that can be potentially solved by integrating a battery electrode and capacitive

electrode in a single supercapacitor device [13]. As discussed earlier in Chap. 2.3.2, an energy storage device with such kind of configuration is called hybrid supercapacitor and offers a promising way to achieve higher energy and power density, as shown in Fig. 10.

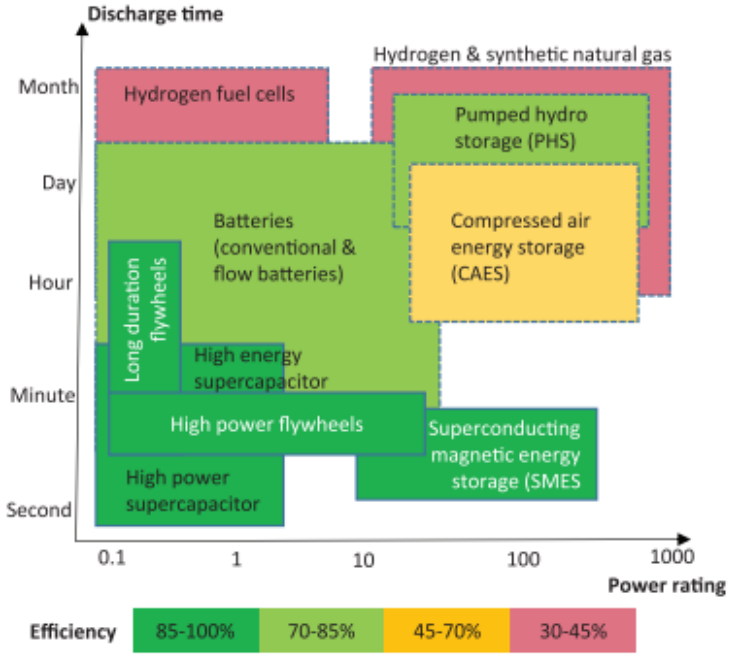

Figure 9. Overview of the characteristics of energy storage technologies according to performance characteristics (adapted from [43])

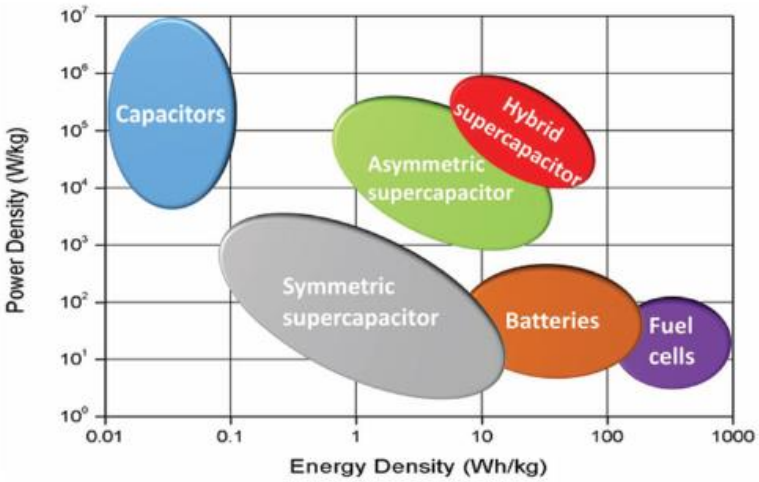

Figure 10. Ragone plot of different EES (modified from [16])

In this thesis the research was focused on developing and testing a battery-type electrode based on Ni hydroxide for the hybrid supercapacitor. Therefore, it is important to understand the specific operation principle of this device. The following section provides detailed information on this concept.

3.1 Working principle of typical hybrid $Ni(OH)_2$//AC supercapacitor

A working principle of hybrid supercapacitor, where the positive electrode is made of nickel hydroxide and the negative electrode is made of activated carbon is demonstrated on Fig. 11. The aqueous solution of KOH is used as an electrolyte.

The half-cell electrochemical reaction on the positive electrode during charge-discharge process can be shown as follow:

$$NiOOH + H_2O + e^- \rightleftarrows Ni(OH)_2 + OH^- \quad (3)$$

As stated in the literature, the redox reactions in nickel hydroxide $Ni(OH)_2$ electrode are controlled by the solid-state proton diffusion. When the electrode is charging, bi-valent Ni is oxidized into the tri-valent state forming NiOOH. The released proton H^+ due to the applied potential difference is diffusing from the bulk of the solid phase into electrode/electrolyte interface and combines with hydroxide anion OH^- forming H_2O.

Simultaneously, electrons are transferred into the external circuit through the current collector. During the discharge, the reverse reaction takes place. Water at the electrode surface is spliced into H^+ and OH^-, next the deprived proton intercalates to the electrode structure to recombine with nickel oxyhydroxide to form $Ni(OH)_2$ and neutralize the electron which entered through the electrode/current collector interface, maintaining the electrostatic balance with the opposite electrode. On the other hand, during charging, the negatively charged AC electrode adsorbs electrolyte cations K^+ to the electric double layer. The reverse process arises during the discharge [44]. The process of charge discharge is depicted on the Figs. 11-12.

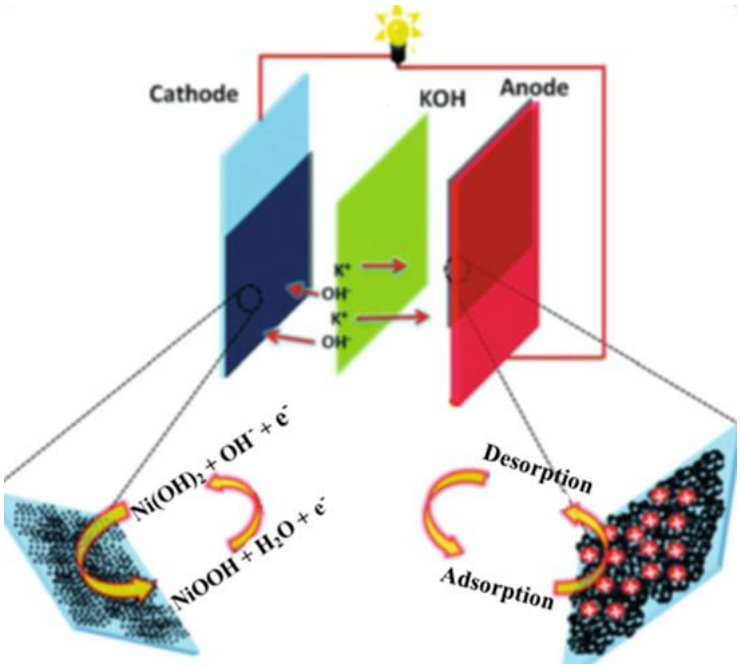

Figure 11. Schematically illustration of a working principle of hybrid supercapacitor with $Ni(OH)_2$ as a positive electrode and AC as a negative electrode, separated by KOH solution as an electrolyte (modified from [14])

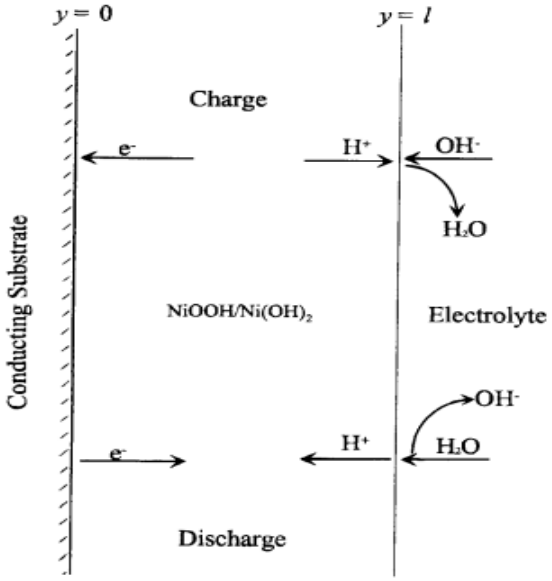

Figure 12. Schematic diagram of the charge/discharge mechanism in nickel hydroxide electrode (modified from [44])

4. Nanostructured electrode supports

Since the response of the battery-like active material is subjected to diffusion-controlled processes, in order to increase the capacity and rate capability of the electrode it is necessary to ensure both: high ionic conductivity within the matrix, as well as highly electrically conductive network to decrease the charge transfer resistance [44]. Both requirements can be achieved by designing an electrode with the active material directly placed on the 3-dimensional (3D) conductive support. In particular, 3D-nanostructured metallic foams (NMFs) have been widely investigated to be used as electrode supports due to their high electrical conductivity and mechanical stability [45]. To date, several methods for NMFs fabrication are available, including hard-template method, electrochemical de-alloying and electrodeposition [46]. Yet not all the production processes are cost-effective. Synthesis of nanostructured porous morphology by de-alloying is a multiple-step process based on the etching of the more active component from the prepared alloy. Typically, however, it has poor control over pores size and distribution [47], [48]. In case of hard-template method the structure is dictated by the ordered porous structure of the template which is then removed by physical and chemical methods, such as dissolution, sintering, and etching. However, it can be complicated to remove the template material, which may cause contamination of the final product [49].

Electrodeposition technic offers wide range of morphologies that can be achieved by adjusting the process parameters. In particular, electrodeposition by meaning of “dynamic hydrogen bubble template” (DHBT), where electrochemically generated hydrogen bubbles serve as pore forming agent, has the advantage of producing nanoporous metallic structures in clean, fast, low-cost and simple way [46]. Furthermore, electrodeposited NMFs are typically formed on the electronically conductive substrates (current collectors). Different metallic materials have been widely explored as conductive current collectors for different electrochemical energy storage devices, including supercapacitors and rechargeable batteries. In particular, commercial nickel foam (CNF) have attracted great attention due to its excellent electric conductivity, low cost, hollow 3D structure (Fig.13) with high surface area [50].

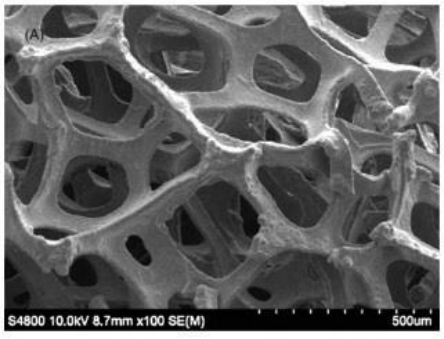

Figure 13. SEM micrograph of commercial nickel foam at magnification 100X (taken from [50])

However, commercial foams are still a large-scale structure to be used bare as an electrode support for a sufficient number of active sites. By growing NMF directly into pores of commercial metallic foams, significant increase of the specific surface area can be achieved. NMF electrodeposited on commercial foam are schematically depicted on Fig. 14. In this case electrodeposited NMF has two functions as a supporting matrix for the active material, as well as a current collector. As a result, favourable nanostructure, which combines a large specific surface area with an appropriate pore size distribution, potentially increasing the number of redox reactions occurring in the electrode surface and therefore overall performance of the electrode [45]. Additionally, increased surface area for deposition allows to decrease the thickness of the active material, facilitating charge and mass transfer reactions. This effect is especially important in case of the materials with low electric conductivity such as of majority of the metal oxides. On the other hand, direct contact between active material and current collector shortens the electron pathway, potentially increasing electron transfer efficiency during charge-discharge process [51].

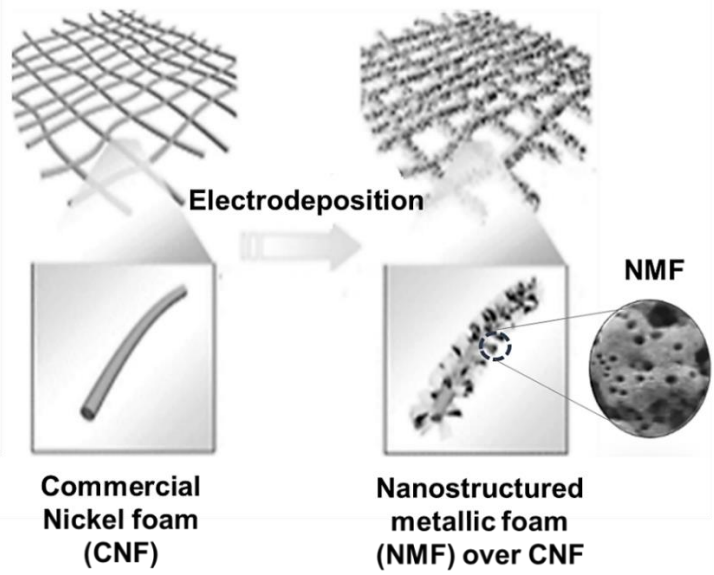

Figure 14. Schematic illustration of electrodeposition of nanostructured metallic foam NMF over commercial nickel foam CNF

4.1 Dynamic hydrogen bubble template electrodeposition technique

The electrodeposition of metals is a technique used in electrochemistry by which metallic ions from an electrolyte solution are reduced onto conducting substrate forming a solid deposit [52]. The experiments are typically performed in electrochemical cell connected to the power source (i.e. voltage/current). Here, the working electrode (cathode) is the surface to be coated and the counter electrode (anode), usually made of inter material (e.g. Pt, Au, graphite, glassy carbon), are immersed into electrolyte. The electrolyte is usually

an aqueous solution of metallic salts. Under the influence of electric field, metal ions M^{z+} from the electrolyte are transported towards the cathode surface, where they gain electrons ze^- forming uncharged elements or compounds M, which typically remain adhered at the surface of the working electrode. Normally, to grow metallic film the electrodeposition process is conducted within the potential window of the electrolyte. DHBT method, however, in driven by high overpotential (or current densities). As a result, simultaneously with reduction of metal ions M^{z+} the protons H^+ from the electrolyte are reduced to hydrogen gas H_2 forming small bubbles near the cathode surface. This process can be formulated with the following Eqs. (4) and (5). Note that both reactions occur at the same time [48], [52].

$$M^{z+}_{(aq)} + ze^- \leftrightarrow M_{(s)} \quad (4)$$

$$2H^+_{(aq)} + 2e^- \leftrightarrow H_2 \uparrow \quad (5)$$

The bubbles continue to grow, as long as they are attached to the surface. Reaching critical size, they detach from the surface which is evidenced by intense hydrogen gas bubbling in the cathode. Since this process if simultaneous with M^+ reduction, the metal deposit will thus form around these bubbles. In this case the bubbles serve as a dynamic template. This process is schematically depicted on Fig. 15.

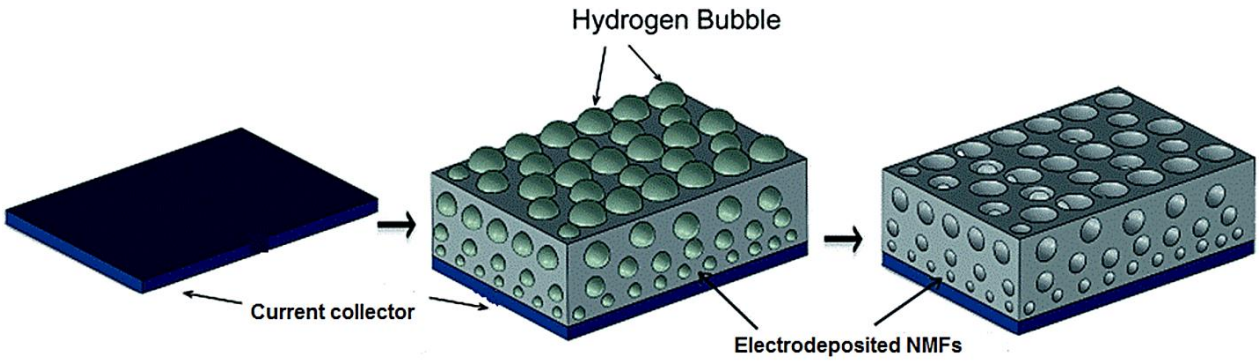

Figure 15. Schematic illustration of electrodeposition of metal using dynamic hydrogen bubble templating (modified from [53])

In the present work the deposition of nanostructured Ni foams over commercial Ni foams using DHBT method was performed by varying both applied time and current density, in order to study the effect of deposition parameters on the morphologies. The details regarding the methodology and obtained results are presented in the Chaps. 6.1 and 8 respectively.

5. C2C-NewCap

C2C-NewCap is a spin off company founded in 2014 by IST researchers that is specialized on the development and production of innovative electric energy storage solutions. On the current stage, the company offers a water-based energy storage device C2C-NewCap assembled in a hybrid configuration, where highly capacitive carbon-based electrode (negative) is paired with a battery type Ni hydroxide electrode (positive) to emulate the exceptional energy density of a battery and supreme power density of a supercapacitor. The final product is a cell of 1.2 V, composed of several pairs of electrodes, immersed in KOH. The electrodes are electrically isolated from each other by a porous membrane (Fig. 8). This cell can be assembled in different shapes and sizes, as well as combined with other cells in modules of 12 V or 24 V, to meet the energy and power densities requirements for varying applications [54].

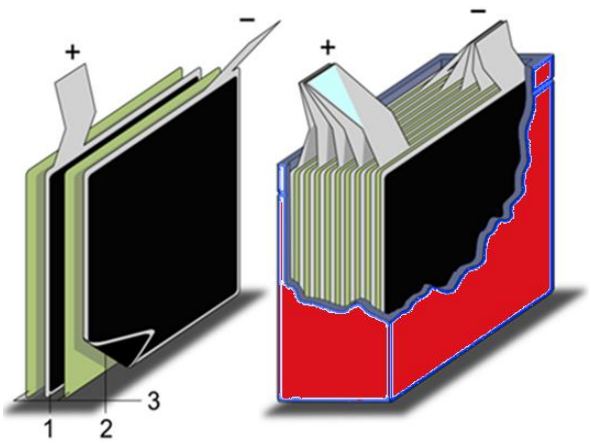

Figure 8. Schematic illustration of hybrid supercapacitor cell design, where (1) positive electrode, (2) negative electrode, (3) Separator, “+”- positive and “-“ negative terminals (modified from [37])

The technology of C2C-NewCap is very reliable. However, there are still open possibilities to improve the production of the Ni-based electrode, particularly in what concerns the number of operations involved in the process and the time of preparation. This of course will reduce cost, saving time and energy. Thus, this dissertation aims at finding alternatives to this process that may lead to time and cost saves.

II. Methodology

This chapter presents methodology of synthesis and characterization of a novel nanostructured electrode for the hybrid energy storage device. The electrode consists of 2 main elements: the electrode support and an electrode active material layer directly grown on a surface of the electrode support. The experimental work is divided in three main parts as shown schematically on the Fig. 16.

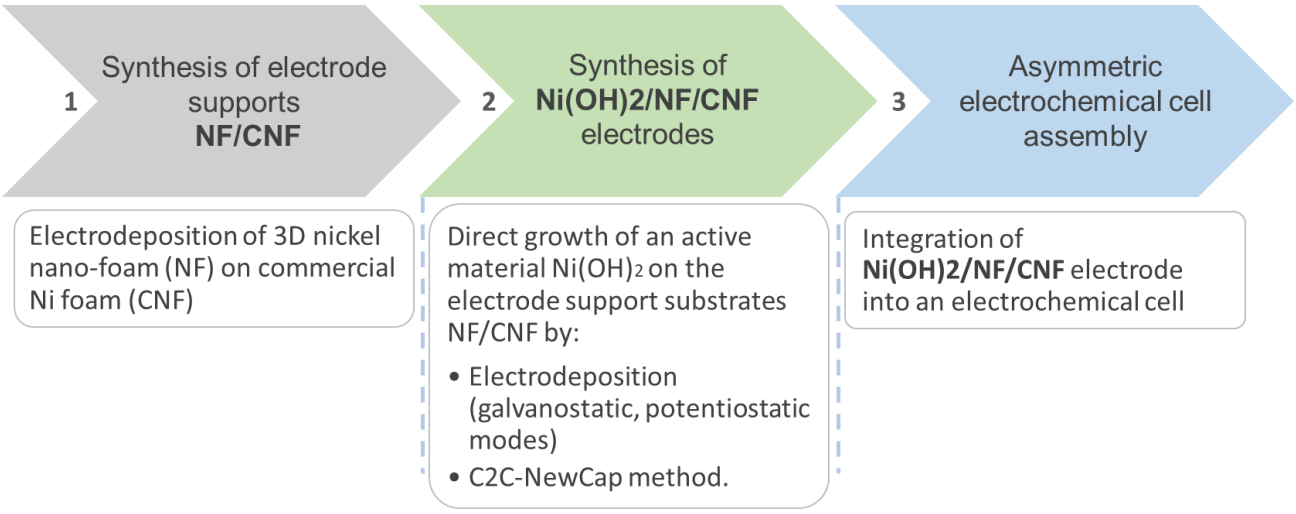

Figure 16. Schematic illustration of the experimental work done in this thesis

The first part of this work is dedicated to fabrication of a nickel composite, which would serve a double function for the novel electrode: current collector and active material support. Here 3D porous nanostructured Ni foams NF were electrodeposited on commercial nickel foam substrates CNF. Ni was selected because of its relatively low cost, good conductivity and good stability in alkaline electrolyte. The effect of the heat treatment on as-prepared foams was examined. As-prepared and heat-treated NF/CNF composites were subjected to morphological and electrochemical characterizations to evaluate their ability to be used as an electrode support for the electrode.

The second part describes the procedure of filling an active material nickel hydroxide into the porous structure of NF/CNF composites to produce a $Ni(OH)_2$/NF/CNF electrode. Two different techniques including electrochemical deposition in both galvanostatic and potentiostatic modes as well as preparation of the electrode in C2C-NewCap company chemical precipitation method were used. Among various electroactive materials, $Ni(OH)_2$ was selected owing to its low cost and high theoretical capacity. As-prepared $Ni(OH)_2$/NF/CNF composites were subjected to full characterization to evaluate their performance as electrode for hybrid supercapacitor.

The final step was to assemble an asymmetric electrochemical cell, where the selected as-prepared $Ni(OH)_2$/NF/CNF composite served as a positive electrode and carbon material (AC) provided by C2C-NewCap as a negative electrode. The cell was subjected to electrochemical characterization. The resulted performance was compared with the asymmetric storage device assembled with sintered electrode (StE) and carbon electrode AC provided by C2C-NewCap.

6. Experimental work

6.1 Synthesis of 3D porous NF/CNF composites

Nanostructured nickel foams (NF) were electrodeposited on commercial nickel foam substrates (CNF) using the dynamic hydrogen bubble template from an electrolyte solution containing 0.1 M $NiCl_2 \times 6H_2O$, 1M NH_4 and 1M NaCl. All chemicals were of analytical grade. Deionized water was used in the synthesis. Properties of CNF are presented in Tab. 2. Prior to electrochemical experiments CNF substrates were cut into pieces of 12×34 mm (+/- 4 cm^2) and chemically cleaned with 0.5 M HCl solution for 30 min to remove the surface oxide layer. Then, the substrates were washed with water and absolute ethanol for 10 min in sequence in an ultrasonic bath [55]. Cleaned substrates (Fig. 17) were dried at 50°C for 24 and then weighted. After electrodeposition, NF/CNF composite was carefully rinsed with deionized water several times and in prior to characterization dried at 60℃ for 48h in the oven.

Table 2. Properties of Commercial nickel foam

Property	Values
Density [g m^{-2}]	480 +/- 30
Porosity [PPI]	90-110
Pores size [µm]	450
Thickness [mm]	1.35

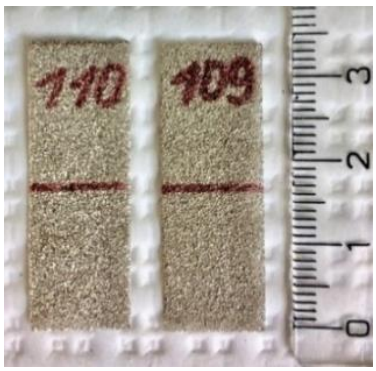

Figure 17. CNF substrates used for electrodeposition

6.1.1 Electrochemical set-up for Ni foam electrodeposition

Electrodeposition of nickel foam over a commercial nickel foam was conducted in galvanostatic mode at room temperature (25°C) in a plexiglass cell (50mL) using a two-electrode system connected to a power source (Sorensen LH110). CNF served as working electrode, two connected graphite plates (30×50×5 mm) were used as counter electrodes. The working electrode was centred between 2 parallel counter electrodes in order to obtain homogeneous deposition of nanostructured foam. The area of soaking into the electrolyte for CNF was kept as 2 cm^{-2}, and for each counter electrode as 10.5 cm^{-2}. The set-up for electrochemical experiments is depicted on Fig. 18.

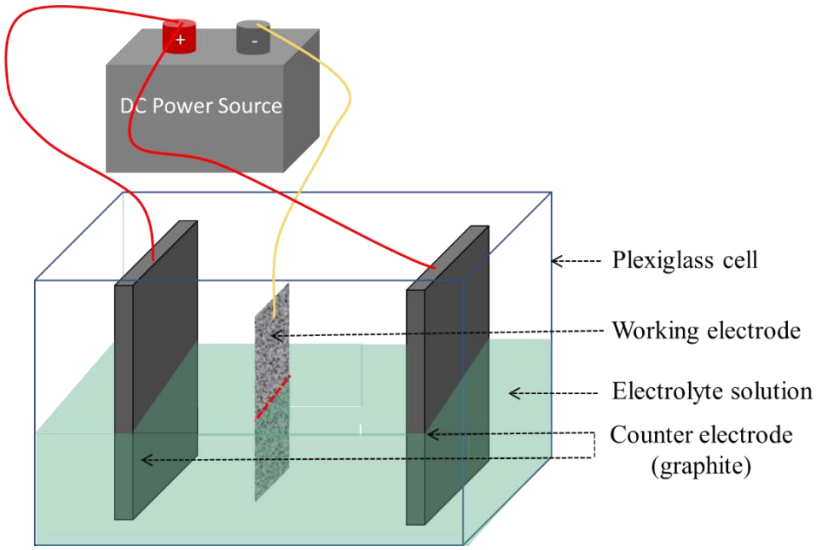

Figure 18. Schematic illustration of electrochemical cell in 2-electrode configuration connected to the DC power source

6.1.2 Electrodeposition parameters

The formation of nickel foam deposits on CNF was controlled by changing the values of applied current and deposition time. The data of NF electrodeposition parameters is presented in Tab. 3.

Table 3. Variation of applied current and time for NF electrodeposition

Current [A]	Current density [A cm^{-2}]	Time [s]
- 1.5	- 0.75	300; 900; 1200; 1800
- 2	- 1	300; 600
- 3	- 1.5	180; 240; 360; 600; 720

6.1.3 Heat treatment

The effect of heat treatment on the electrochemical behavior of deposited materials was studied on the selected samples. The samples were subjected to heat treatment at temperatures of 350°C and 450°C in the oven (model) for 3 hours.

6.2 Electrochemical Synthesis of $Ni(OH)_2$/NF/CNF and $Ni(OH)_2$/CNF composites

6.2.1 Electrochemical synthesis of $Ni(OH)_2$/NF/CNF and $Ni(OH)_2$/CNF composites in galvanostatic mode

Electrodeposition of $Ni(OH)_2$ films was carried out in galvanostatic mode was using the 2-electrode system with the configuration as one depicted on Fig. 18. Here, as a working electrode were used CNF substrate or the as-prepared NF/CNF composite. The electrolyte solutions used for galvanostatic electrodeposition of $Ni(OH)_2$ is presented in Tab. 4.

Table 4. Electrolytes used for galvanostatic electrodeposition

Index	Solution composition
1	0.1 M $Ni(NO_3)_2$
2	0.1 M $Ni(NO_3)_2$+ 0.5 M $NaNO_3$

In order to study the effect of electrodeposition parameters on the mass load and structure of the deposits, experiments were performed varying both applied current and deposition time. The data for electrodeposition parameters is presented in Tab. 5.

Table 5. Variation of applied current and time for $Ni(OH)_2$ galvanostatic electrodeposition

Initial material	Current [A]	Current density [A cm^{-2}]	Deposition time [s]
CNF	- 2	- 1	180
CNF	- 1	- 0.5	300
CNF	- 0.7	- 0.375	900
CNF	- 0.5	- 0.25	600; 900
CNF	- 0.1	- 0.05	600; 900
NF/CNF	- 0.1	- 0.05	240; 360; 420

6.2.2 Electrochemical synthesis of $Ni(OH)_2$/NF/CNF and $Ni(OH)_2$/CNF electrodes in potentiostatic mode

The nickel hydroxide films were obtained by potentiostatic electrodeposition from 0.1 M $Ni(NO_3)_2 \cdot 6H_2O$ aqueous solution. The experiments were performed in three-electrode cells using the Gamry reference 600 potentiostat as a power source. The configuration of the electrochemical set-up was similar as depicted on Fig. 18 and additionally included saturated calomel electrode (SCE, Hanna instruments HI5412) as the reference electrode. Depending on the experiment, working electrode was CNF or the as-prepared NF/CNF supports.

All the active surface films were obtained at a potential of -1.1 V vs. saturated calomel electrode (SCE) during 1200 and 1800 sec. The values used during the experiments are presented in the Tab. 6.

Table 6. Variation of applied voltage and time for $Ni(OH)_2$ potentiostatic electrodeposition

Initial material	Potential [V] vs. SCE	Time [s]
CNF	-1.1	1200; 1800
NF/CNF	-1.1	1200; 1800

6.2.3 Synthesis of $Ni(OH)_2$/NF/CNF electrodes by C2C-NewCap method

Synthesis of the Ni electrode material on the as-prepared NF/CNF support was conducted in the laboratory of C2C-NewCap company. This is a multiple-step method, carried out under the company procedures (not disclosed). This procedure results in chemical precipitation of an active Ni compound onto the porous surface of the immersed substrate. All the details regarding used methodology remained confidential. The selected samples were calendared.

6.3 Assembling of 2-electrode asymmetric electrochemical cell

In the present work to investigate the electrochemical response of as-prepared $Ni(OH)_2$//NF//CNF electrode in asymmetric supercapacitor unit the two-electrode cell was assembled. The as-prepared selected $Ni(OH)_2$/NF/CNF served as a positive electrode, carbon electrode AC from C2C-NewCap company served as a negative electrode. The cell was connected to Gamry reference 600 potentiostat. All measurements were carried out in glass cell (100 mL) using 1 M KOH aqueous solution as the electrolyte at room temperature (25°C).

7. Characterization techniques

This section presents the list of characterization techniques used in the present work.

7.1 Scanning electron microscopy (SEM)

Scanning electron microscopy (SEM) is a tool widely used to characterize and observe the surface of solid material, providing detailed three-dimensional image of samples morphology at various magnifications. The magnification can be adjusted from tens to tens of thousands of times, reaching very high spatial resolution. The SEM technique is based on the physical mechanism of electron optics, electron scattering and secondary electron emission. The images are formed by electronic synthesis, no optical transformation takes place. The main components of SEM are an electron optical column, a vacuum chamber, electronics, and sophisticated software (Fig. 19).

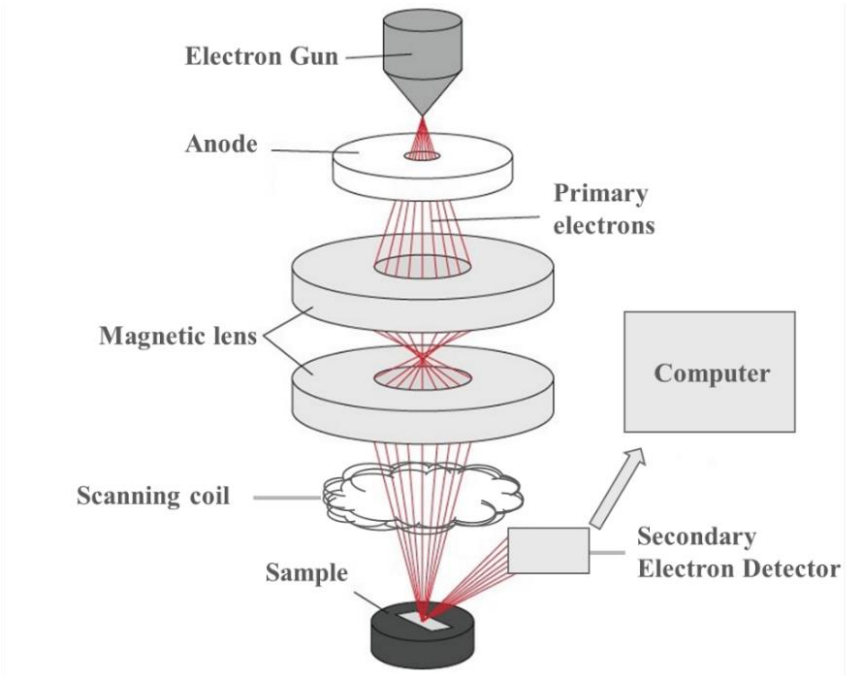

Figure 19. Schematic illustration of the scanning electron microscope (modified from [56])

The electron source at the top of the column generates a high-energy electron beam. This beam is focused into a nano-scale spot volume of the sample and with a help of scanning coils scans across its surface. Each spot on the specimen that is struck by the beam electrons, also referred to as primary electrons, emits signals in the form of electromagnetic radiation. Among those signals, low-energy secondary electrons are the most frequently used to produce images. These electronic signals are attracted and collected by detector, and then

are measured and stored in computer memory. Next the stored values are translated as pixels on a monitor providing a detailed three-dimensional image of the sample structure. The ratio of the size of the displayed image to the size of the area scanned on the sample gives the magnification [57]. The differences in brightness on the image varies with the topography of the examined surface, where the edges are brighter than the hollows.

In the present work, scanning electron micrographs of selected samples were acquired with analytical microscope JEOL 7001-F operated at 15 kV.

7.2 Raman spectroscopy

Raman spectroscopy is an important scattering technique used in chemistry to identify a chemical composition of substances through the detection of vibrational, rotational, and other low-frequency modes in a molecular system. In Raman spectroscopy, the examined sample is irradiated with a powerful laser source of visible or infrared monochromatic radiation, which scatters in all directions after the interaction with sample molecules. Most of the radiation is scattered with a frequency (wavelength) of incident radiation and represents elastic scattered light. However, a small portion of the of scattered radiation differs from the incident (inelastic scattering) due to the change of photon energy upon the interaction with vibrating molecules of the sample. This phenomenon is called Raman scattering and contains the information about the molecular structure of the examined substance [58]. The scattered radiation is measured with a suitable spectrometer with a laser line as a reference, therefore the occurring peaks determined by the vibrating energies associated with molecular bonds in the sample, are measured as a shift from the laser line. The Raman spectrum is expressed in a form of intensity of scattered light versus wavenumber [59].

In the present work, Raman measurements of selected samples were performed at room temperature (22 °C) employing diode laser light at 532 nm from a LabRAM HR Evolution Raman spectrometer (HORIBA, Jobin Yvon, Edison, NJ) with integrated BX41 confocal microscope (Olympus) focused with a 50x objective lens. The Raman spectra of each sample were truncated in the range between 100 and 4000 cm^{-1}.

7.3 Cyclic voltammetry

Cyclic voltammetry is a widely used tool for acquiring qualitative information about the electrochemical species and mechanism in an electrochemically active material. This technique is based on a linear potential sweep varying the applied potential at a working electrode between potential limits, E1 and E2, at a certain scan rate, while monitoring the generated current. A scan rate is defined as a change in potential versus time. When the voltage reaches E2, the scan is reversed and runs in the opposite direction back to E1. The resulting measurements of the current plotted versus potential is called a cyclic voltammogram [60].

An experimental apparatus for cyclic voltammetry in a modern electroanalytical system consists of a potentiostat, computer, and the electrochemical cell. A typical electrochemical cell includes three electrodes (working, counter and reference) inserted into an ionic electrolyte. The current flows through the electrolyte between the working and counter electrodes. The electrode potential of interest E is that between working and the reference electrode. The instrument which controls the potential, E, is the potentiostat [61]. Using computer software, the resulting current-potential measurement can be displayed as a plot on the computer monitor. The cyclic voltammogram profile varies depending on the nature of material and its reactivity in the tested environment (double layer, charge transfer).

Redox active materials

For the faradaic nature material as the potential is swept back and forth, the pass through the standard potential E_0 of a species forces a change in the concentration C of an electroactive species at the electrode surface by electrochemically reducing (Red) or oxidizing (Ox) it. The reduction or oxidation of a substance results in the generation of currents.

For the reversible faradaic reactions, the system remains in equilibrium throughout the potential scan. In other words, the surface concentrations of Ox and Red are maintained at the values required by the Nernst equation presented below:

$$\mathrm{E} = \mathrm{E}_0 + \frac{\mathrm{RT}}{\mathrm{nF}} \ln \frac{\mathrm{C(Ox)}}{\mathrm{C(Red)}} \tag{6}$$

where, *E* is the applied potential difference and E_0 is the standard electrode potential, *n* is no. of electrons transferred, *R* is the molar gas constant (8.3144 [J mol^{-1} K^{-1}]), *T* is the absolute temperature [K], *F* = Faraday constant [96 485 C mol^{-1}] [62].

The typical cyclic voltammetry response for an electrochemical reaction is depicted in Fig. 20. The scan is presented clockwise, i.e when a positive potential is applied, the electroactive species lose an electron at the electrode giving rise to an anodic current *Ipa*, which appears on the plot as an oxidation peak at a given potential *Epa*. Cathodic current *Ipc* occurs when the potential is applied in the negative direction leading to a reduction process and is defined as cathodic current *Ipc* peak at a given potential *Epc*.

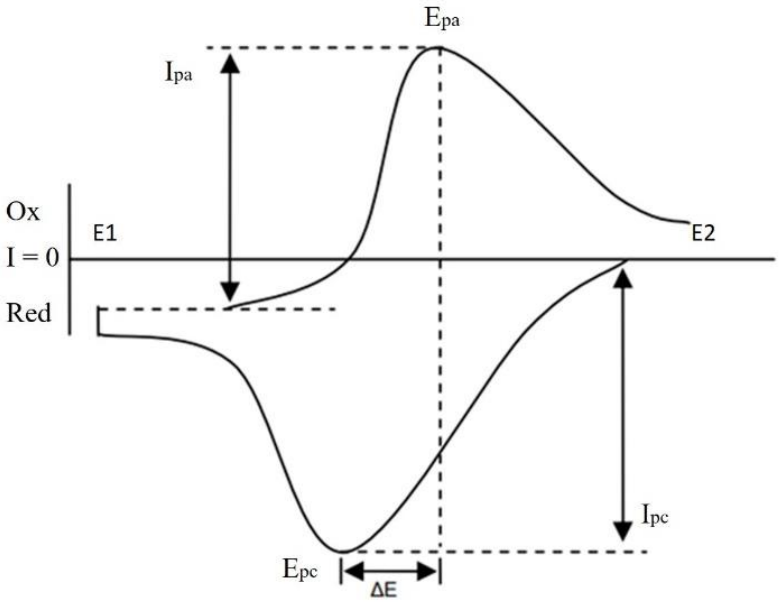

Figure 20. Schematic illustrations of CVs of rechargeable battery (adapted from [63])

For a reversible system, the cyclic voltammogram exhibits cretain well defined characteristics [64]:

I. The peak height of the anodic Ipa and cathodic Ipc waves should be equivalent.

$$I_{pa} \approx I_{pc} \tag{7}$$

II. The voltage separation ΔE between the current peaks is defined by the following Eq.2, where n is the number of electrons transferred:

$$\Delta E = E_{pa} - E_{pc} \approx 0.059/n \tag{8}$$

III. When the scan rate is altered the current response also changes, both the cathodic and anodic currents are expected to be increased in proportion to the square root of the scan rate magnitude. In case of the reversible redox couple, the function (for either the anodic or cathodic waves) is expected to be invariant with scan rate, kepping the intercepts at the origin as depicted on the Fig. 21.

The current peak-to-peak distance is not dependent only on the charge-transfer mechanism; The higher system resistances, the larger is the current peaks voltage separation ΔE. It is also important to emphasize that the impact of system resistance on potential is scan-rate-dependent since the magnitude of the observed current increases with scan rate. Therefore, in case of high system resistance, a reversible couple may demonstrate a scan-rate-dependent peak-to-peak potential variation [65]. Thus, to assure the accuracy of material characterization cyclic voltammerty experiments should be performed over different scan rates.

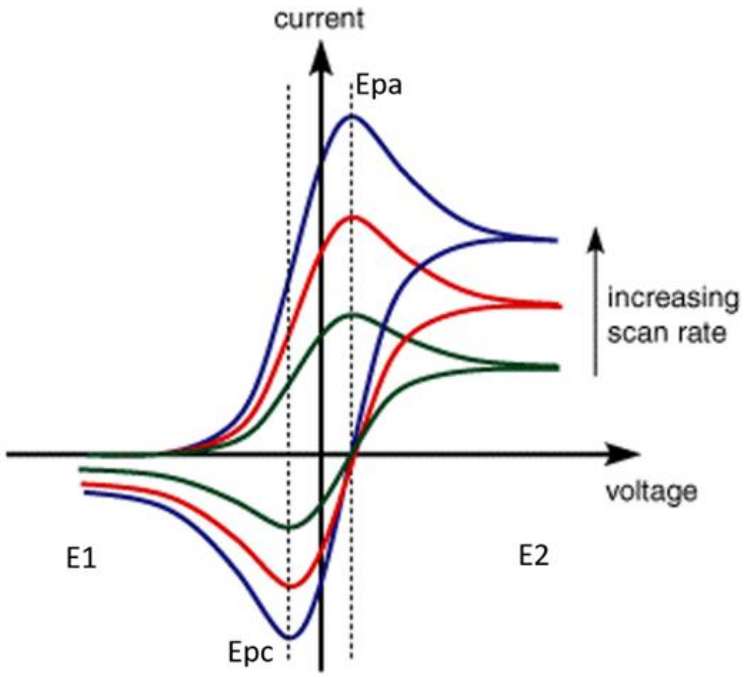

Figure 21. The influence of scan rate for a reversible electron transfer reaction (adapted from [63])

EDLC materials

Ideally, capacitive material demonstrates a rectangular cycle voltammogram profile, where current flowing through the system is proportional to the linear variation of voltage scan rate, but independent of voltage itself. This response arises from the fundamental nature of the EDLC storage mechanism [15]. In the absence of diffusion limitations, when the external electric field is applied the charge separation occurs immediately, therefore dV/dt is a constant.

Depending on the direction of the voltage scan, the current can also be positive or negative. Principally, if the voltage scan is reversed in direction but retains the same rate, the current jumps from a positive value to a negative value. This gives the rectangular CV shapes at various scan rates as shown in Fig. 22. In fact, the rectangular shape of the CV plot is an experimental criterion for qualitatively judging of capacitive performance of a device or electrode [66].

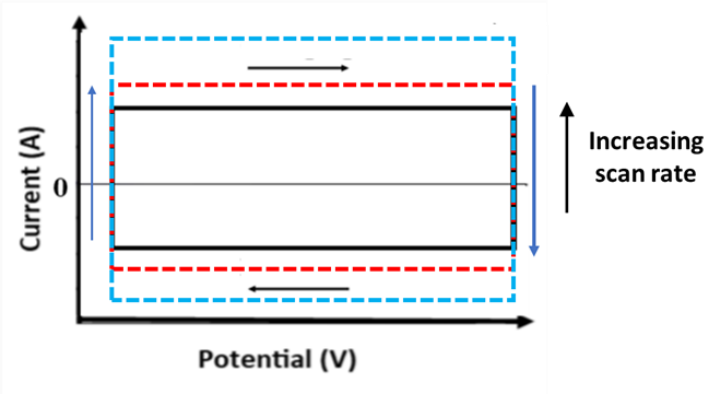

Figure 22. Schematic illustrations of CV of ideal EDLC material at different scan rates (taken from [15])

In the present work all electrochemical measurements were carried out in glass cell (100 mL) using 1 M KOH aqueous solution as the electrolyte at room temperature (25°C). Electroanalytical tests for single electrodes were conducted in a three-electrode cell connected to Gamry reference 600 potentiostat. The schematic illustration of the electrochemical set-up is depicted on the Fig. 23, where the different samples to be studied were used as the working electrode, a platinum wire as the counter electrode, saturated calomel electrode (SCE) as the reference electrode. The potentiostat applied and maintained potential between the working and reference electrode while at the same time measured the current at the working electrode.

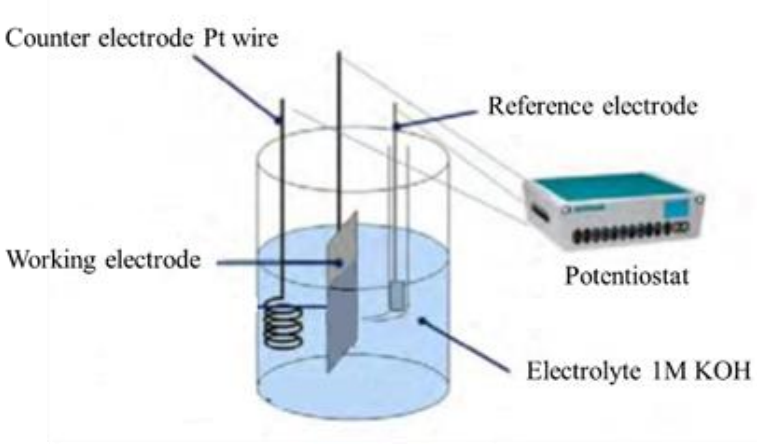

Figure 23. Schematic illustration of set-up for electrochemical experiments (modified from [67])

Testing single electrode, cyclic voltammetry was conducted in a potential range between -0.2 and 0.8 V vs. SCE at various scan rates of 2, 5, 10, 20 mV s^{-1}. For the 2-electrode asymmetric electrochemical cell with configuration described in the section 3, the tests were carried out in a potential range between 0 and 2 V vs. SCE at various scan rates of 2, 5, 10, 20, 30, 50 and 100 mV s^{-1}. The recorded values were used to plot the graph of current versus the applied potential.

7.4 Chronopotentiometry

Chronopotentiometry (or galvanostatic charge-discharge) is a standard technique used to characterize the performance and the cycling stability of electrode materials under controlled current conditions. In this technique, a constant current is applied to the working electrode and its resulting potential is measured against a reference electrode as a function of time. This process is carried out until the electrode potential reaches the cut-off voltage. The resulting measurements of the potential plotted versus time is called a capacity curve. In case of ideal battery type material, the galvanostatic charge-discharge (GCD) profile displays plateaus (Fig. 24a), and EDLCs materials exhibit linear potential-time profile (Fig. 24b).

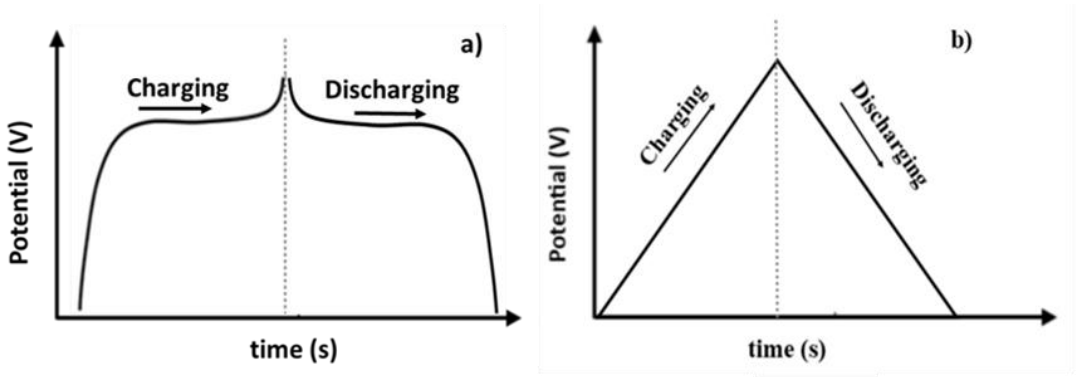

Figure 24. Schematic illustration of GCD profile of a) an ideal battery and b) ideal EDLC electrode (taken from [15])

In the present work, the specific capacity C of the active material was estimated from discharge curves of single electrodes, using the following equation:

$$C = I \times \frac{t_{discharge}}{3600 \times m} \ [mAhg^{-1}] \quad (9)$$

Where *I* is the applied current [mA], $t_{discharge}$ is the discharge time [sec], and *m* is the mass of an active material [g].

To evaluate the rate capability of a single electrode, the specific capacity was measured at different discharge currents. The cycling stability test of selected electrodes was conducted by applying current density of 25 mA cm^{-2} for 1000 cycles.

For the 2-electrode asymmetric system the specific capacitance Cs, real energy Ereal and real power density Preal were determined from galvanostatic charge–discharge measurements using the following equations:

$$C_s = I \times \frac{t_{discharge}}{\Delta V_{disch} \times m_2} \ [F\ g^{-1}] \quad (10)$$

$$P_{real} = I \times \frac{\Delta V_{disch}}{m_2} \times 1000 \ [W\ kg^{-1}] \quad (11)$$

$$E_{real} = \frac{P_{real}\ t_{disch}}{3600} \ [Wh\ kg^{-1}] \quad (12)$$

where *I* [A] is the applied constant current, $t_{discharge}$ [sec] is the discharge time, ΔV_{disch} [V] is the potential difference between the end of the charge and the end of the discharge and m_2 [g] is the sum of the active mass of both electrodes [68].

Ideally, the potential difference throughout charge-discharge half-cycles remains constant, i.e. the efficiency of the charge transfer is 100%. Though in practice, the charge potential is higher than the discharge potential due to electrode polarisation and ohmic internal resitance (IR-potential drop) arising during GCD half-cycles (Fig. 25) and therefore the charge and discharge time are not equivalent [28].

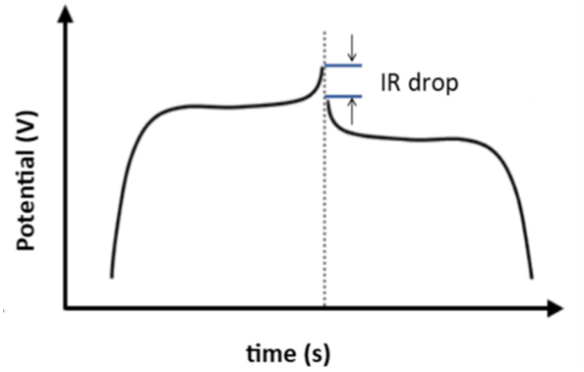

Figure 25. Schematic illustration of the difference in potentials between the end of charge and begginning of discharge [28]

In the present work the charge-discharge efficiency rate CR was calculated with using a following equestion:

$$CR = \frac{t_{discharge}}{t_{charge}} \times 100\% \quad (13)$$

where t_{charge} and $t_{discharge}$ [sec] are the values of charge and discharge time at certain constant current at the fixed potential window.

All chronopotentiometry experiments were carried out in 1 M KOH electrolyte at room temperature. The electrochemical tests for the single electrode were performed in set-up as described in the section for cyclic voltammetry (Fig. 23). The 2-electrode system was tested in configuration as described in Chapter 6.1.1. The electrochemical stability windows of each electrode and of the full cells were evaluated by cyclic voltammetry. Depending on the system under investigation, the constant current charge–discharge tests were carried out at various current densities of 7.5, 10, 50, and 25 mA cm^{-2} within a potential range of 0 to 0.42 V for testing single electrode, and of 0 to 2 V for the 2-electrode electrochemical cell.

III. Results and discussion

8. NF/CNF composites for electrode supports.

Fabrication of electroactive NF/CNF composites was performed by electrodeposition of nickel nanofoam (NF) from an electrolyte solution containing 0.1 M $NiCl_2 \times 6H_2O$, 1M NH_4 and 1M NaCl over a commercial microporous Ni foam (CNF). During the deposition process of the 3D Ni structures the following electrochemical reactions and a precipitation reaction may occur [69].

$$Ni^{2+} + nNH_3 \leftrightarrow Ni(NH_3)_n^{2+} \quad , 2 \leq n \leq 6 \tag{14}$$

$$Ni(NH_3)n^{2+} + 2\ e^- \rightarrow Ni(s) + nNH_3 \tag{15}$$

$$NH_4^+ + e^- \rightarrow NH_3 + H_{ads} \tag{16}$$

$$2H_{ads} \rightarrow H_2(gas)\uparrow \tag{17}$$

Firstly, nickel ions form complex compounds in solution (Eq. 14) that are reduced (Eq. 15) at the surface of the working electrode, in this case a commercial nickel foam. Due to the high current applied, electrodeposition of Ni occurred simultaneously with hydrogen bubble evolution. Ammonium ions are reduced at the Ni foam surface and hydrogen gas is evolved (Eq. 16 and 17), creating pores through the bulk of deposited Ni. In the present work electrodeposition experiments resulted in formation of grey foam-like metallic Ni well-adherent to the CNF substrate (Fig. 26).

Figure 26. Image of the typical NF/CNF composite resulted from electrodeposition experiments

8.1 Optimization of electrodeposition parameters for Ni foam synthesis: applied current and deposition time.

Series of samples were produced by changing the values of deposition time and applied constant current densities. These parameters showed significant influence on mass load of deposited nickel nanofoam. The electrodeposition parameters and the obtained results are listed in the Tab. 7.

Table 7. Results from experiments of electrodeposition of Ni nanofoam over a commercial nickel foam CNF

	Current [A]	Current density [A cm^{-2}]	Time [s]	Deposited mass [mg cm^{-2}]	Index	Observations
1.	- 1.5	- 0.75	300	10	NF_1.5_10	Insufficient - thin layer.
2.	- 1.5	- 0.75	900	30	NF_1.5_30	
3.	- 1.5	- 0.75	1200	80	NF_1.5_80	Homogeneous distribution.
4.	- 1.5	- 0.75	1800	95	NF_1.5_95	
5.	- 2	- 1	600	30	NF_2_30	Insufficient - thin layer.
6.	- 2	- 1	300	20	NF_2_20	
7.	- 3	- 1.5	180	30	NF_3_30	
8.	- 3	- 1.5	360	60	NF_3_60	Homogeneous distribution.
9.	- 3	- 1.5	600	80	NF_3_80	
10.	- 3	- 1.5	720	95	NF_3_95	Excess of Ni deposit

Deposits resulting in mass load lower than 60 mg cm^{-2} (sample 1; 2; 5; 6; 7) showed low coverage of the CNF substrates and appeared not adequate to be used as electrode supports. The deposits with mass load of 95 mg cm^{-2} (sample 4, 10) demonstrated uneven distribution on the substrate with agglomeration of nickel particles at the edges, which detached after drying. Therefore, these samples were rejected and not used for future characterization. The deposits 3, 8 and 9 were homogeneously distributed on the substrate and resulted in significant increase of the surface density of CNFs. The samples with deposit mass of 60 mg cm^{-2} and 80 mg cm^{-2} were selected for further testing and characterization.

8.2 Dependency of deposited mass on current density and deposition time.

The experimental results indicate that the value of applied current plays a significant role in the electrodeposition process in this study. The electrodeposition time is also a factor that influences the mass of

deposited foams. As expected, the mass load of Ni nanofoam increases with the deposition time and the value of applied current. In order to demonstrate increasing trend, this dependency is shown in Fig. 27.

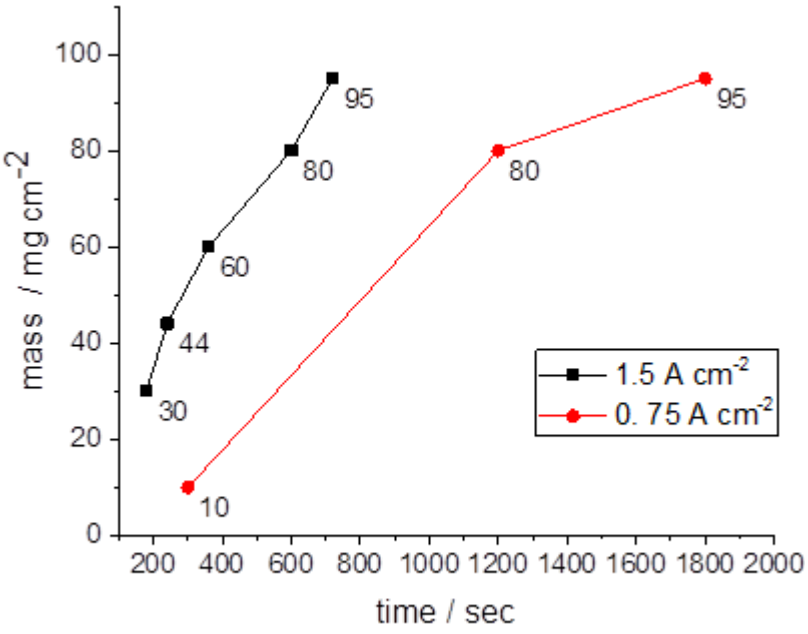

Figure 27. Dependency between deposited mass and applied current density

It was observed, that at higher currents less time was required to obtain desired amount of deposit. For the cost efficiency of the experiments, further depositions of 60 mg cm^{-2} and 80 mg cm^{-2} were produced at the maximum current density of -1.5 A cm^{-2} and were referred as NF_60/CNF and NF_80/CNF, respectively.

8.3 Morphological characterization of electrodeposited Ni nanofoam

The surface morphologies of the CNF and as-deposited NF_80/CNF composites were studied by FEG-SEM. The SEM images taken at different magnifications are shown in Fig. 28. For comparative purposes, the sintered nickel S/CNF which is used as an electrode support provided by C2C-NewCap electrode is also depicted.

The commercial Ni foam shown on the Fig. 28a demonstrates an open 3D morphology with randomly distributed large pores. The typical morphology of Ni nanofoams, with mass of 80 mg cm^{-2}, electrodeposited on the CNF at -1.5 A cm^{-2} and 600 s is shown in Fig. 28c. In agreement with literature [70], this Ni nanofoam deposit demonstrates a uniform sponge-like morphology where the pores result from hydrogen bubble evolution during the electrodeposition process. It is clearly observed (Fig. 28b) that the deposit of the Ni nanofoam leads to reduction of the pore size compared to the CNF surface.

Higher magnification images (Fig. 28d) demonstrate that the Ni nanofoam deposits is composed of small agglomerates of Ni grains. Therefore, the porosity of the NF/CNF composites arises not only from the original CNF large pores, rough morphological features of the pore walls of deposited Ni. The formation of an open 3D network with an increased density of smaller pores over the commercial foam is expected to create a very suitable network for a high storage of the active material and facilitate the access of the electrolyte ions to the available electrochemical sites.

The sample S/CNF obtained by the sintering method in C2C-NewCap laboratory is presented on the Fig. 28e. Higher magnification image (Fig. 28f) shows that sintered Ni particles are formed of agglomerates of randomly shaped Ni grains. One can observe, that in comparison to CNF, the sintered sample has a surface area with significantly smaller average pore size.

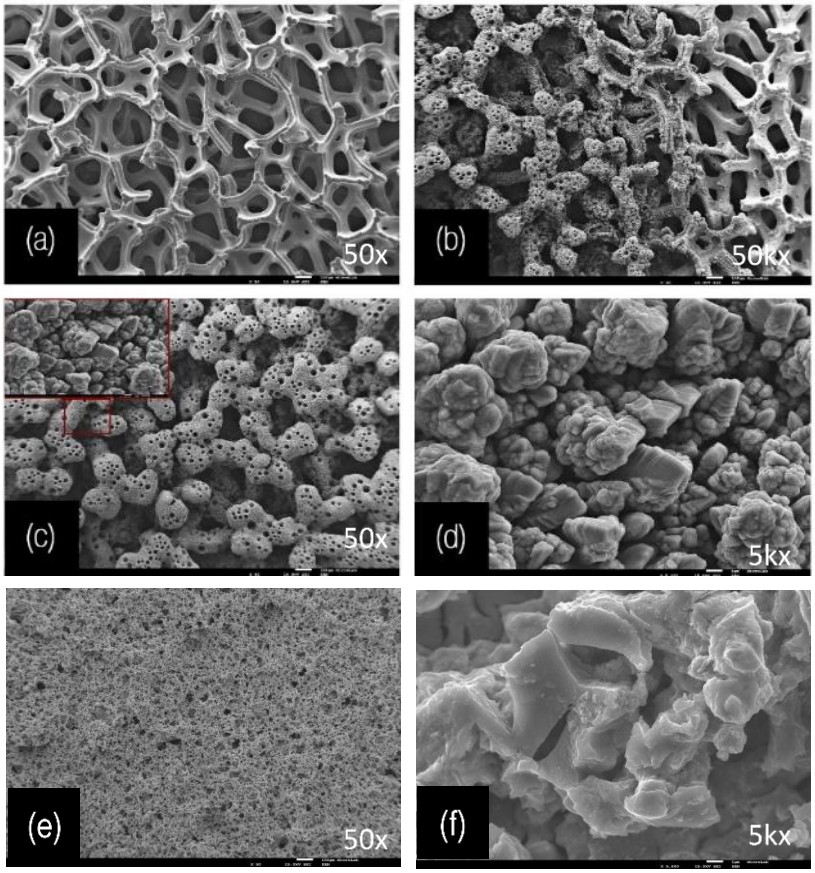

Figure 28. Comparison of morphologies of (a) CNF at magnification 50X (b) NF_80/CNF on the edge with clean CNF at magnification 50X (c) NF_80/CNF at magnification 50X (d) Sample NF_80/CNF at magnification 5kX (e) Sintered nickel S/CNF at magnification 50X (f) Sintered nickel S/CNF at magnification 5kX

8.4 Electrochemical characterization

In this chapter in order to investigate the electrochemical properties of NF/CNF composites, cyclic voltammetry and GCD experiments were performed. The obtained results were used to evaluate if NF/CNF composites were suitable to be used as an electrode supports.

8.4.1 Cyclic voltammetry results

The cyclic voltammograms were measured with a 3-electrode cell in 1M KOH electrolyte at rate of 5 mV s^{-1} in a potential window from 0 V to 0.55 V. The results of the electrochemical performance of NF_60/CNF and NF_80/CNF are presented on Fig. 29. The CV curves of the sintered nickel S/CNF and clean commercial foam CNF obtained in the same conditions are also depicted.

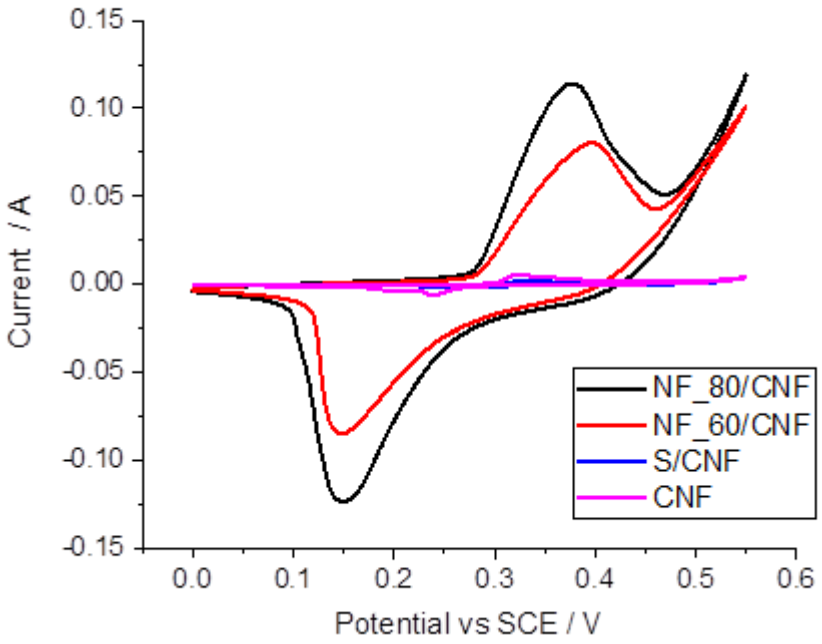

Figure 29. Comparison of the electrochemical response of the different materials at scan rate of 5 mV s^{-1}

All voltammograms revealed one pair of redox peaks. During the scan the following chemical reactions are expected to occur [71]:

$$Ni + 2OH^- \rightarrow Ni(OH)_2 + 2e^- \quad (18)$$

$$Ni(OH)_2 + OH^- \leftrightarrow NiOOH + H_2O + e^- \quad (19)$$

Eq. 18 corresponds to the formation of $Ni(OH)_2$ at the surface of the metal Ni nanofoam in alkaline electrolytes; however, this reaction is irreversible. Therefore, the peaks in the CV curves are mainly related to the Faradaic reaction of $Ni(OH)_2$ (Eq.19), which is reversible. Here, the anodic peak was referred to the oxidation of $Ni(OH)_2$ into NiOOH and the cathodic peak corresponds to the reverse process. The current peak from 0.55 V is due to oxygen evolution [72]. The corresponding reaction is the discharge process of OH^-.

$$4OH^- - 4e^- \rightarrow O_2(gas)\uparrow + 2H_2O \quad (20)$$

The chemical reaction in Eq. 19 is also the half-cell electrochemical reaction at the positive electrode during charge-discharge process of $Ni(OH)_2$ when used as electrode for charge storage. The voltammograms in Fig. 30 show that the best performance in terms of current response was observed from the NF_80/CNF composite. For this reason, NF_80/CNF composite was selected as an electrode support for all further experiments in the present work. However, the observed current is still very small (inferior to 0.5 mA at scan rate of 5 mVs^{-1}), which indicates a very little electrochemical activity of NF_80/CNF. Therefore, using NF_80/CNF as a support for electrode, is not expected to give sufficient contribution to the overall electrode capacity.

Cyclic voltammograms of NF_80/CNF taken at different scan rates are presented on the Fig. 30.

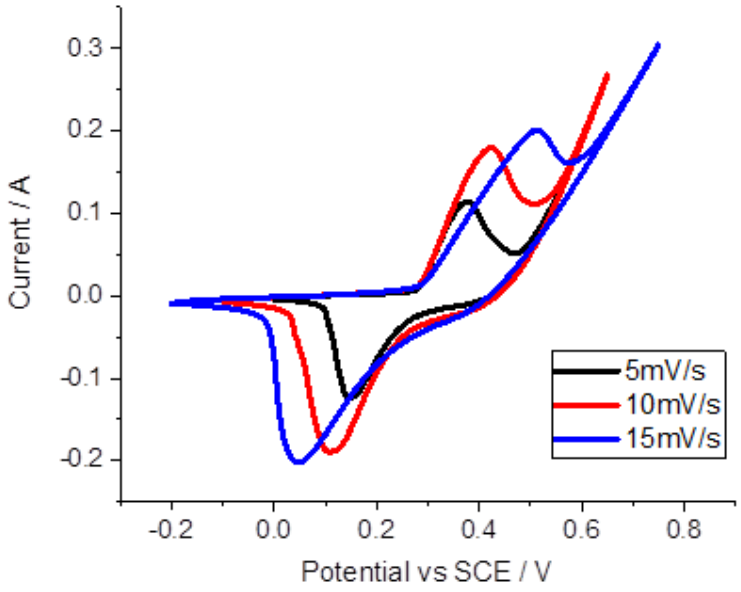

Figure 30. Comparison of performances of NF_80/CNF at different scan rates

The redox peaks are observed at different sweep rates and the shapes of these curves are similar, meaning that the electrochemical behaviour of the material is maintained over this range. As expected, the intensity of the current peaks increased as the sweep rate increased. The quasi-reversibility of the system may be assumed from the fact, that the intensity of the anodic and cathodic waves remains equivalent. However, the voltage separation between the current peaks is also scan-rate dependent: the higher scan rate, the larger the separation between the redox peaks, indicating the quasi-reversibility of the electrode.

Results of the Heat treatment

The CV curves of NF_80/CNF before and after thermal treatment at 350ºC (NF_80/CNF_350C) and 450ºC (NF_80/CNF_450C) are shown on Fig. 31. It is clearly observed that, the current intensity of heat-treated samples is much weaker compared to the as-prepared Ni deposits. As explained in literature [73], during the heat treatment residual oxygen reacts with the metallic nickel foam to form a thinner films of nickel oxide that may display semiconducting behaviour, resulting in lower electrochemical activity compared with untreated sample. As can be seen in Fig.31, with increase of the heat treatment temperature, from 350º C to 450ºC, the electrochemical response is poorer, meaning that there are more semiconducting nickel oxides being formed on the surface of the foam. For these reasons in the present work the heat treatment was not included considered in the further experiments.

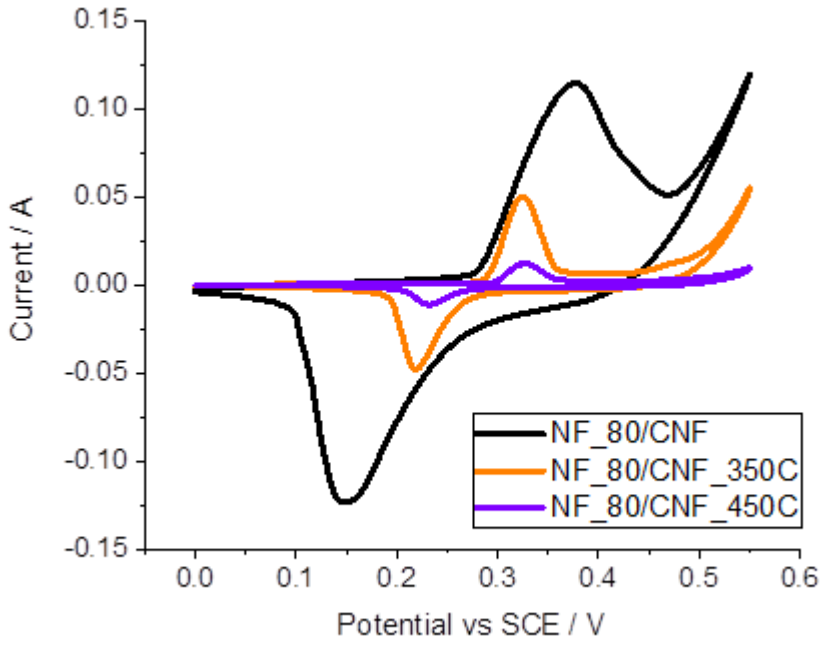

Figure 31. Comparison of performances of NF_80/CNF before and after the heat treatment at the scan rate of 5 mV s^{-1}

8.4.2 Charge-discharge curves

Knowing the working potential window, the electrochemical performance of CNF, sintered nickel S/CNF and as-prepared NF/CNF with mass load of Ni of 60 and 80 mg cm^{-2}, was also investigated by chronopotentiometry tests. The discharge curves of the tested samples were obtained by applying a constant current density of -7.5 mA cm^{-2} (Fig. 32). As can be seen the electrodeposited nickel nanofoams exhibit a plateau-like shape and demonstrate significantly longer discharge time compared to both sintered nickel and CNF. This behaviour was very marked for the NF_80/CNF electrode.

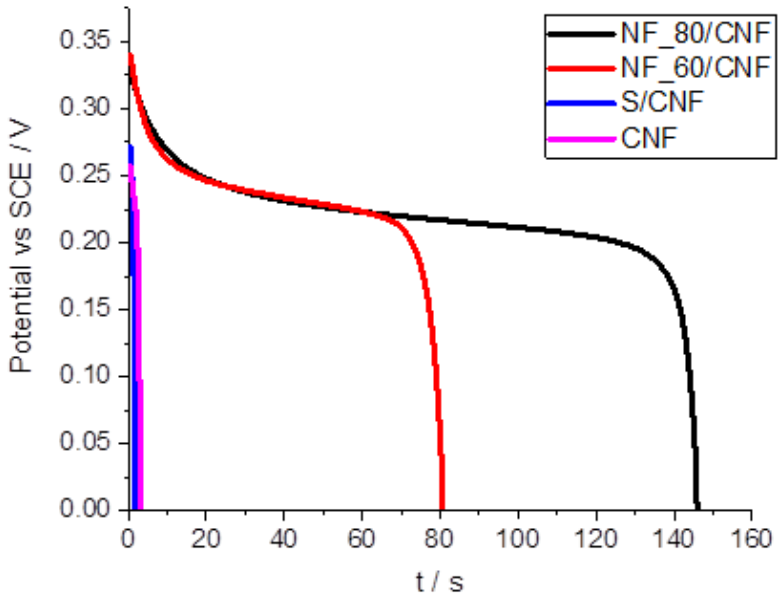

Figure 32. Comparison of the discharge curves of different samples at -7.5 mA cm^{-2}

The specific capacity for the composites was calculated from these discharge curves using formula (9) described in methodology. The results are presented in Tab. 8. Composites NF_80/CNF and NF_60/CNF exhibit the highest specific capacity values and were used as electrode supports for the further experiments in the present work.

Table 8. Specific capacity calculated from GDC at current density of -7.5 mA cm^{-2}

Sample	Specific capacity [mAh g^{-1}]
NF_80/CNF	8
NF_60/CNF	4
S/CNF	0.125
CNF	0.125

9. Experimental results obtained from synthesis of $Ni(OH)_2$/NF/CNF and $Ni(OH)_2$/CNF composites

9.1 Synthesis of $Ni(OH)_2$/NF/CNF and $Ni(OH)_2$/CNF composites in galvanostatic electrodeposition mode

In order to select the most appropriate electrolyte for the synthesis of $Ni(OH)_2$, preliminary electrodeposition experiments were performed in two electrolyte solutions. The results are presented in Tab.9.

Table 9. Results from electrodeposition experiments using different electrolyte solutions

	Solution composition	Observations
1.	0.1 M $Ni(NO_3)_2$+0.5M $NaNO_3$	Deposit occurs in low extent.
2.	0.1 M $Ni(NO_3)_2$	Deposit ocurres in sufficient content.

As described in Tab.10, the deposits obtained by galvanostatic electrodeposition from the electrolyte solution 0.1 M $Ni(NO_3)_2$+0.5M occurred in a very small amount, not equally distributed on the substrate. The parameters used for electrodeposition from the solution 1 are listed in Tab. 10. A commercial nickel foam CNF was used as a substrate in this set of experiments. The results show that the formation of deposits did not occur at current densities of -1.5 A cm^{-2} and -0.75 A cm^{-2}. Reducing the applied current density to 0.05 Acm^{-2} resulted in deposition of unstable light-green deposits (Fig. 33) that were not well-adherent to the surface of the CNF substrate.

Table 10. Results from galvanostatic electrodeposition experiments using solution 1

Sample	Initial material	Index	Current density [A cm^{-2}]	Time [s]	Observations
1.	CNF	CNF_31	- 1.5	360	Deposition does not occur
2.	CNF	CNF_44	- 0.75	600	
3.	CNF	CNF_45	- 0.05	900	Deposition occurs in a reduced extent
4.	CNF	CNF_46	- 0.05	600	

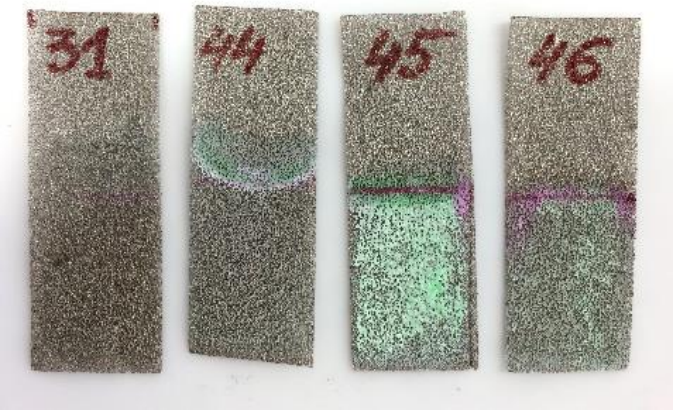

Figure 33. Samples obtained from electrolyte no.1

In the set of experiments from electrolyte 2 electrodeposition resulted in bright-green deposits (Fig. 34), the formation of which can be explained by electrochemical (Eq. 21) and precipitation reactions (Eq. 22, 23) expressed as follow [74]:

$$2H_2O + 2e^- \rightarrow H_2 + 2OH^- \quad (21)$$

$$Ni^{2+}_{(aq)} + +2OH^-_{(aq)} + yH_2O \rightarrow [Ni(OH)_2\ yH_2O] \downarrow \quad (22)$$

$$Ni^{2+}_{(aq)} + +2OH^-_{(aq)} + NO_3^- + yH_2O \rightarrow \left[Ni(OH)_{(2-x)}(NO_3)_x yH_2O\right] \downarrow \quad (23)$$

where *x* and *y* are the concentrations of nitrate ions and water molecules presented in the hydroxide compound, respectively.

Firstly, when electric current passes, water molecules are reduced on the surface of the working electrode, generating OH^- ions and H_2 gas (Eq. 21). During this reaction the evolution of the gas bubbles near the cathodic surface could be experimentally observed. This step results in an increase of the local pH, establishing the conditions for formation of $Ni(OH)_2$ deposit [75]. Next, nitrate ions presented in the electrolyte solution can be reduced by consuming generated OH^- ions (Eq. 22, 23). This step leads to the formation of a Ni hydroxide film on the surface of the working electrode.

Tab.11 depicts an overview of the galvanostatic electrodeposition experiments performed by varying applied current and deposition time. CNF, NF_60/CNF and NF_80/CNF were used as substrates for the functionalization with $Ni(OH)_2$. As expected, the mass load of the deposits shows strong dependency on the deposition time and on the value of applied current. All samples with a mass load higher than 16 mg cm^{-2} (sample 1; 2; 3; 4; 5; 7; 8; 9; 10) showed inconsistent distribution of deposited material with accumulated particles on the edges of the surface of substrates. After drying the agglomerated particles detached from the substrate. These structures appeared unstable and were rejected for further experiments. The deposits

formed on samples 6, 11 and 12 were homogeneous and adhered well to the substrates: unlike other samples, after rinsing the sample 6, 11 and 12 with water several times and drying in the oven for few hours, no material detachment was observed. Taking these results into consideration, these samples were chosen for subsequent studies.

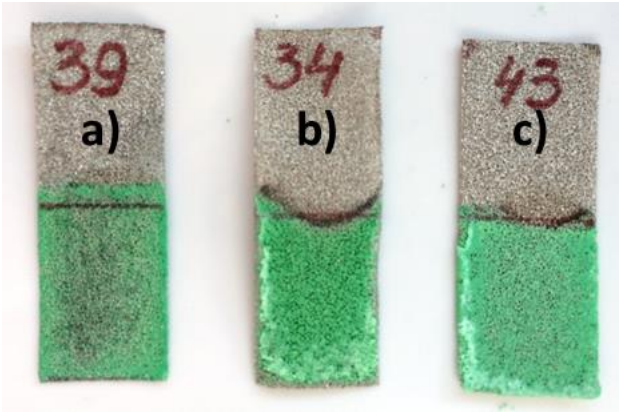

Figure 34. deposits obtained on CNF substrate from solution #2: a) sample 6 - CNF_g18, b) sample 3 - CNF_g45, c) sample 4- CNF_g50

Table 11. Results from galvanostatic electrodeposition experiments using solution 2

Sample	Initial material	Index of $Ni(OH)_2$	Current density [A cm^{-2}]	Time [s]	Mass [mg cm^{-2}]	Observations
1.	CNF	g60	- 1	180	60	Bulky deposit with agglomerations on the edges of the substrate; material detachment from the substrate after drying
2.	CNF	g60	- 0.5	300	60	
3.	CNF	g45	- 0.25	600	45	
4.	CNF	g50	- 0.25	900	50	
5.	CNF	g55	- 0.35	900	55	
6.	CNF	g18	- 0.05	600	18	Homogeneous green deposit well adherent to the substrate
7.	CNF	g30	- 0.05	900	30	Deposit with little access of material on the edges, which was detached from the substrate after drying.
8.	NF_80/CNF	g25	- 0.05	420	25	
9.	NF_80/CNF	g20	- 0.05	360	20	
10.	NF_60/CNF	g25	- 0.05	420	25	
11.	NF_80/CNF	g16	- 0.05	240	16	Homogeneous green deposit, no visible material detachment after drying.
12.	NF_60/CNF	g18	- 0.05	360	18	

9.2 Synthesis of $Ni(OH)_2$/NF/CNF and $Ni(OH)_2$/CNF nanocomposites in potentiostatic electrodeposition mode

The results obtained by potentiostatic electrodeposition from solution 2 are presented below (Tab. 12). As described, the deposit of 12 mg cm^{-2} (sample 1) showed low material content and was rejected for further studies. Similarly to galvanostatic experiments, sample 3 with mass load of 37 mg cm^{-2} showed nickel aggregates at the edges of the substrate. This sample was considered unstable due to material detachment after drying. At last, the deposits with mass load of 16 mg cm^{-2} (sample 2) and 17 mg cm^{-2} (sample 3) showed uniform distribution of thin film throughout the substrate, and therefore were selected for further characterization.

Table 12. Results from potentiostatic electrodeposition experiments using solution 2

Sample	Initial material	Index of $Ni(OH)_2$	Potential [V] vs. SCE	Time [s]	Mass [mg cm^{-2}]	Observations
1.	NF_80/CNF	pot12	-1.1	1200	12	Homogeneous thin layer of deposit, low content.
2.	NF_80/CNF	pot16	-1.1	1800	16	Homogeneous distribution, sufficient coverage of the substrate.
3.	CNF	pot17	-1.1	1200	17	
4.	CNF	pot37	-1.1	2400	37	Bulky deposit, agglomeration on the edges of the substrate, material detachment after drying.

9.3 Characterization

9.3.1 Morphological characterization of deposits

To study the effect of the electrodeposition modes (potentiostatic or galvanostatic) on the surface morphology, selected composites were analysed by SEM. As-prepared Ni hydroxide films obtained on NF_80/CNF substrates by applying constant current density of -0.05 A cm^{-2} ($Ni(OH)_2$_g16/NF_80/CNF) and constant potential of 1.1 V ($Ni(OH)_2$_pot16/NF_80/CNF) are shown on the Figure 35a and b. The mass load of selected deposits is equal to 16 mg cm^2.

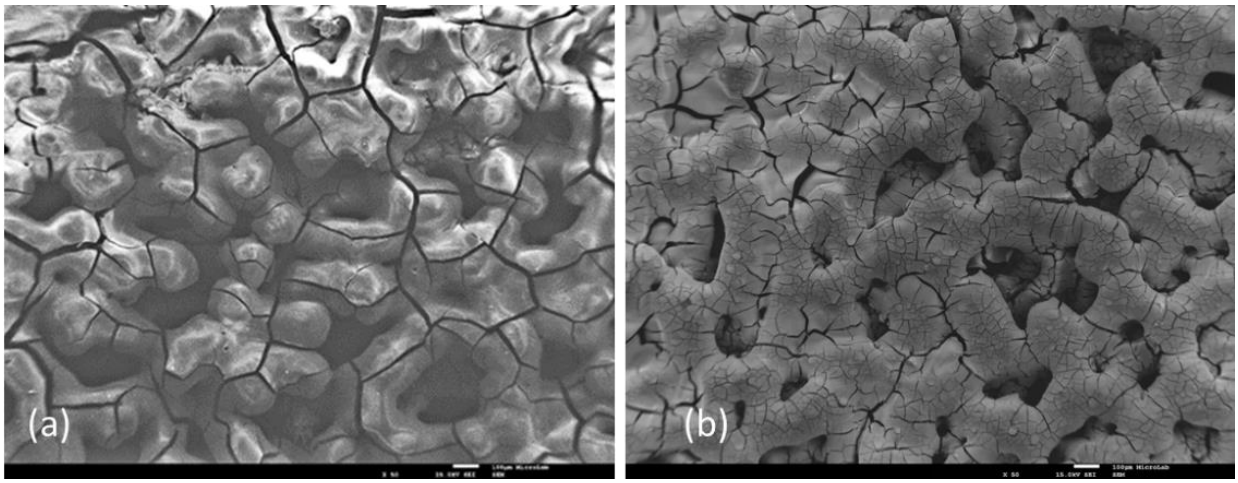

Figure 35. Comparison of morphologies of the composites $Ni(OH)_2$/NF/CNF obtained from solution 2 by (a) galvanostatic and (b) potentiostatic electrodeposition (at magnification 50X)

Surface analysis shows that both electrodeposition conditions produce similar smooth films of Ni hydroxide with surface morphologies analogous to the morphology of the substrate. This reveals that the electrodeposited Ni hydroxide homogeneously cover the original porous morphology of NF/CNF composites. For both deposition techniques Ni hydroxide shows surface cracks, that may be caused by drying process. Though, a higher cracking tendency is observed in the Fig. 35a. Also, the deposit obtained galvanostatically demonstrates larger pores compared to the potentiostatically produced sample. These differences may be associated with different potential and current response during electrodeposition process. As a result, 2 types of 3D hierarchical material composed of Ni hydroxide as active material and NF/CNF as current collector are produced. These samples were selected for further characterization.

9.3.2 Raman spectroscopy analysis

The Raman spectra of the films obtained in galvanostatic (Fig. 36a) and potentiostatic (Fig. 36b) electrodeposition modes showed very similar profiles. The peak positions, intensities and peak width, in both samples, correspond well to the spectra of α-$Ni(OH)_2$ prepared from $Ni(NO3)_2$ as described in a literature [76]. The small shift of peaks between samples appeared for all detected bands and can be explained by morphological differences as described in Chapter 9.3.1. As shown on the Fig. 36a and b, both films display a sharp peak with medium intensity at ~ 460 cm^{-1}, a peak with weak intensity at ~ 1620 cm^{-1} and a large sharp peak at ~ 3640 cm^{-1} assigned to α-$Ni(OH)_2$. Several NO_3^- bends were measured at approximately ~712-715 cm^{-1} and ~1291-1294 cm^{-1}. Free H_2O that is present within the material is measured at 3240 cm^{-1}. Therefore, the Raman identification is consistent with the products expected from the electrochemical and precipitation reactions described earlier (Eq. 21-23).

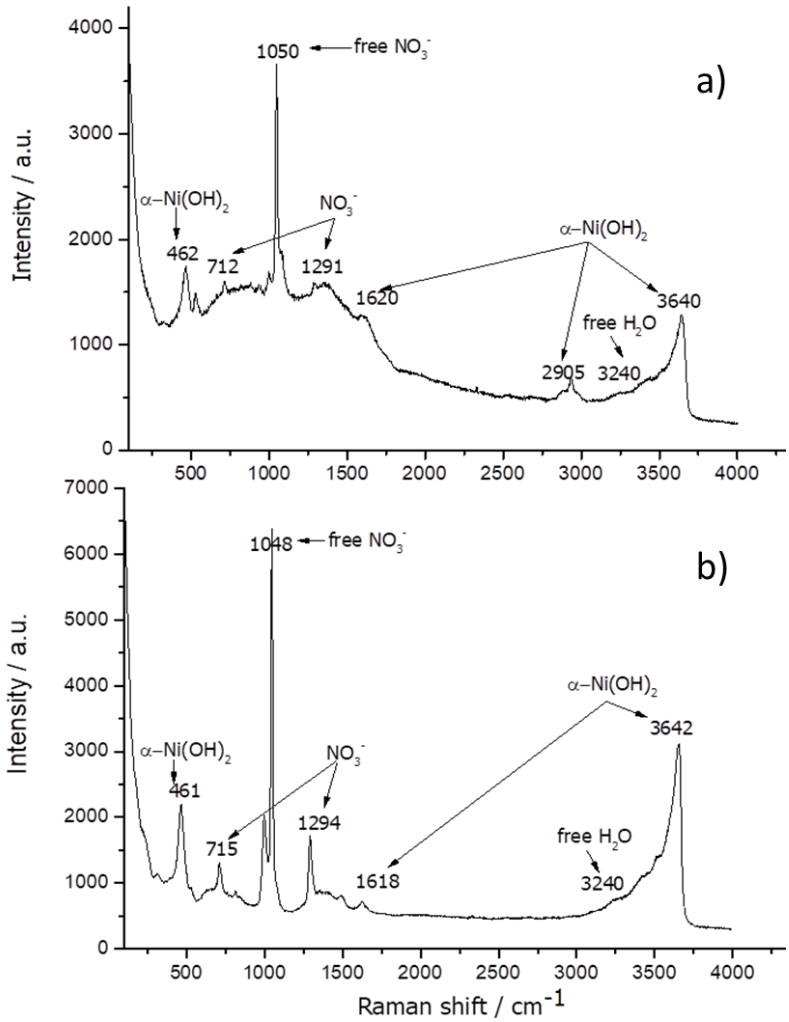

Figure 36. Raman spectra of $Ni(OH)_2$/NF/CNF electrodes prepared a) galvanostatically, b) potentiostatically

9.3.3 Electrochemical characterization of $Ni(OH)_2$/NF/CNF composites

The cyclic voltammograms of different samples of electrodeposited $Ni(OH)_2$ measured at rate of 2 mV s^{-1} within a potential window from 0 V to 0.55 V are depicted on Fig. 37. The CV curves evidence the presence of a pair of broad peaks. It is well known that the Faradic processes for charge storage in the hydroxide film proceed according to the reaction presented earlier with Eq. 19. The current response of the active material deposited over NF_80/CNF composites is stronger than over the blank commercial foams. This is probably due to the characteristics of the current collector which may enhance electronic conductivity. When comparing $Ni(OH)_2$_pot16/NF_80/CNF and $Ni(OH)_2$_g16/NF_80/CNF electrodes, CVs show similar curves, with a trend similar to that typical for a battery type material, and reveal a quasi-reversible character. However, potentiostatically deposited samples in comparison with galvanostatically deposited exhibits more symmetrical shape of redox peaks, that can be associated with higher reversibility.

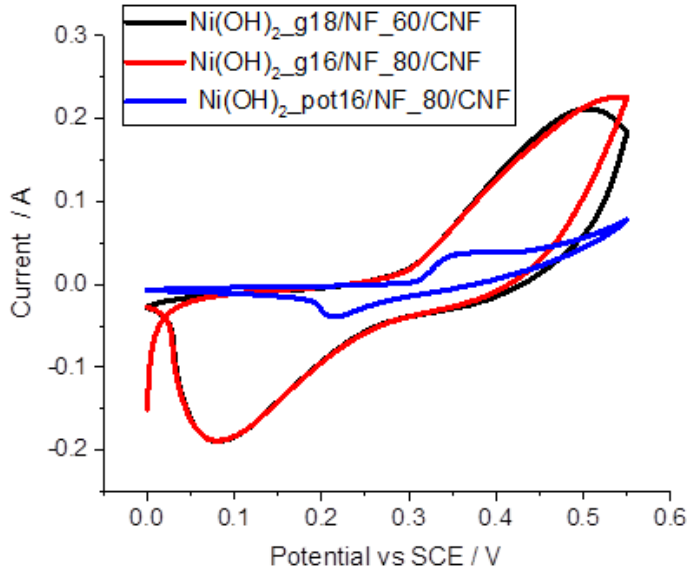

Figure 37. Comparison of performances of different materials at 2 mVs^{-1}

The redox response of the potentiostaticaly prepared composites was further evaluated by voltammetric cycling at different scanning rates from 2 mV s^{-1} to 10 mV s^{-1} (Fig. 38). At higher scan rates the shape of the cyclic voltammograms demonstrate changes. The CVs show that the anodic peaks disappeared, and the cathodic peaks are shifted to the negative direction. This is may be due to polarization of the electrodes at faster scan rates and increase of the system resistance.

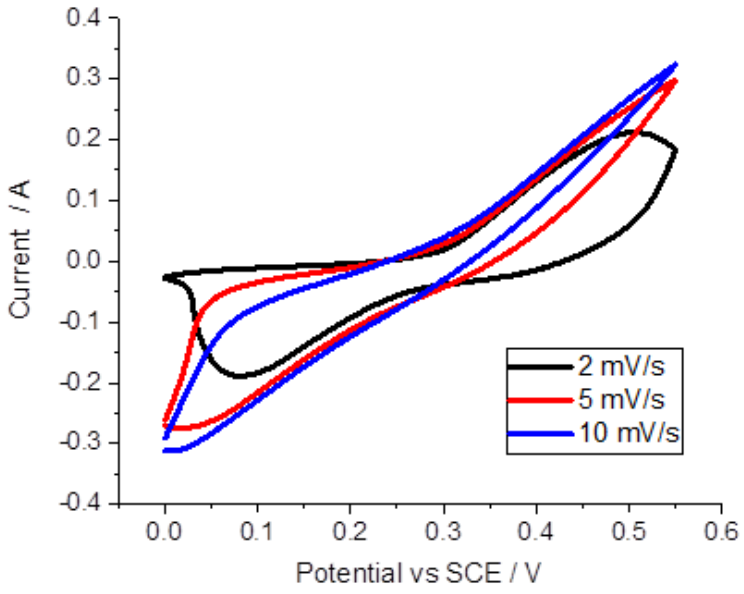

Figure 38. Comparison of performances of $Ni(OH)_2$_pot16/NF_80/CNF at different sweep rates

The GCD measurements of electrodeposited hydroxide films were performed under a constant current density of -7.5 mA cm^{-2}. The results show the presence of plateau in the discharge curves for all electrodes studied. The values of specific capacity of the active material $Ni(OH)_2$ presented in Tab. 13, were calculated from these discharge curves using Eq. 9 described in methodology. Taking into account the fact the weight of the deposited active material is nearly the same, the presented results reveal a strong influence of the type of electrode support on the overall electrochemical performance of the electrode.

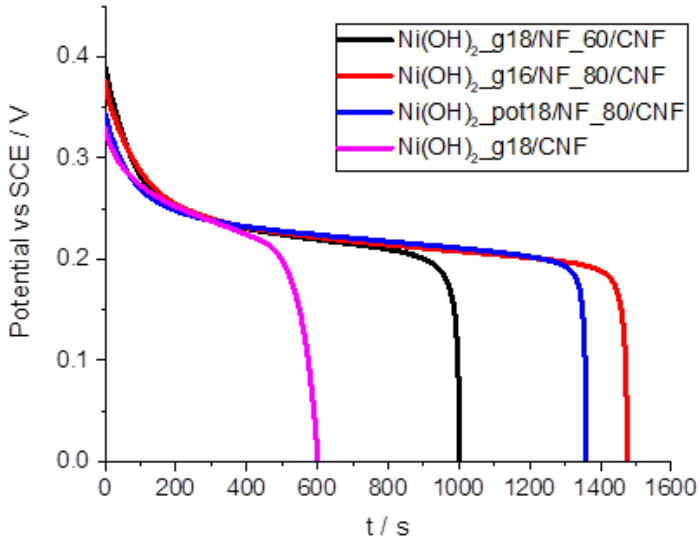

Figure 39. Comparison of discharge curves of different materials at applied current density of -7.5 mA cm^{-2}

Here, the highest specific capacity of 192 mAh g^{-1} and 177 mAh g^{-1} correspond respectively to the active material electrodeposited galvanostatically and potentiostatically on the NF_80/CNF substrate. However, further observations demonstrate significant capacity decrease for both samples.

Table 13. Specific capacity of $Ni(OH)_2$ films calculated from GDC at current density of -7.5 mA cm^{-2}

Sample	Specific capacity mAh g^{-1}
$Ni(OH)_2$_g16/NF_80/CNF	192
$Ni(OH)_2$_g18 /NF_60/CNF	116
$Ni(OH)_2$_pot18 /NF_80/CNF	177
g18/CNF	63

As can be seen on Fig. 40, the $Ni(OH)_2$_g16/NF_80/CNF electrode revealed higher capacity fade compared to $Ni(OH)_2$_pot16/NF_80/CNF, probably due to morphological differences associated with the electrodeposition route.

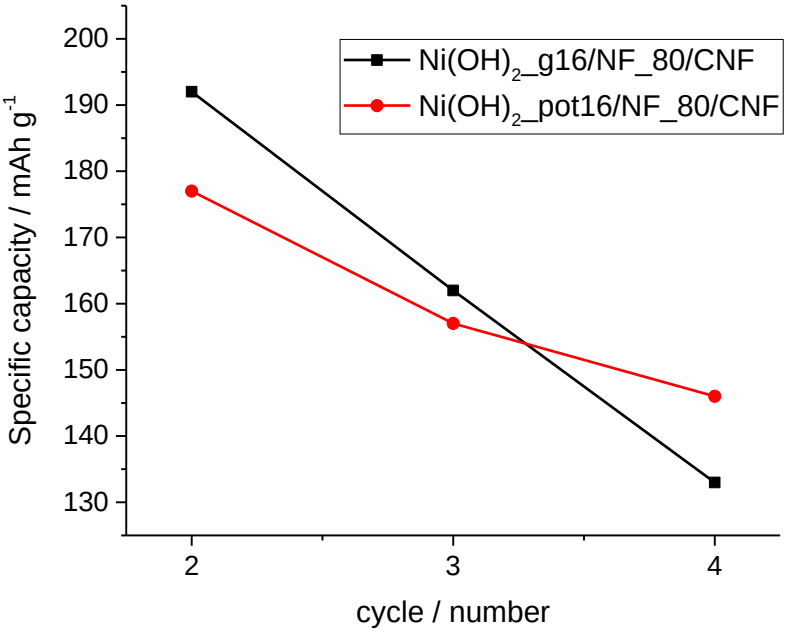

Figure 40. Comparison of specific capacity retention curves of different samples at -7.5 mA cm^{-2}

A cyclic stability of $Ni(OH)_2$_pot16/NF_80/CNF electrode was evaluated by applying constant current density of -25 mA cm^{-2} for 500 cycles. As can be seen on Fig. 41, the discharge time of the tested electrode has dropped significantly over 500 cycles. This may be associated with detachment of the active material from the surface of the electrode support, an effect that was experimentally observed after the GCD measurements. Since all the electrodes with the active material obtained by electrodeposition showed low mechanical stability, they were not selected for further tests in a 2-electrodes electrochemical cell.

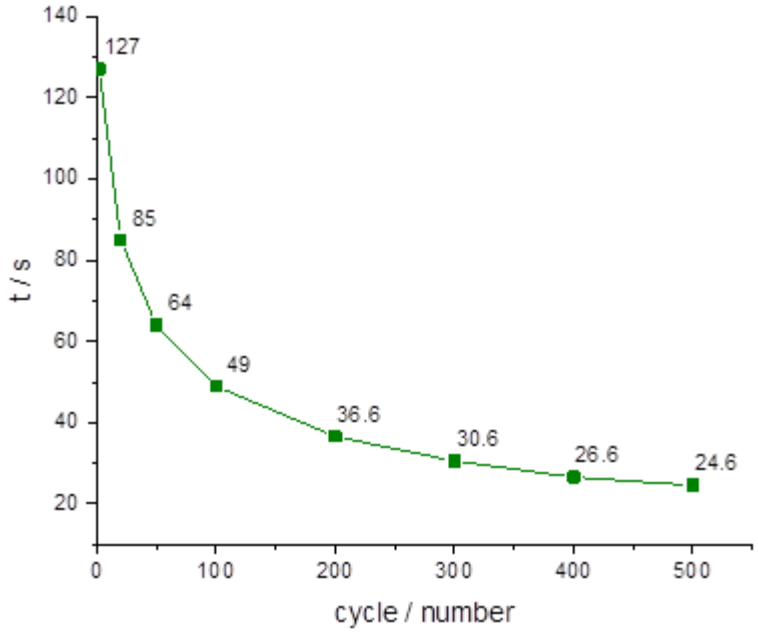

Figure 41. Discharge time of $Ni(OH)_2$_pot16/NF_80/CNF at different cycles at -25 mA cm^{-2}

10. $Ni(OH)_2$/NF/CNF electrodes prepared in C2C-NewCap laboratory.

The fabrication of $Ni(OH)_2$/NF/CNF electrodes was performed by filling pores of NF_80/CNF support with an active material Ni hydroxide using C2C-NewCap company method. Selected electrodes were calendared (electrode compression).

10.1 Results from chemical precipitation

Tab.14 presents the results of the synthesis of the $Ni(OH)_2$/NF/CNF electrodes. As expected, a cycle of fabrication procedure generated an active material $Ni(OH)_2$ as a precipitate on the porous surface of the NF_80/CNF. Depending on the number of cycles used during experiments, the fabricated electrodes were divided into two groups: the ones formed after the 1st cycle, and the ones formed after the 2nd cycle. Therefore, the synthesized nickel hydroxide electrodes are represented as L1 (as-prepared with 1 cycle) and L2 (as-prepared with 2 cycles). The calendared electrodes were marked with an additional index “cal” (L1_cal and L2_cal). The number of cycles showed strong dependency on the amount and structure of precipitated Ni hydroxide. The first cycle generated a blue-green bulky precipitate (L1) with randomly aggregated particles loosely attached on the surface of NF_80/CNF substrate. With the second cycle these agglomerated particles detached, and $Ni(OH)_2$ loaded as a homogenous film. After roll pressing the thickness of the electrodes decreased. The surface of the calenderer electrodes looked shiny compared to the as-prepared equivalents that looked matte. The results demonstrate that calendared electrodes exhibit lower mass load of $Ni(OH)_2$ compared to non-calendared samples (Tab.14). This is because during roll pressing some of precipitated $Ni(OH)_2$ detached from the NF_80/CNF substrate. The loss of the active material was experimentally observed in a form of light-green powder on the rolls of the compacter. Fabricated electrodes L1, L2 and L2_cal were subjected to the further characterization. Non-calendared L1 composite, as mentioned earlier, demonstrated mechanical instability, and therefore it was rejected for subsequent experiments.

Table 14. Description of the composites prepared at C2C-NewCap laboratory

Index	Initial material	Number of cycles	Calendaring	$Ni(OH)_2$, mg cm^{-2}	Observations
L1	NF_80/CNF	1	no	47	Bulky precipitation, some material detachment from the substrate after drying.
L1 _cal	NF_80/CNF	1	yes	15	Well-compacted into porous substrate
L2	NF_80/CNF	2	no	20	Homogenous thin layer well adhered to the substrate
L2 _cal	NF_80/CNF	2	yes	15	Homogeneously well-compacted into the porous substrate

10.2 Characterization

10.2.1 Morphological characterization of the electrodes with active material Ni(OH)2 fabricated with C2C-NewCap method

Typical of SEM images of the outer surface of the synthesized $Ni(OH)_2$/NF/CNF electrodes prepared by two cycles of C2C-NewCap method is illustrated in Fig. 42. The micrographs were taken at different magnifications before (L2, Fig. 42a-b) and after (L2_cal, Fig.42c-d) calendaring. The sintered electrode provided by C2C-NewCap (StE) is also shown for comparative reasons (Fig. 42e-f).

The micrograph of as-prepared L2 electrode (Fig. 42a) demonstrates that precipitated Ni does not hinder the porous morphology of the NF_80/CNF substrate, however the distribution of the active material is not fully homogeneous. Higher magnification (Fig. 42b) reveals that $Ni(OH)_2$ is composed of irregular shaped particles which are interconnected with each other randomly.

It is shown on the Fig.28c that after roll pressing the porosity of the electrode is significantly reduced compared to its as-prepared equivalent (Fig. 42a). L2_cal demonstrates well-compacted surface similar to StE (Fig. 42e), which is expected since the fabrication of both electrodes was finished with calendaring. However, unlike StE coating, L2 reveals visible cracking throughout the electrode surface. This is most likely because originally pores of NF_80/CNF current collectors are much larger than that of sintered nickel S/CNF, as discussed in Chapter 8.3. High magnification micrographs (Figs. 27d, 27f) demonstrate severe damage of Ni hydroxide particles caused by the mechanical pressure, which is applied during the compacting process. Overall, the results obtained from SEM analysis give us an important overview on the influence of the fabrication techniques on the electrode morphology. These results are also used to further explain the effects of electrode morphology on electrochemical performance and on cyclic stability.

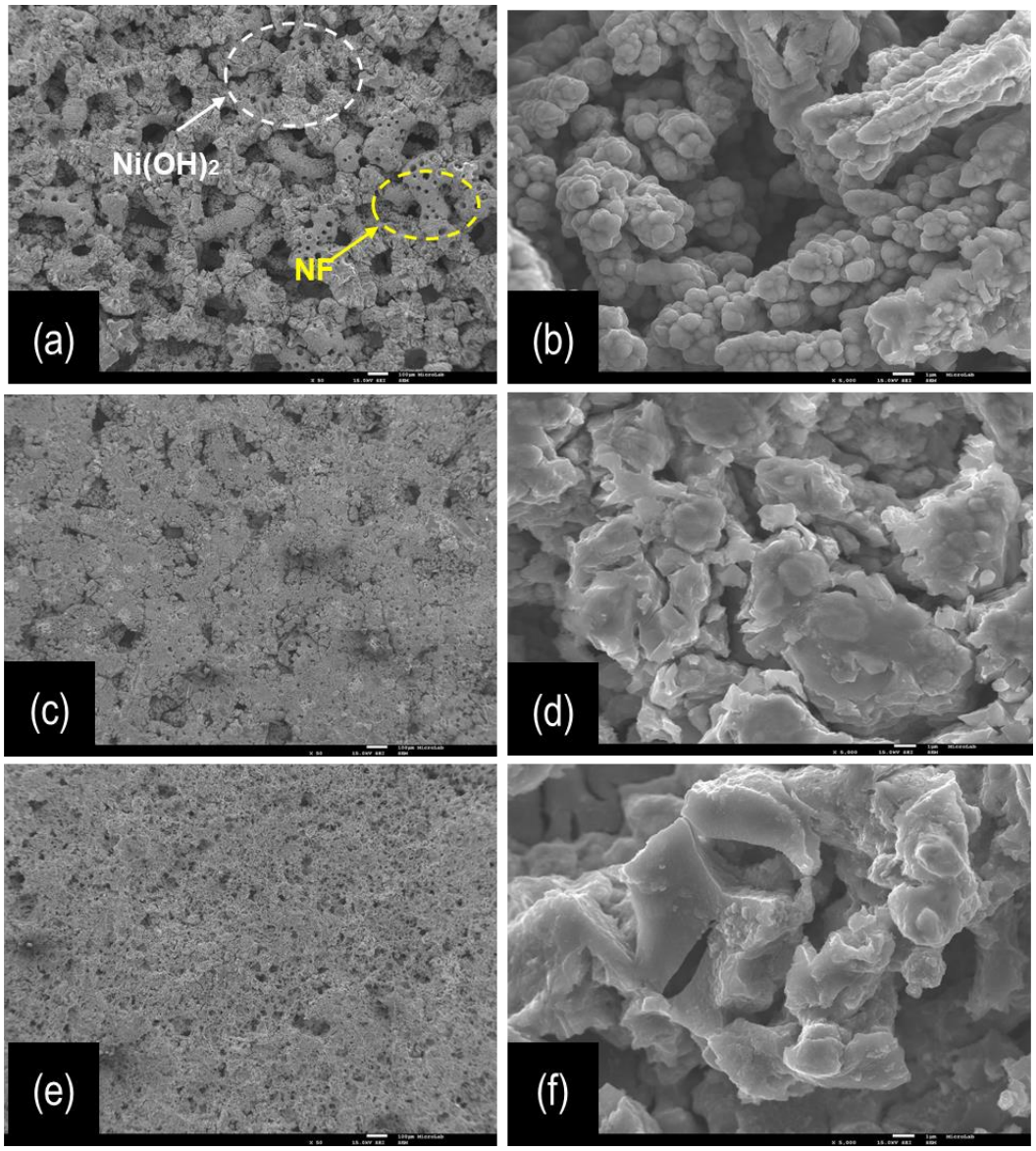

Figure 42. SEM images at different magnifications of Ni hydroxide on the NF_80/CNF substrate before (a-b) and after (c-d) calendaring; and StE electrode (e-f)

10.2.2 Raman spectroscopy analysis

Raman experiment was carried out to determine the spectral characteristics of the active material $Ni(OH)_2$ which was synthesized by C2C-NewCap method. The result of Raman measurements of L2 electrode is graphically depicted on the Fig. 43. Note that all the sintered electrode StE provided by C2C-NewCap demonstrated similar response.

The appearance of the 478/557 cm^{-1} doublet is assigned to the NiO(OH) stretching [77] . Two weak peaks observed at ~790 cm^{-1} and at ~1072 cm^{-1} indicate that the structure of $Ni(OH)_2$ corresponds to alpha phase.

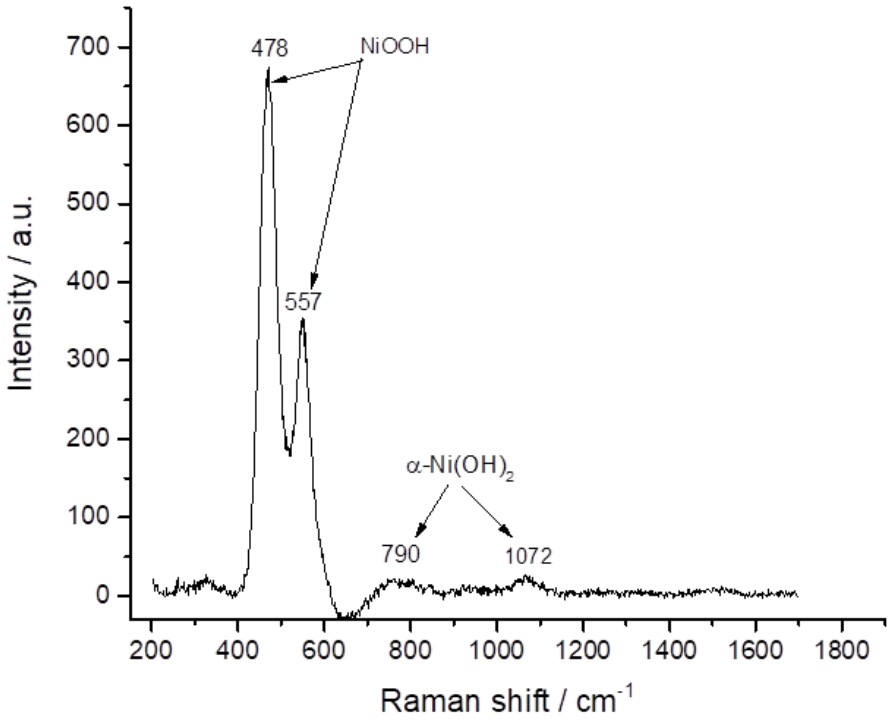

Figure 43. Raman spectrum of $Ni(OH)_2$ synthesized by C2C-NewCap method

10.2.3 Electrochemical characterization

The electrochemical performance of synthesized $Ni(OH)_2$ electrodes was examined via CV and galvanostatic charge-discharge techniques. The sintered electrode StE provided by C2C-NewCap company was also evaluated for comparative reasons. Multiple samples of each electrode type were tested to ensure the repeatability of the electrochemical results. The cyclic voltammograms of the L1_cal, L2, L2_cal and StE electrodes are shown on the Fig. 44. The measurements were taken in 1 M KOH electrolytes with the sweep rate of 2 mV s^{-1} ranging the potential from -0.2 V to 0.8 V. The shape of the CV curves confirmed the typical Faradaic redox reaction which corresponds to the oxidation and reduction process as shown in Eq.19. The intensity of the anodic and cathodic peaks is equivalent for all the presented curves. However, the presence of asymmetry in the shape of CVs reveals a quasi-reversible nature. The synthesized electrodes demonstrate CVs with higher current responses, which represents the improved electrochemical behavior in comparison with StE electrode.

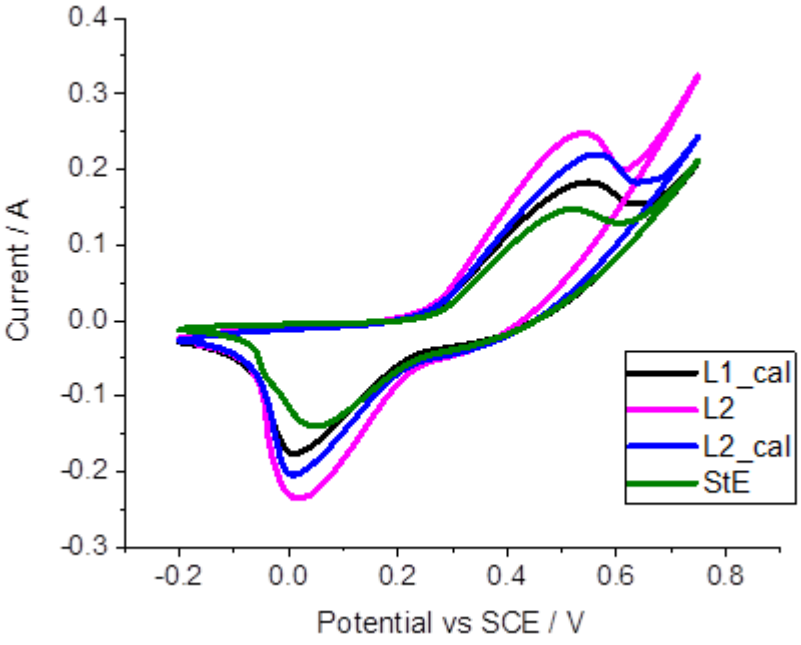

Figure 44. Comparison of performances of different materials at 2 mV s^{-1}

Chronopotentiometry tests were carried out to evaluate specific capacity of the electrodes. Fig. 45a-c show the comparison of discharge curves of L1_cal, L2, L2_cal and StE electrodes measured in 1 M KOH electrolyte at different current densities (from -7.5 to -25 mA cm^{-2}). The plateau-like profiles of the discharge curves depict the performing of a battery-type redox reaction. Here, the synthesized electrodes possess the longer discharge time than StE electrode at all discharge currents. The results are consistent with the CV curves. The specific capacity of the synthesized L1_cal, L2, L2_cal and StE electrodes were calculated from the galvanostatic discharge curves using the Eq. 4 presented in methodology. The results of calculations are summarized in the Tab. 15 and graphically are depicted in Fig.46.

It was observed that all electrodes demonstrate the decrease of discharge time (Fig. 45), and therefore specific capacity, with an increase of applied current. This is probably because during electrode charging at lower currents the OH^- ions have more time to diffuse into the surface of $Ni(OH)_2$ than that at higher currents [10]. The calculated specific capacity values of the $Ni(OH)_2$/NF/CNF electrodes are significantly higher in comparison with StE electrode. Considering that the active material $Ni(OH)_2$ is the same for all the tested samples, larger specific capacity of the $Ni(OH)_2$/NF/CNF electrodes may arise from more efficient utilization of this active material. The open pore morphology (L2) or surface cracks (L2_cal) observed on SEM images (Fig. 42a, c) may increase the number of active sites available for redox reactions.

Also, among the tested electrodes, L1_cal and L2_cal showed the best results, which lead to conclusion that calendering improved electrochemical performance of the electrodes. This is probably because after the roll

pressing the uniformity of the active material in the electrode is increased, which may improve an electric contact between the active material Ni hydroxide and current collector Ni_80/CNF.

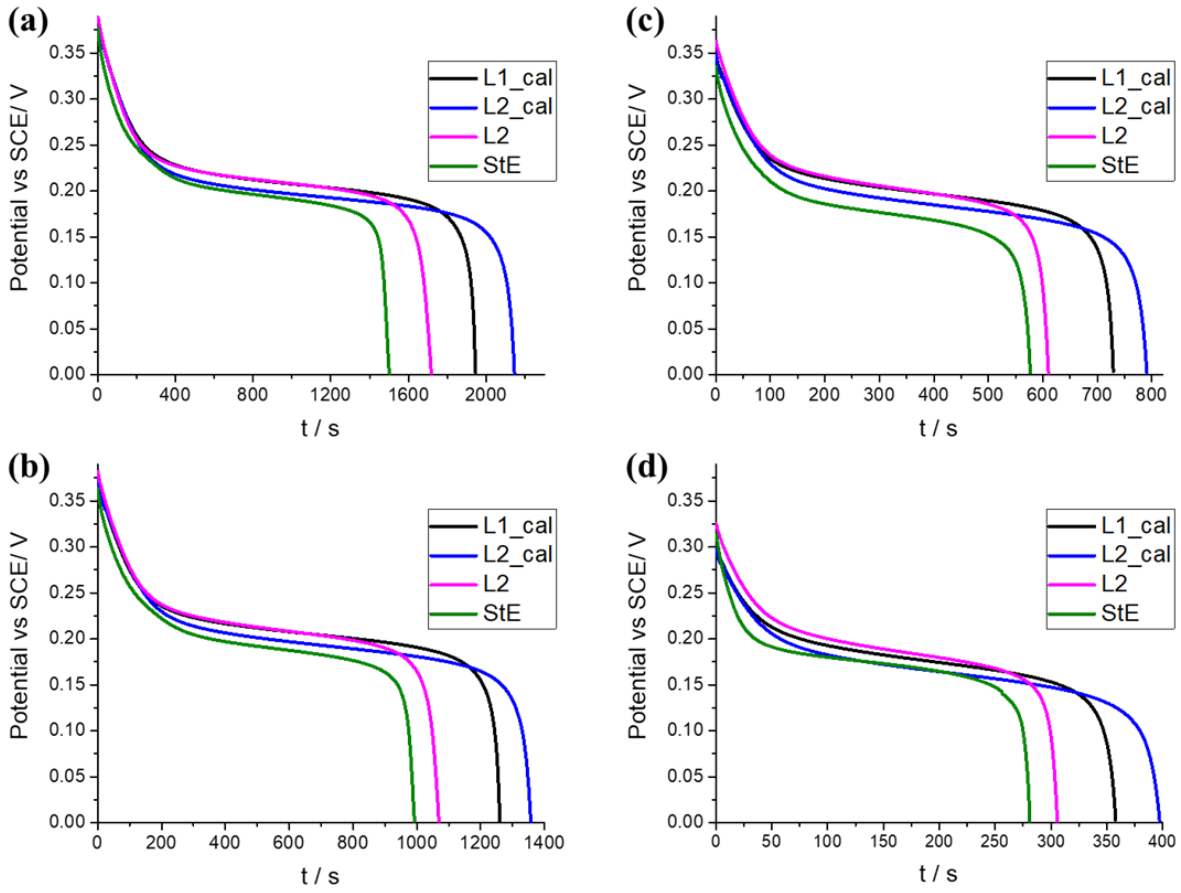

Figure 45. Comparison of discharge curves of different materials at current densities of (a)7.5 mA cm^{-2}, (b)10 mA cm^{-2}, (c) 15 mA cm^{-2}, (d) 25 mA cm^{-2}

Table 15. Calculated specific capacity of the electrodes in mAh g^{-1}

Index	7.5 mA cm^{-2}	10 mA cm^{-2}	15 mA cm^{-2}	25 mA cm^{-2}
L1_cal	253	237	153	119
L2_cal	298	251	220	72
L2	179	149	127	43
StE	78	69	60	19

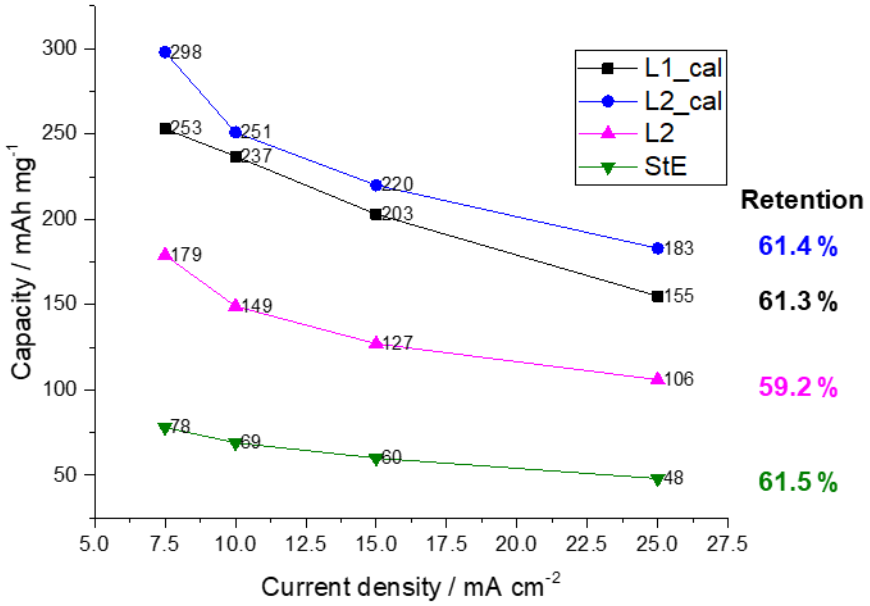

Figure 46. Capacity retention of synthesized electrodes at different discharge currents

Overall, each tested electrode performed in total of 20 charge/discharge cycles (4 cycles for each current applied). To estimate mechanical stability, after GCD test the electrodes L1_cal, L2 and L2_cal were rinsed thoroughly using deionized water, dried at 60ºC for 24h and then weighted. The difference in electrode mass before and after tests was associated with loss of the active material $Ni(OH)_2$ - detached Ni hydroxide particles were observed as a residue on the bottom of the glass cell after GCD tests were completed. The obtained results revealed that $Ni(OH)_2$ mass in L1_cal and L2 reduced by 40% and 60% respectively, while L2_cal appeared comparatively stable with reduction by 10% from the original active material mass. The difference in mechanical stability may be attributed to the morphological differences associated with fabrication procedures, as discussed earlier (Chapter 10.2.1). Note that the NF_80/CNF current collector has interconnected porous network, and the $Ni(OH)_2$ particles impregnated inside these pores may have loose contact with the metal foam of NF_80/CNF. After calendering Ni hydroxide particles are sealed inside the pores of current collector. This may explain the fact calendared electrodes L1_cal and L2_cal appeared mechanically more stable than non-calendered L1.

The cyclic stability of the electrodes is an essential parameter for their practical application [78]. Therefore, due to high level of mechanical degradation demonstrated by L1_cal and L2 these electrodes were rejected for the further tests. Next, the cyclic stability of nanostructured L2_cal electrode was carried out in charge-discharge test at constant current density of 25 mA cm^{-2} for 1000 cycles. For comparative reason StE electrode was also cycled at the same conditions. The capacity retention of L2_cal and StE electrodes is graphically depicted on the Fig. 47. The results indicate that after 1000 cycles L2_cal electrode demonstrate

specific capacity drop by 75%, while StE by 53% of the initial value at the second discharge cycle. The specific capacity fade of L2_cal electrode is the consequence of degradation mechanism in which the active material detached from the current collector. However, the final value of specific capacity of L2_cal is still higher than that of StE electrode. Therefore, L2_cal was selected for the final test as a positive electrode in a hybrid cell.

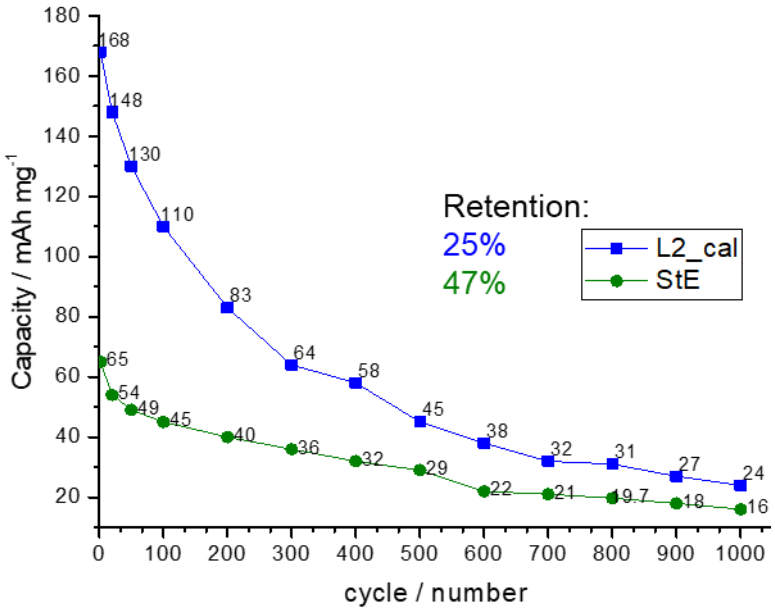

Figure 47. Capacity retention of L2_cal and StE electrodes at 25 mA cm^{-2} over 1000 cycle

11. Assembling asymmetric electrochemical cell

To evaluate performance of the L2_cal electrode for practical applications, the asymmetric electrochemical cell was designed using the L2_cal as the positive electrode and the carbon based AC-sheet as the negative electrode. This system was marked with an index L2_cal //AC. For comparative purposes the cell of similar configuration, where StE served as a positive electrode and AC-sheet as a negative electrode was also fabricated and examined (StE//AC). All the electrochemical tests were carried out in 1M KOH electrolyte. The geometrical area of the positive and negative electrodes immersed into the electrolyte was kept identical (as 2 cm^2). To estimate a working potential of the asymmetric device, the AC-sheet electrode and L2_cal electrode were evaluated by cyclic voltammetry in a three-electrode system at rate of 2 mV s^{-1} (Fig. 48a-d).

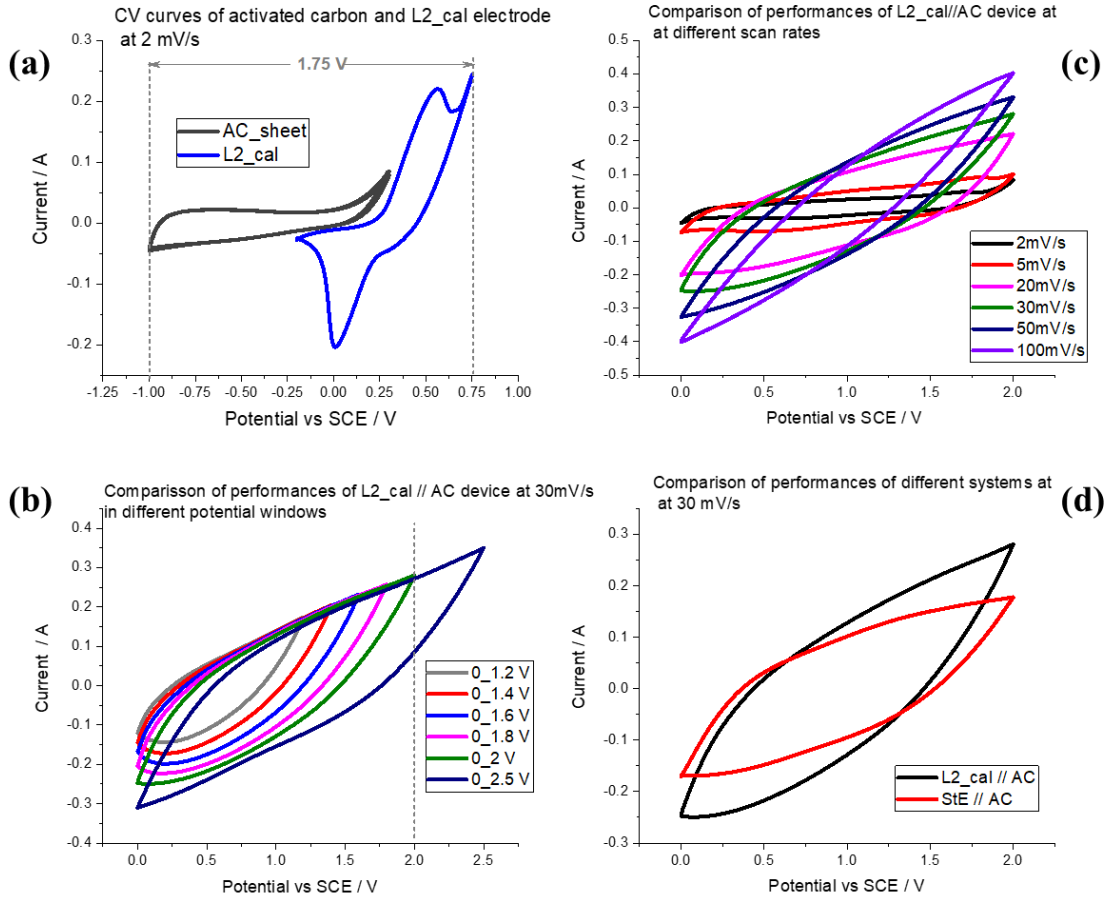

Figure 48. (a) CV curves of L2_cal and AC_sheet half cells in 1 M KOH solution at the scan rate of 2 mV s^{-1}; (b) CV curves of the L2_cal//AC tested at different potential windows ranging from 0.0 to 2.5 V; (c) CV curves of the L2_cal//AC tested at different scan rates ranging from 2 to 100 mV s^{-1}; (d) comparison of CV curves of L2_cal//AC and StE//AC tested at 30 mV s^{-1} at potential window from 0 to 2.0 V

Fig.48a shows that the voltammogram of the AC electrode reveals a typical of a carbon-based material rectangular-like shape in a potential range of −0.2 to +0.76 V, while the CV curve of the L2_cal electrode exhibits a pair of a battery-type redox peaks in a potential range of −1.0 to +0.3 V.

Therefore, the L2_cal//AC is expected to have a working potential of around 1.75 V. In order to confirm the estimated potential window, the L2_cal//AC device was additionally cycled in different potential windows from 0.0 to 2.5 V, as depicted in Fig. 48b. The CVs demonstrate capacitive behaviour and the shape of the voltammograms remains stable with a good reversibility up to 2.0 V. At higher potential the shape of the CV slightly altered, which is probably due to decomposition of the electrolyte by oxygen evolution [79]. This means the stable operation cell voltage of L2_cal//AC can be higher than it was estimated previously and is approximately 2.0 V.

Fig. 48c shows the CV curves of L2_cal//AC device measured at different scan rates starting from 2 to 100 mV s^{-1} at the potential range of 0 – 2.0 V. At lower scan rates (2 and 5 mV s^{-1}) the CV profile retains nearly rectangular shape, however with the significant increase in the scan rate (above 20 mV s^{-1}), the CV is distorted into tilted rectangular indicating increase in the system resistivity. Although the CV plots of the StE//AC recorded at the same conditions showed lower current response than that recorded for L2_cal//AC device, the later one demonstrated slightly higher resistance (Fig. 48d), that may be assigned to the difference in fabrication method.

Fig. 49a and b show typical chronopotentiograms of the asymmetric devices L2_cal//AC and StE//AC, respectively, recorded in potential window from 0.0 to 1.5 V applying different discharge currents from -15 to -50 mA. The discharge plots of both systems demonstrate near-linear profiles. However, it is noticed for both systems that at lower discharge currents (-15, -20, -30 mA) the curves demonstrate deviation from the linear shape starting from potential of 0.2 to 0.0 V. This fact may be attributed to the speed of the hydroxil ion diffusion, which occurs during redox reaction at the positive electrode, as discussed in Chap. 3.1. The GCD curves of L2_cal//AC and StE//AC demonstrate nearly-symmetrical triangular shape with a small IR-drop (Fig. 49c), which confirms a good capacitive behaviour of the systems.

The calculations performed with Eq.13, indicate that L2_cal//AC has superior charge-discharge efficiency rate (93%) in comparison to StE//AC (82%). The specific capacitance, power and energy densities of the L2_cal//AC and StE//AC devices were calculated from the discharge curves at different currents from -15 to -50 mA, as described in methodology (Chapter 7.4) and are summarized in Tab. 16. The variation of specific capacitance values as a function of the current (Fig. 50b) demonstrate that the specific capacitance of the L2_cal//AC is higher than that of the StE//AC device. The Ragone plots (Fig. 50b) graphically illustrates that at the same discharge currents the L2_cal//AC system shows higher specific power and specific energy values for in comparison to that of delivered by the StE//AC.

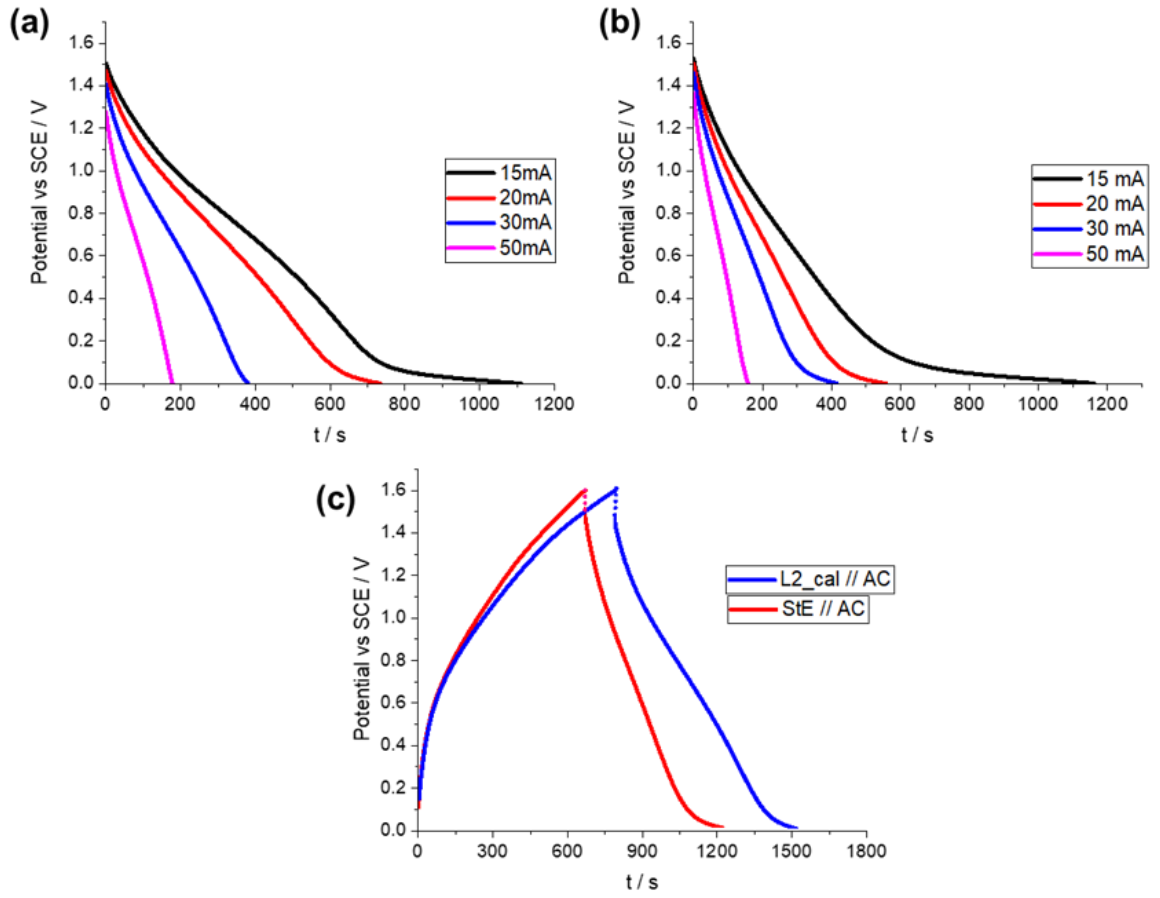

Figure 49. Galvanostatic discharge curves at different currents from -15 to -50 mA of (a) L2_cal//AC, (b) StE//AC; (c) Galvanostatic charge-discharge curves of L2_cal//AC and StE//AC at 20 mA

Table 16. Electrochemical performance of L2_cal // AC and StE// AC devices

		15 mA	20 mA	30 mA	50 mA
C_s [F g^{-1}]	L2_cal // AC	151	141	113	81
	StE // AC	114	74	85	59
P_{real} [W kg^{-1}]	L2_cal // AC	156	203	292	521
	StE // AC	114	150	216	337
E_{real} [Wh kg^{-1}]	L2_cal // AC	47	42	31	25
	StE // AC	37	23	24	15

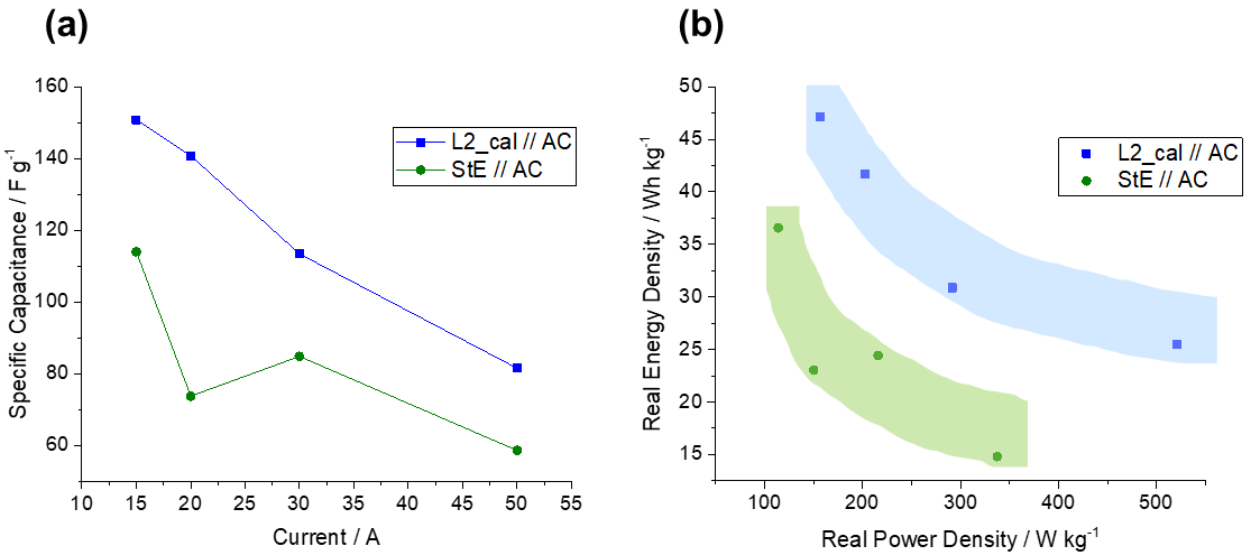

Figure 50. Electrochemical performance of L2_cal//AC and StE//AC devices at different discharge currents from 15 to 50 mA: (a) Specific capacitance [Fg^{-1}], (b) Ragone plots

IV. Conclusions

The objective of the present thesis was to develop and to test a novel nanostructured electrode for the hybrid supercapacitor. As depicted schematically on the Fig. 51, the work included fabrication of the electrode supports (Step 1) and then filling the pores of the as-prepared electrode supports with an active material nickel hydroxide (Step 2).

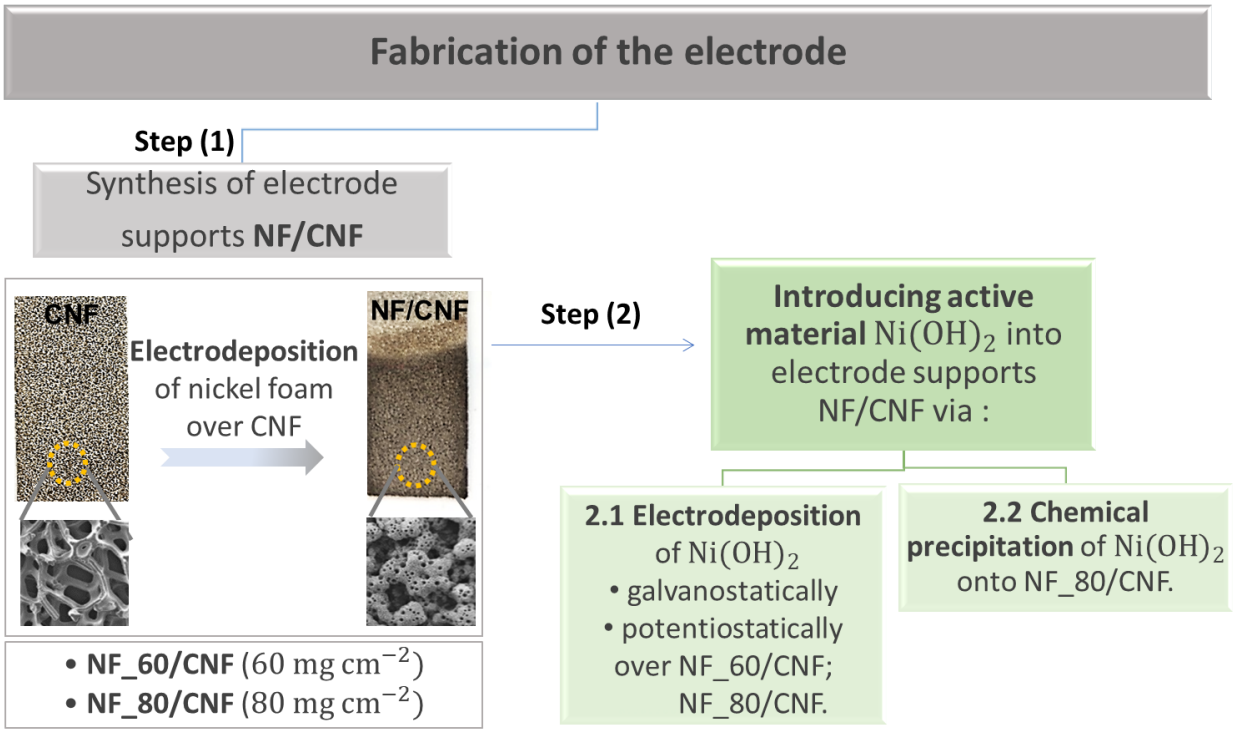

Figure 51. Schematic illustration of the experiments

(1) The electrode supports were fabricated by electrodeposition of nanostructured nickel foams NF directly on commercial nickel foam CNF substrates that served as the current collector. The experimental results proved that the mass of deposits increased with the increase of deposition time and the value of applied current density. The optimization of the electrodeposition parameters (time and current density) resulted in a set of two optimized composites with a mass of nickel deposit of 60 mg cm^{-2} (NF_60/CNF) and 80 mg cm^{-2} (NF_80/CNF), which displayed the intended morphology. The electrochemical performance of the composites was studied using cyclic voltammetry and chronopotentiometry techniques.

Cyclic voltammetry of NF_60/CNF and NF_80/CNF measured in the potential window from 0 V to 0.55 V in 1M KOH revealed one pair of redox peaks for both composites. The phenomena are related to the faradaic

reactions of nickel occurred in alkaline electrolyte. NF_80/CNF composite demonstrated higher current response in cyclic voltammograms and longer discharge time during chronopotentiometry tests if compared to NF_60/CNF. The specific capacity calculated from the GCD curves at 7.5 mA cm^{-2} for NF_80/CNF composite is 8 mAh g^{-1} which is twice higher than that of 4 mAh g^{-1} for NF_60/CNF.

The electrochemical characterization of the heat-treated NF_80/CNF composites showed that with increase of the heat treatment temperature, from 350ºC to 450ºC, the electrochemical response is poorer in comparison with as-prepared composite, meaning that more semiconducting nickel oxides was formed on the surface of the nickel nanofoam deposit.

Morphological characterization of the NF_80/CNF composite surface proved significant reduction of the pore size compared to the bare CNF. The nickel nanofoam deposit demonstrated a uniform sponge-like morphology where the pores were formed by hydrogen bubble evolution during the electrodeposition process. Higher magnification images revealed that the deposit is composed of small agglomerates of Ni grains.

Based on the morphology and electrochemical response raw composites NF_80/CNF and NF_60/CNF were selected to be used as electrode supports in the present work.

(2) The second part included the experiments to fill an active material nickel hydroxide into the porous structure of as prepared electrode supports to fabricate the electrodes. Three different techniques including electrochemical deposition in both (2.1) galvanostatic and potentiostatic modes as well as (2.2) the patented by C2C-NewCap chemical precipitation method were used.

Raman spectroscopy analysis indicated that the structure of the synthesized active material $Ni(OH)_2$ in all the types of fabrication techniques used in the present work corresponded to alpha phase. Therefore, the electrochemical characterization of the electrodes is demonstrating the crucial importance of the electrode architecture on the overall electrode performance.

(2.1) The results obtained from electrochemical characterization revealed that specific capacity of the electrodes with the active material electrodeposited over nonporous nickel composites NF_80/CNF (up to 192 mAh g^{-1}) and NF_60/CNF (up to 116 mAh g^{-1}) is significantly higher than that of the electrodes with nickel hydroxide over the blank commercial foams CNF (up to 63 mAh g^{-1}). The superior performance may result from the enhanced ionic/electronic conductivity achieved by introducing nanostructured electrode supports.

All the electrodes with the active material obtained by electrodeposition showed high mechanical degradation during electrochemical tests. Electrodes with an active material electrodeposited galvanostatically demonstrated higher mechanical instability compared to the electrodes with potentiostatic electrodeposition. This is probably due to morphological differences associated with electrodeposition mode.

(2.2) The fabrication of the electrodes by chemical precipitation method was performed by introducing the active material Ni hydroxide directly onto the NF_80/CNF support following C2C-NewCap fabrication procedure. Selected electrodes were calendared. The optimization of the fabrication procedure resulted in the set of 3 electrodes depending on the number of fabrication cycles (L1 and L2) and whether the electrodes were calendared or not.

The morphological characterization demonstrated that the surface of the calendared electrodes was well-compacted, and the porosity was significantly reduced compared to their as-prepared equivalents.

The electrochemical tests revealed that after roll pressing the electrodes exhibited improved electrochemical performance. This is probably due to better electric contact between the precipitated nickel hydroxide particles and the electrode support after calendering.

The electrodes fabricated via C2C-NewCap method in the present work demonstrated significantly higher specific capacity (up to 253 mAh g^{-1}) compared to current electrode from C2C-NewCap (78 mAh g^{-1}). The larger specific capacity may arise from more efficient utilization of this active material.

The results of the cyclic stability test carried out at 25 mA cm^{-2} showed that after 1000 cycles specific capacity of the calendared electrode L2_cal decrease by 75% of the value at the second discharge cycle. This specific capacity fade is the consequence of the detachment of the active material from the current collector during the cycling experiments.

12. Suggestions for future work

The results obtained in the present work for Ni nanofoams and their application as electrodes supports for supercapacitor electrodes have led to the following proposals for future work:

- Electrodeposition at current densities higher than 1.5 A cm^{-2}. During this work, the current value was limited by the equipment.
- Optimization of electrolyte composition. For example, change molar concentration of ammonium for modification of the foams morphologies. Since ammonium acts as a proton source for hydrogen evolution, it influences the surface pore density.
- Surface examination should also be considered after electrochemical testing to see morphological changes after numerous charge-discharge cycles.

In addition to the work already done in electrode synthesis, more experiments may be performed to find out the reasons for mechanical instability of the produced electrodes:

- Composition analysis employing different techniques would be performed on more samples;
- Electrochemical impedance spectroscopy study and analysis of the electrode at different state-of-charge conditions.

Assembling 2-electrode device may be done by:

- Balancing charge.
- In a battery-type Swagelok cell for electrochemical studies.

References

[1] U.S. Energy Information Administration (2017*), International Energy Outlook 2017*. [online] Available at: https://www.eia.gov/outlooks/ieo. [Accessed Dec. 2018].

[2] OECD (2018), *Economic Outlook for Southeast Asia, China and India 2018: Fostering Growth through Digitalisation*, OECD Publishing, Paris, doi:10.1787/9789264286184-en.

[3] IMF (2018). *World Economic Outlook Update, January 2018: Brighter Prospects, Optimistic Markets, Challenges Ahead*. [online] Available at: https://www.imf.org/en/Publications/WEO/Issues/2018/01/11/world-economic-outlook-update-january-2018 [Accessed Dec. 2018].

[4] OECD/IEA (2017), *Global Energy & CO2 Status Report*, March 2018, [online] Available at: https://www.iea.org/geco/ [Accessed Nov. 2018].

[5] S. Ugarte, B. Ree and J. Larkin (2015). *Energy Storage: Which Market Designs and Regulatory Incentives*. Brussels: European Parliament's committee on Industry, Research and Energy (ITRE). August 2015 [online] Available at: http://www.europarl.europa.eu/committees/en/supporting-analyses-search.html [Accessed Nov. 2018].

[6] European Commission. (2017). *Energy storage – the role of electricity.* Brussels. 2017. [online] Available at: https://ec.europa.eu/energy/sites/ener/files/documents/swd2017_61_document_travail_service_part1_v6.pdf [Accessed Nov. 2018].

[7] IEA (2017). *Energy Access Outlook 2017: From Poverty to Prosperity*, IEA, Paris, doi: 10.1787/9789264285569-en.

[8] Statistical Office of the European Communities (2018). EUROSTAT: *Renewable energy statistics*. [online] Availableat: June 2018 https://ec.europa.eu/eurostat/statistics-explained/index.php/Renewable_energy_statistics [Accessed Nov. 2018].

[9] European Commission (2011), *Energy roadmap 2050*, Luxembourg: Publications Office of the European Union, 2012. doi:10.2833/10759

[10] Dr. Chris Naish, Dr. Ian McCubbin, Mr. Oliver Edberg, Mr Michael Harfoot (2008). *Outlook of Energy Storage Technologies*. Brussels: European Parliament's committee on Industry, Research and Energy (ITRE). February 2008 [online] Available at:

http://www.europarl.europa.eu/document/activities/cont/201109/20110906ATT26009/20110906ATT26009EN.pdf [Accessed Nov. 2018].

[11] International Electrotechnical Commission (IEC): *White Paper: Electrical Energy Storage*, 1st edition, IEC, Geneva, Switzerland, 2011.

[12] IRENA (2017), *Electricity Storage and Renewables: Costs and Markets to 2030*, International Renewable Energy Agency, Abu Dhabi.

[13] Zuo, Wenhua & Li, Ruizhi & Zhou, Cheng & Li, Yuanyuan & Xia, Jianlong & Liu, Jinping. (2017). *Battery-Supercapacitor Hybrid Devices: Recent Progress and Future Prospects*. Advanced Science. Vol.4. 1600539. doi:10.1002/advs.201600539.

[14] Samantara A.K., Ratha S. (2018) *Asymmetric and Hybrid Supercapacitor. In: Materials Development for Active/Passive Components of a Supercapacitor*. SpringerBriefs in Materials. Singapore: Springer. pp 41-46. doi:10.1007/978-981-10-7263-5_4

[15] G. Z. Chen (2013). *Understanding supercapacitors based on nano-hybrid materials with interfacial conjugation*, Progress in Natural Science: Materials International, vol. 3, no. 23, pp. 245-255, 2013. doi: 10.1016/j.pnsc.2013.04.001

[16] Choudhary, N., Li, C., Moore, J., Nagaiah, N., Zhai, L., Jung, Y. and Thomas, J. (2017). *Asymmetric Supercapacitor Electrodes and Devices*. Advanced Materials, 29(21), p.1605336.

doi: 10.1002/adma.201605336

[17] Statistical Office of the European Communities (2018). EUROSTAT: *Gross electricity generation from renewable sources, EU-28*, *1990-2016.* [online] Available at: https://ec.europa.eu/eurostat/statistics-explained/index.php?title=Renewable_energy_statistics/de. [Accessed Oct 2018].

[18] Gregor Erbach (2016). *Understanding electricity markets in the EU. European Parliamentary Research Service*. November 2016. [online] Available at: http://www.europarl.europa.eu/RegData/etudes/BRIE/2016/593519/EPRS_BRI(2016)593519_EN.pdf. [Accessed Nov 2018].

[19] Kouchachvili, L., Yaïci, W. and Entchev, E. (2018). *Hybrid battery/supercapacitor energy storage system for the electric vehicles.* Journal of Power Sources, 374, pp.237-248. doi: 10.1016/j.jpowsour.2017.11.040

[20] A. Burke, H. Zhao (2015). *Applications of Supercapacitors in Electric and Hybrid vehicles.* Davis: University of California. 2015. [online] Available at: https://steps.ucdavis.edu/wp-content/uploads/2017/05/2015-UCD-ITS-RR-15-09-1.pdf [Accessed Nov 2018].

[21] Wang, G., Zhang, L. and Zhang, J. (2012). A review of electrode materials for electrochemical supercapacitors. Chem. Soc. Rev., 41(2), pp.797-828. doi: 10.1039/C1CS15060J.

[22] Yan, J., Wang, Q., Wei, T. and Fan, Z. (2013). *Recent Advances in Design and Fabrication of Electrochemical Supercapacitors with High Energy Densities*. Advanced Energy Materials, 4(4), p.1300816. doi: 10.1002/aenm.201300816.

[23] European Commission's Directorate General for Energy (DG ENER) Working paper. *The future role and challenges of Energy Storage*. 2013.

[24] Luo, X., Wang, J., Dooner, M. and Clarke, J. (2015*). Overview of current development in electrical energy storage technologies and the application potential in power system operation*. Applied Energy, 137, pp.511-536. doi: 10.1016/j.apenergy.2014.09.081.

[25] Ridge Energy Storage & Grid Services L.P., 2015. [online]. Available at: http://www.ridgeenergystorage.com/. [Accessed Nov 2018].

[26] The World Energy Council (2016*). World Energy Resources Report 2016: E-storage - shifting from cost to value – wind and solar applications.* United Kingdom. 2016.

[27] Materials Energy Research Laboratory in nanoscale (2018). *About hydrogen energy. University of New South Wales*. [online] Available at: http://www.merlin.unsw.edu.au/energyh/about-hydrogen-energy/. [Accessed Sept 2018].

[28] Conway, B. (1999). *Electrochemical Supercapacitors*. Boston, MA: Springer US, pp.11-31.

[29] Barak, M. (1990*). Electrochemical Power Sources - Primary and Secondary Batteries*. Peter Peregrinus: Stevenage, 1990, 137(1), pp. 29-34.

[30] Chen, H., Cong, T., Yang, W., Tan, C., Li, Y. and Ding, Y. (2009). *Progress in electrical energy storage system: A critical review.* Progress in Natural Science, 19(3), pp.291-312. doi: 10.1016/j.pnsc.2008.07.014.

[31] T. Kousksou and P. Bruel (2015*). Energy storage: Applications and challenges, Solar Energy Materials and Solar Cells.* Elsevier, 78, pp. 459-464. doi:10.1016/j.egypro.2015.11.698.

[32] González, A., Goikolea, E., Barrena, J. and Mysyk, R. (2016). *Review on supercapacitors: Technologies and materials. Renewable and Sustainable Energy Reviews*, 58, pp.1189-1206. doi: 10.1016/j.rser.2015.12.249.

[33] S. Zaharaddeen and C. Subramani (2016). *A Brief Review on Electrode Materials for Supercapacitor*. International Jornal of Electrochemical Science, 11, pp. 10628 – 10643. doi: 10.20964/2016.12.50.

[34] Yan, J., Wang, Q., Wei, T. and Fan, Z. (2013). *Recent Advances in Design and Fabrication of Electrochemical Supercapacitors with High Energy Densities.* Advanced Energy Materials, 4(4), p.1300816. doi: 10.1002/aenm.201300816

[35] Simon, P. and Gogotsi, Y. (2008). *Materials for electrochemical capacitors*. Nature Materials, 7(11), pp.845-854. doi.org/10.1038/nmat2297.

[36] Wikipedia, Supercapacitor. [online]. Available at: https://en.wikipedia.org/wiki/Supercapacitor. [Accessed Oct 2018].

[37] K. Solanki (2016*). Electrochemical Characterization Of Vanadium Pentoxide (V_2O_5) And Activated Carbon (AC) Electrodes In Multivalent Aluminum Nitrate (Al(NO3)3) Electrolyte For Battery-type Hybrid Supercapacitor Applications.* The University of Wisconsin – Milwaukee. 56(3).; p.113.2016. [online]. Available at: https://www.slideshare.net/KetanSolanki8/thesis-presentation-71201047. [Accessed Oct 2018].

[38] W. Schalkwijk and B. Scrosati, *Advances in Lithium-Ion Batteries*. Springer, 2002, p. 495. doi: 10.1007/B113788

[39] Sirisinudomkit, P., Iamprasertkun, P., Krittayavathananon, A., Pettong, T., Dittanet, P. and Sawangphruk, M. (2017). *Hybrid Energy Storage of $Ni(OH)_2$-coated N-doped Graphene Aerogel//N-doped Graphene Aerogel for the Replacement of NiCd and NiMH Batteries.* Scientific Reports, 7(1). doi: 10.1038/s41598-017-01191-8

[40] Xiao, J. and Yang, S. (2012). *Nanocomposites of $Ni(OH)_2$/Reduced Graphene Oxides with Controllable Composition, Size, and Morphology: Performance Variations as Pseudocapacitor Electrodes.* ChemPlusChem, 77(9), pp.807-816. doi: 10.1002/cplu.201200102.

[41] Navigant Research (2017). *Installed Hybrid Energy Storage System Power Capacity is Expected to Exceed 2 GW in 2026.* [online] Available at: https://www.navigantresearch.com/news-and-views/installed-hybrid-energy-storage-system-power-capacity-is-expected-to-exceed-2-gw-in-2026. [Accessed Oct 2018].

[42] European Commission (2017). *Energy storage*. European Institute for Energy Research (EIFER). Brussels. 2014. [online] Available at: setis.ec.europa.eu/energy-research. [Accessed Oct 2018].

[43] Motupally, S. (1995). *Proton Diffusion in Nickel Hydroxide Films*. Journal of The Electrochemical Society, 142(5), p.1401. doi: 10.1149/1.2048589.

[44] Chaudhari, N., Jin, H., Kim, B. and Lee, K. (2017). *Nanostructured materials on 3D nickel foam as electrocatalysts for water splitting*. Nanoscale, 9(34), pp.12231-12247. doi: 10.1039/C7NR04187J

[45] Eugénio, S., Silva, T., Carmezim, M., Duarte, R. and Montemor, M. (2013). *Electrodeposition and characterization of nickel–copper metallic foams for application as electrodes for supercapacitors.* Journal of Applied Electrochemistry, 44(4), pp.455-465. doi: 10.1007/s10800-013-0646-y.

[46] L. Sun, C.-L. Chien and P. C. Searson*. Fabrication of Nanoporous Nickel by Electrochemical Dealloying*. Chemistry of Materials, 2004, 16 (16), pp 3125–3129. doi: 10.1021/cm0497881.

[47] A.-K. Randa and E.-R. Saad. *Electrochemical Deposition of Nanoporous Metallic Foams for Energy Applications in Advanced Materials and their Applications: Micro to nano scale.* Cairo University, Giza, Egypt.One Central Press, pp.69-90.

[48] Xie, Y., Kocaefe, D., Chen, C. and Kocaefe, Y. (2016). *Review of Research on Template Methods in Preparation of Nanomaterials*. Journal of Nanomaterials, 2016, pp.1-10. doi: 10.1155/2016/2302595.

[59] Y. Guang-Wu, X. Cai-Ling and L. Hu-Lin (2008). *Electrodeposited nickel hydroxide on nickel foam with ultrahigh capacitance*. The Royal Society of Chemistry,48, p. 6537–6539, 2008. doi: 10.1039/B815647F.

[50] Kim, S., Kim, I., Kim, S. and Jang, J. (2017). *Nickel Hydroxide Supercapacitor with a Theoretical Capacitance and High Rate Capability Based on Hollow Dendritic 3D-Nickel Current Collectors.* Chemistry - An Asian Journal, 12(12), pp.1291-1296. doi: 10.1002/asia.201700454.

[51] Prida, V., Vega, V., García, J., Iglesias, L., Hernando, B. and Minguez-Bacho, I. (2015). *Electrochemical methods for template-assisted synthesis of nanostructured materials.* Magnetic Nano- and Microwires, pp.3-39. doi: 10.1016/B978-0-08-100164-6.00001-1.

[52] Kim, B., Sy, S., Yu, A. and Zhang, J. (2015*). Electrochemical Supercapacitors for Energy Storage and Conversion. Handbook of Clean Energy Systems*, pp.1-25. doi/10.1002/9781118991978.hces112.

[53] C2C-NewCap Supercapacitors. (2018). *C2C-NewCap Supercapacitors*. [online] Available at: https://www.c2cnewcap.com [Accessed 3 Dec. 2018].

[54] Xiong, X., Zhang, J., Ma, J., Zeng, X., Qian, H. and Li, Y. (2016). *Fabrication of porous nickel (hydr)oxide film with rational pore size distribution on nickel foam by induction heating deposition for high-performance supercapacitors*. Materials Chemistry and Physics, 181, pp.1-6. doi: 10.1016/j.matchemphys.2016.06.038.

[55] *The Optical Society*. (2018). [online]. Available at: https://www.eng-atoms.msm.cam.ac.uk/Images/SEMScheme. [Accessed Dec. 2018].

[56] Electron Microscopy Solutions. Thermo Fisher Scientific. (2018). [online]. Available at: https://www.fei.com/introduction-to-electron-microscopy/sem/. [Accessed Dec. 2018].

[57] Bumbrah, G. and Sharma, R. (2016). *Raman spectroscopy – Basic principle, instrumentation and selected applications for the characterization of drugs of abuse.* Egyptian Journal of Forensic Sciences, 6(3), pp.209-215. doi*:* 10.1016/j.ejfs.2015.06.001*.*

[58] D. M. Musso. (2000). *Raman Spectroscopy. Comparison of Raman Spectra of selected substances with Infrared Spectra obtained from the literature*. Salzburg. 2000.

[59] Elgrishi, N., Rountree, K., McCarthy, B., Rountree, E., Eisenhart, T. and Dempsey, J. (2017*). A Practical Beginner's Guide to Cyclic Voltammetry*. Journal of Chemical Education, 95(2), pp.197-206. doi: 10.1021/acs.jchemed.7b00361.

[60] Vernon D. Parker (1986*). Linear Sweep and Cyclic Voltammetry in Comprehensive Chemical Kinetics*. Elsevier B.V.,26, 2008, pp. 145-202.

[61] S. P. Kounaves (1997). *Voltammetric Techniques in Handbook of Instrumental Techniques for Analytical Chemistry.* Upper Saddle River, NJ, Prentice Hall PTR, 1997, pp. 710-713.

[62] Princeton Applied Research. *A Review of Techniques for Electrochemical Analysis*. [online] Available at: www.princetonappliedresearch.com. [Accessed Oct 2018].

[63] University of Cambridge, *Linear Sweep and Cyclic Voltametry: The Principles*. [online]. Available at: https://www.ceb.cam.ac.uk/research/groups/rg-eme/teaching-notes/linear-sweep-and-cyclic-voltametry-the-principles. [Accessed Oct 2018].

[64] A. B. Bocarsly (2002). *Cyclic Voltammetry. Characterization of Materials*. Princeton, NJ, Princeton University, 2002, pp. 580–592. doi: 10.1002/0471266965.com050.pub2.

[65] Lukatskaya, M., Dunn, B. and Gogotsi, Y. (2016). *Multidimensional materials and device architectures for future hybrid energy storage.* Nature Communications, 7(1). doi: 10.1038/ncomms12647 (2016).

[66] R. Ruiz-Rosas (2015). *Design of hybrid asymmetric capacitors in aqueous electrolyte using ZTC and ultraporous activated carbons*. Instituto Universitario de Materiales de Alicante, Alicante, Spain, 2015.

[67] Attias, R., Sharon, D., Borenstein, A., Malka, D., Hana, O., Luski, S. and Aurbach, D. (2017). *Asymmetric Supercapacitors Using Chemically Prepared MnO_2 as Positive Electrode Materials*. Journal of The Electrochemical Society, 164(9), pp. A2231-A2237. doi: 10.1149/2.0161712jes.

[68] Ashassi-Sorkhabi, H., La'le Badakhshan, P. and Asghari, E. (2016). *Electrodeposition of three dimensional-porous Ni/$Ni(OH)_2$ hierarchical nano composite via etching the Ni/Zn/$Ni(OH)_2$ precursor as a high performance pseudocapacitor.* Chemical Engineering Journal, 299, pp.282-291. doi:10.1016/j.cej.2016.04.069.

[69] K. I. Popov, S. D. Stojan, D. Nebojs˘a (2016). *Morphology of Electrochemically and Chemically Deposited Metals*, Switzerland: Springer Nature, 2016, pp.209-303.

[70] Chen, K. and Xue, D. (2014). *Electrochemically Stabilized Porous Nickel Foam as Current Collector and Counter Electrode in Alkaline Electrolyte for Supercapacitor. Journal of Nanoengineering and Nanomanufacturing*, 4(1), pp.50-55. doi:10.1166/jnan.2014.1168.

[71] Ding Yunchang, Yuan Jiongliang and Chang Zhaorong (1997). *Cyclic voltammetry response of coprecipitated $Ni(OH)_2$ electrode in 5 M KOH solution.* Journal of Power Sources, 69(1-2), pp.47-54. doi:10.1016/S0378-7753(97)02565-2.

[72] Gu, L., Wang, Y., Lu, R., Guan, L., Peng, X. and Sha, J. (2014). *Anodic electrodeposition of a porous nickel oxide–hydroxide film on passivated nickel foam for supercapacitors.* J. Mater. Chem. A, 2(20), pp.7161-7164. doi: 10.1039/C4TA00205A.

[73] Aghazadeh, M., Ghaemi, M., Sabour, B. and Dalvand, S. (2014*). Electrochemical preparation of α-Ni(OH)2 ultrafine nanoparticles for high-performance supercapacitors*. Journal of Solid State Electrochemistry, 18(6), pp.1569-1584. doi: 10.1007/s10008-014-2381-7.

[74] G.-r. Fu, Z.-a. Hu, L.-j. Xie, X.-q. Jin, Y.-l. Xie, Y.-x. Wang, Z.-y. Zhang, Y.-y. Yang and H.-y. Wu (2009.). *Electrodeposition of Nickel Hydroxide Films on Nickel Foil and Its Electrochemical Performances for Supercapacitor.* International Journal of Electrochemical Science, 4(8), pp. 1052 – 1062.

[75] Hall, D., Lockwood, D., Bock, C. and MacDougall, B. (2014). *Nickel hydroxides and related materials: a review of their structures, synthesis and properties*. Proceedings of the Royal Society A: Mathematical, Physical and Engineering Sciences, 471(2174), pp.20140792-20140792. doi: 10.1098/rspa.2014.0792.

[76] Kostecki, R. (1997). *Electrochemical and In Situ Raman Spectroscopic Characterization of Nickel Hydroxide Electrodes.* Journal of The Electrochemical Society, 144(2), p.485. doi: 10.1149/1.1837437.

[77] Numan, A., Duraisamy, N., Saiha Omar, F., Gopi, D., Ramesh, K. and Ramesh, S. (2017). Sonochemical synthesis of nanostructured nickel hydroxide as an electrode material for improved electrochemical energy storage application. Progress in Natural Science: Materials International, 27(4), pp.416-423. doi:10.1016/j.pnsc.2017.06.003.

[78] Kirubasankar, B., Palanisamy, P., Arunachalam, S., Murugadoss, V. and Angaiah, S. (2018*). 2D $MoSe_2$-$Ni(OH)_2$ nanohybrid as an efficient electrode material with high rate capability for asymmetric supercapacitor applications.* Chemical Engineering Journal, 355, pp.881-890. doi: 10.1016/j.cej.2018.08.185.

[79] The Prashant Kamat Laboratory (2018). University of Notre Dam. [online]. Available at: https://www3.nd.edu/~kamatlab/. [Accessed Oct 2018].